Measurement of $\sigma \times \mathrm{Br}(\mathrm{W} \longrightarrow \tau + \nu + \mathrm{jets})$ Via Precision Tracking in $\bar{p}p$ Collisions at $\sqrt{s} = 1.8$ TeV

by

Robert Andrew Dunn

A dissertation submitted in partial fulfillment
of the requirements for the degree of
Doctor of Philosophy
(Physics)
in The University of Michigan
1995

Doctoral Committee:

Professor J. Wehrley Chapman, Chair
Professor Hugh D. Aller
Associate Professor Dante Amidei
Professor David Williams
Professor Jens Zorn

"What does it mean to be human?

What does it mean to be human? I cannot help but suspect that at one time in the history of thinking that people believed that it meant that we were spiritual and that we could make choices and were capable of aspiring to higher ideals . . . like maybe loyalty or maybe faith . . . or maybe even love. But now we are told by people who think they know that we vary from the amoeba only in the complexity of our makeup and not in what we essentially are. They would have us think as Dysart said that we are forever bound up in certain genetic reigns — that we are merely products of the way things are and not free, not free to be the people who make them that way. . . . Well who are they? They are the few that sit at the top of the heap – dung heap though it is – and who say it is better to reign in Hell than to serve in Heaven. Well I do not know that we can have a Heaven here on earth, but I am sure that we need not have a Hell here either.

What does it mean to be human?

I cannot help but believe that it means that we are spiritual – that we are responsible and that we are free. That we are responsible *to* be free."

— *Rich Mullins, "Intro to Higher Education" from the album Never Picture Perfect*

Acknowledgments

I would say that it has been a long road getting to this point, but it seems to me that I spent a good deal more time slashing through wilderness than actually on any kind of pavement.

I am grateful to my advisor, J. Chapman, for giving me the opportunity to work in the field of particle physics. His calm and patience in this long endeavor have been most appreciated. Thanks also to Dan Amidei for introducing me to tau physics and suggesting the initial direction of this research.

My time in grad school was greatly enriched by the company of those outside the lab. A few brave souls deserve special thanks for putting up with me when I really wasn't much fun to be around: Alan, various Dave's, Julie, and Tami. Rock on.

And most of all I thank my Lord Jesus, without whom all is lost.

Table of Contents

List of Tables

Table

List of Figures

Figure

List of Appendices

Appendix

Chapter 1

Introduction

Order or chaos? Is the universe in which we live governed by laws that regulate the behaviors and interactions we observe around us, or is the world an incomprehensible collection of randomness and dissonance? It is the fundamental assumption of science that there is order – that there exist principles which are constant, self-consistent, and knowable – and it is this which science seeks. By the formulation of hypothesis and the subsequent test by experiment, the scientist attempts to understand the nature of nature itself.

The field of physics has achieved considerable success in this quest, especially in the area of elementary particle interactions. The current collection of theories, dubbed the Standard Model, has been experimentally verified to high accuracy in many areas and has been used to predict correctly the behavior of particles that had not been observed at the time, an example being the correct calculation of the decay modes of the tau lepton four years before its discovery in 1975 [1]. However, there remain areas inadequately explained by the Standard Model (such as the origin of mass) and areas where the Standard Model predictions are not yet verified (e.g. the existence of the tau neutrino), so the research continues.

The study of elementary particles depends heavily on the correct identification of the resultant particles from the interactions, especially the charged members of the lepton families. For energetic electrons and muons there exist methods to determine particle type from the detector response. The tau lepton is more problematic because its short lifetime

(295.7 ± 3.2 fs [2]) means that the tau does not reach any of the detectors at a collider experiment. The issue is further complicated by the ability of the tau to produce a variety of decay products. The tau lepton decay produces a tau neutrino and a virtual W boson. The W promptly decays into an electron and an electron neutrino, a muon and a muon neutrino, or hadrons. The last of these, the hadronic decay modes of the tau lepton, are interesting for many reasons, not the least of which is that these modes account for the majority of the tau decays. It is therefore beneficial in the identification and study of tau leptons to be able to distinguish the hadronic tau decays from other sources of jets, such as quarks and gluons. In practice this is difficult at hadron colliders due to copious non-tau sources of hadronic jets.

This dissertation describes a technique for identifying hadronic tau decays in which highly energetic taus are separated from background by making use of the displaced vertex caused by the short distance travelled by the tau before it decays. The efficacy of the algorithm is demonstrated by the observation and measurement of hadronic tau jets in $\bar{p}p \longrightarrow W+$ associated jets, with $W \longrightarrow \tau\ \nu_\tau$.

1.1 Motivation for the Measurements

The tau lepton provides a channel into the understanding of the physics of elementary particles unlike any other currently known fundamental particle. With a mass of 1.784 GeV/c^2, it is the only lepton sufficiently massive to decay into hadrons. Furthermore, its short lifetime allows precision measurements of certain predictions of electroweak theory [3].

The tau lepton was discovered in 1975 by Martin Perl, *et al*, at SLAC [4] by observation of the process $e^+ + e^- \longrightarrow \tau^+ + \tau^- \longrightarrow e^\pm + \mu^\mp +$ missing energy. Further experiments have observed the hadronic decays of taus, allowing precision measurements of the branching fractions of the various tau decay modes, the lifetime of the tau, and (indirectly) the mass of the tau neutrino. The production of tau pairs at electron-positron colliders is sufficiently distinguishable from background that high-purity data sets can be selected.

Identification of taus at hadron colliders has proven to be more difficult. Observation of the reaction $\bar{p}p \longrightarrow W \longrightarrow \tau\nu_\tau$, with the tau decaying hadronically, has been accomplished at UA1 [5] and CDF [6], with the creation of data samples of approximately 60% signal and 40% background. Such studies are discussed in greater detail in chapter 4. Tau jets have not been observed in other event topologies at hadron colliders prior to this analysis. Many studies which are expected to be statistically limited (top quark analyses, Higgs boson searches) at current hadron colliders might benefit from the accessibility of the tau decay channels.

1.2 Outline

Herein is described in detail the development and implementation of an algorithm to preferentially select energetic hadronic tau decays over other sources of hadronic jets. Experimental validation of this "tau tagging" technique is presented by the creation of high-purity tau samples from the proton-antiproton collisions gathered at the Collider Detector at Fermilab (CDF) during the 1992-1993 run of the Fermilab Tevatron.

Chapter 2 provides a discussion of the experimental apparatus used, both the detector setup at CDF and the Tevatron accelerator used to produce the proton-antiproton collisions. Particular attention is given to the CDF Silicon Vertex Detector, since it is of primary importance in this analysis.

In chapter 3 a description of the signed impact parameter and its relation to displaced vertices is provided.

Chapter 4 details the selection of the control and background samples used in this thesis. A sample enriched in hadronic tau decays is selected from the data. It is then shown that the fractional tau content is determinable from the track multiplicity distribution and from the impact parameter distribution. The lifetime of the τ is measured.

Chapter 5 describes the tau tagging algorithm, including the derivation of the technique, studies of the algorithm on background and Monte Carlo samples, determination of the efficiency from the control sample, and systematic effects.

Chapters 6 and 7 present the results of the application of the tau tagging algorithm to the data, with chapter 6 discussing the $W \longrightarrow \tau + \nu + n$ jets results and chapter 7 discussing a top search in which one or both of the W bosons decay into a tau. Measurements of the cross-section times branching ratio are computed for those topologies for which there are sufficient statistics.

Chapter 8 summarizes the results of this work.

Chapter 2

Experimental Apparatus

In the plains near Batavia, Illinois lies the Fermi National Accelerator Laboratory (Fermilab), a facility run for the United States Department of Energy by the University Research Associates. Fermilab plays host to a variety of studies in particle physics ranging from fixed-target neutrino experiments to proton-antiproton collider experiments at energies not achievable at any other facility.

The data for this thesis were taken at the Collider Detector at Fermilab, one of the two facilities currently operating to study the $\bar{p}p$ collisions produced by the Fermilab Tevatron. In this chapter the equipment and data-acquisition system used in this analysis are described, with particular attention given to those components relevant to tau identification.

2.1 The Tevatron at Fermilab

Shown schematically in figure 2.1, the Tevatron synchrotron [7] is the final stage of a series of accelerators used to create the $\bar{p}p$ collisions. Protons are accelerated to an energy of 400 MeV by a linear accelerator (LINAC) before introduction into the Booster synchrotron ring. In the Booster, the proton beam is accelerated to 8 GeV and separated into discrete groups, or "bunches," before insertion into the Main Ring.

Sharing the 4-mile-circumference beam tunnel with the Tevatron, the Main Ring synchrotron at Fermilab boosts the protons to an energy of 150 GeV. From there, the protons

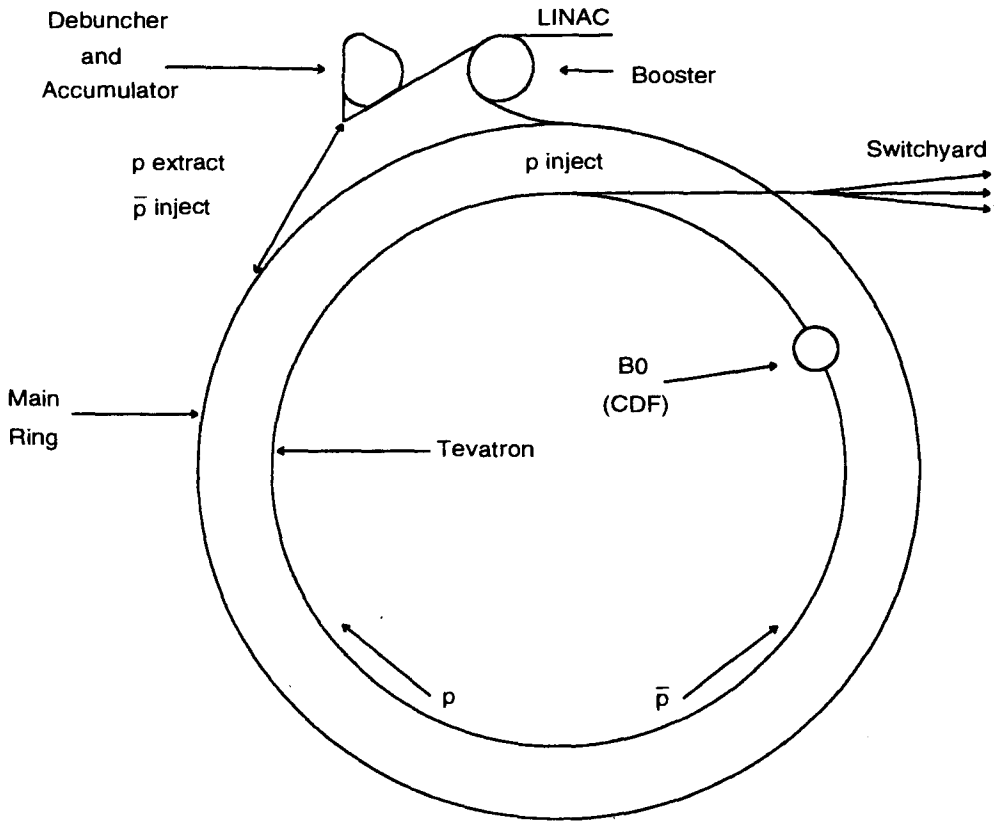

Figure 2.1: Schematic view of the Tevatron facility at the Fermi National Accelerator Laboratory.

can then be injected in the Tevatron superconducting synchrotron for further acceleration, or extracted for use in the creation of antiprotons. Antiprotons produced by the collision of the extracted protons with a tungsten-rhenium target are collected and stored in an accumulator ring until a stockpile of sufficient size for collider usage is achieved. The antiprotons are then removed in bunches from the accumulator, accelerated with the Main Ring, and inserted into the Tevatron (revolving counter-clockwise as opposed to the clockwise direction of the Tevatron proton bunches). When the proton and antiproton bunches are in the Tevatron, they are accelerated to an energy of 900 GeV in the laboratory frame. By counter-rotating the bunches, collisions with a total center-of-mass energy of 1.8 TeV are obtained.

The first recorded Tevatron $\bar{p}p$ collisions were seen at the then-incomplete Collider Detector at Fermilab (CDF) in October, 1985. A completed CDF facility was commissioned during a brief run from January, 1987 to May, 1987.

The first significant data-taking using the $\bar{p}p$ collisions of the Tevatron took place at the Collider Detector at Fermilab (CDF) during Run 0 in 1988-1989. After substantial upgrades to the CDF detector, and the addition of a second general-purpose collider detector at the D0 site, the Tevatron ran in collider mode from August, 1992 to May, 1993. During this run (designated as Run 1a), six bunches of protons (each typically consisting of 10^{11} particles) and six bunches of antiprotons (each typically consisting of 3×10^{10} particles) were used in the Tevatron, producing instantaneous luminosities of order $3 \times 10^{30} \mathrm{cm}^{-2}\mathrm{sec}^{-1}$ at the collision sites. This luminosity provided ~ 1.6 proton-antiproton interactions per bunch crossing. Beams were run in stores about 12 hours in duration.

2.2 Collider Detector At Fermilab

For this thesis, the data were collected at CDF during the 1992-1993 run of the Tevatron. CDF [8], shown in figure 2.2, is a forward-backward and cylindrically-symmetric multi-purpose detector surrounding the Tevatron beampipe. The proton and antiproton bunch orbits in the Tevatron are set such that one of the collision sites is approximately at the center of CDF, with some spread from beam tuning effects and the finite extent of the

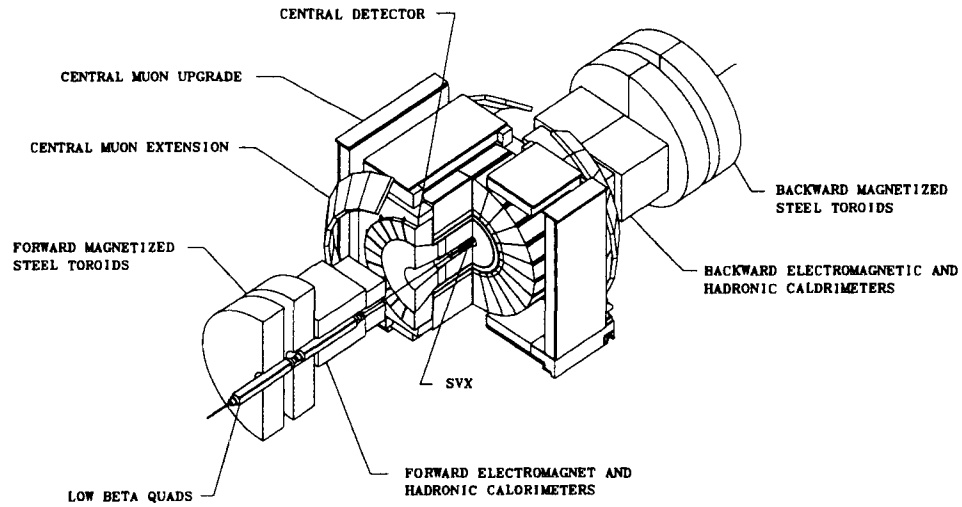

Figure 2.2: An isometric view of the CDF detector.

particle bunches. Many of the $\bar{p}p$ collisions are of the elastic and quasi-elastic scattering variety and are not of particular interest in the types of searches being conducted at CDF. Of more interest are the deeply inelastic collisions in which the partons of the colliding beams interact. In contrast with the small scattering angles (in the lab frame) of the unwanted collisions, the inelastic collisions of interest to the CDF collaboration (see appendix C) are more likely to produce particles with a considerable momentum boost in the plane transverse to the beamlines. Accordingly, CDF places its highest resolution components in the central region of the detector.

A schematic cross-section [9] of the upper-east quadrant of the CDF detector (see figure 2.3) shows the arrangement of the many distinct subsystems used in the observation of the collisions. The other quadrants of CDF are functionally similar to the quadrant shown,

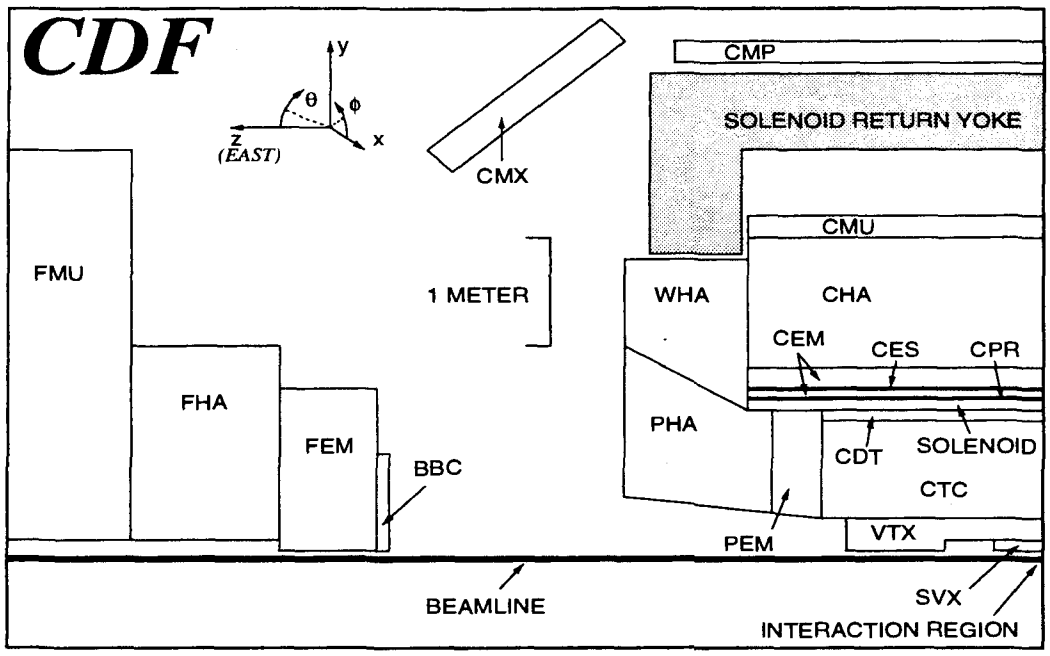

Figure 2.3: A sideview of one quadrant of the CDF detector.

though some small differences exist. Figure 2.3 indicates the CDF coordinate system, which is a cylindrical system whose z axis runs along the beamline (with increasing z along the proton direction) and an azimuthal angle ϕ measured from the north-pointing horizontal. The polar angle θ is measured from the positive z axis, but it is often more convenient in the analysis to deal with the pseudo-rapidity coordinate, which is related to the polar angle by

$$\eta = -\ln\left(\tan\left(\frac{\theta}{2}\right)\right)$$

As described below, many of the CDF detector components are segmented in terms of these variables.

2.2.1 Tracking Systems

A 1.4 Tesla superconducting solenoid at CDF produces a magnetic field approximately coaxial with the beampipe, and within this field are the tracking systems. The path

of a charged particle traversing the solenoid's field is (to within multiple–scattering and brehmstrallung corrections) a right circular helix whose curvature is inversely related to the component of momentum in the transverse plane, $\vec{P_T} = \vec{P} \sin\theta$. The tracking subsystems provide measurements of the trajectories of the particles, permitting the calculation of the momentum of the particle (assuming unit electric charge).

The CDF detector component nearest the interaction region is the Silicon Vertex Detector (SVX) [10], a silicon microstrip device used to measure to high precision the paths of charged tracks in the $r - \phi$ plane. The SVX does not provide z position information. It is the ability of the SVX to determine track impact parameters with resolutions on the order of tens of microns that permits the identification of secondary vertices from short-lived particles such as B mesons and tau leptons. As the impact parameter information plays a crucial role in this thesis, the SVX is described in detail in section 2.4.

As seen in figure 2.3 encompassing the SVX is the CDF Vertex Detector (VTX), a time-projection chamber used to determine the z-coordinate of the primary event vertex on an event-by-event basis. The non-negligible lengths of the p and $\bar{p}$ bunches in the Tevatron result in an interaction region extended along the z axis, which is well described by a gaussian of width $\sim 30cm$ for any given beam store. The location and shape of the interaction region vary slightly from store to store, and it is necessary to monitor these changes to compute geometric acceptances for cross-section calculations. A discussion of this is presented as appendix B. The 24 chambers of the VTX [11] provide coverage from $+1.5m$ to $-1.5m$ along the z axis, which is adequate for most CDF analyses. The longitudinal acceptance for events used in this thesis is limited by the length of the SVX.

Outside the VTX is the Central Tracking Chamber (CTC). The CTC [12] (shown in Fig. 2.4) provides the main source of charged particle tracking information at CDF. The CTC consists of 5 axial superlayers and 4 stereo superlayers of drift cells. The axial superlayers have 12 layers of drift cells running parallel to the z axis, while the stereo superlayers have 8 layers of drift cells tilted $\pm 3°$ about the z axis. Though the stereo superlayers do allow some determination of the inclination of the track with respect to the

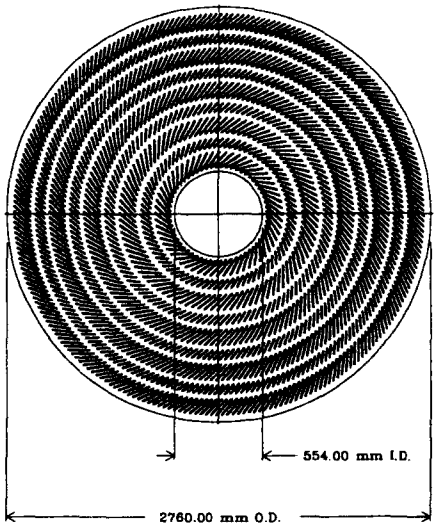

Figure 2.4: An end view of the Central Tracking Chamber (CTC).

beam axis, the CTC is much more adept at tracking reconstruction in the transverse plane. The $r - \phi$ resolution of the axial superlayers permits transverse momentum measurements to a precision of $\delta P_T = 0.001 P_T$. As described more fully in section 2.4, all SVX tracks are associated with reconstructed CTC tracks. The combined CTC-SVX system attains a momentum resolution of $\frac{\delta P_T}{P_T} = [(0.0009\ P_T)^2 + (0.0066)^2]^{1/2}$, where P_T is measured in GeV/c.

2.2.2 Calorimetry

Further from the interaction region are the calorimeter systems which record energy flow in the event. The calorimetry at CDF consists of separate subsystems for central (CEM [13], CHA [14], and WHA), plug (PEM [15] and PHA [16]), and forward regions (FEM [17] and FHA [18]). Though differing in resolution and location, the calorimeters for each of the regions share the features that they are composed of distinct electromagnetic and hadronic components (with the electromagnetic calorimeters closer to the interaction region

Calorimeter Subsystem	Geometric Coverage η Range	Energy Resolution	Absorption Thickness
CEM	$0.0 < \|\eta\| < 1.1$	$13.7\%/\sqrt{E_T} \oplus 2\%$	18 X_0
PEM	$1.1 < \|\eta\| < 2.4$	$22\%/\sqrt{E} \oplus 2\%$	18-21 X_0
FEM	$2.2 < \|\eta\| < 4.2$	$26\%/\sqrt{E} \oplus 2\%$	18 X_0
CHA	$0.0 < \|\eta\| < 0.9$	$50\%/\sqrt{E_T} \oplus 3\%$	4.5 λ_0
WHA	$0.7 < \|\eta\| < 1.3$	$75\%/\sqrt{E} \oplus 4\%$	4.5 λ_0
PHA	$1.3 < \|\eta\| < 2.4$	$106\%/\sqrt{E} \oplus 6\%$	5.7 λ_0
FHA	$2.4 < \|\eta\| < 4.2$	$137\%/\sqrt{E} \oplus 3\%$	7.7 λ_0

Table 2.1: A summary of the CDF calorimetry components. Thicknesses are given in radiation lengths (X_0) for the electromagnetic calorimeters and in pion interaction lengths (λ_0) for the hadronic calorimeters.

for each region) which are internally divided into projective towers in $\eta - \phi$ whose boundaries extrapolate to the CDF coordinate origin. A summary of the calorimeter properties is given in table 2.1.

Because the center–of–mass frame of the partons involved in the interaction is not necessarily at rest in the lab frame, the resultant particles may be considerably boosted along the z axis. However, the transverse component is largely unaffected by the parton momenta (the contribution being mainly from Fermi motion within the protons and antiprotons, which is at a much lower energy scale than the Tevatron accelerator) and it is therefore more informative to use the transverse energy of a particle or jet of particles, $E_T = E \sin\theta$.

2.2.3 Other Systems

The outermost detectors at CDF are used for muon identification purposes. The Central Muon chambers [19] (CMU) provide most of the coverage for the central region (with additional information coming from the newly added Central Muon Upgrade [20] (CMP) and Central Muon Extension (CMX) detectors). There is no corresponding plug region muon detection equipment, but CDF does have a Forward Muon system (FMU) to provide coverage at high η. While the muon detectors are not used in the identification of

hadronic tau decays, they are used in rejecting certain types of background (see section 4.1) as well as selecting good muon candidates for a top quark search (see chapter 7).

The BBC (Beam-Beam Counters) are located in the forward and backward regions of CDF near the beamline. Consisting of two planes of scintillation counters covering the range $3.24 < |\eta| < 5.88$, the BBC [21] are used both as a minimum-bias trigger and as a luminosity monitor.

2.3 Data Acquisition at CDF

Not every collision produced at the CDF detector is of interest. CDF is primarily concerned with the study of highly inelastic collisions, and is designed accordingly. However, the frequency of the collisions (bunch crossings occur about every 3.5 μsec) and the large number of data channels (about 100,000) make the recording of every event infeasible. The result is a need to determine, in real-time, whether a given bunch crossing resulted in a collision that might be of interest. To this end, CDF employs a multi-level trigger system [24] to determine which of the events are to be written to the tape drives for further analysis.

2.3.1 Level 1 Trigger

To avoid deadtime, the first level trigger decision must be made in the 3.5 μsec interval between bunch crossings. It is, not surprisingly, the simplest trigger in terms of the requirements made. The Level 1 trigger has three main criteria in determining whether an event will be considered at higher levels of the trigger:

1. Coincidence Hits in the East and West BBCs
2. Single Calorimeter Towers Over Transverse Energy Threshold
3. Muon Chamber Track Stubs Over Transverse Momentum Threshold

The BBC coincidence requirement was used in all calorimetry and muon triggers in the first half of the data run to reduce the rate of false triggers caused by noise in the detector. Later in the run the instantaneous luminosity proved sufficiently high to rate–saturate the BBC's. This limited the effectiveness of the BBC requirement in trigger

decisions, so the BBC coincidence was dropped as a prerequisite for most higher level triggers in the last half of the run. A rate-limited minimum bias trigger using only the BBC requirement was kept for various calibration studies, such as the event vertex distribution discussed in Appendix B.

The Level 1 calorimetry trigger considers the information in projective towers each covering a range of $\Delta\eta_{detector} \times \Delta\phi = 0.2 \times 15°$. The analog signals from the resulting 2048 calorimetry trigger towers are corrected for pedestals and gains before comparison against thresholds.

There is no information from the CDF tracking systems available in time for use by the Level 1 trigger, so the z coordinate of the primary vertex is not known when computing the transverse energy of the calorimetry towers. Therefore, the trigger makes the approximation that the collisions always occur at $z = 0$ in the CDF coordinate system, and computes the E_T for each tower as $E_T = E \sin\theta_{detector}$. This approximation leads to some inefficiency, which will be discussed in later chapters. Once the E_T has been computed, the measurements for each tower are compared with predetermined thresholds which vary from system to system (*e.g.* 6 GeV for the CEM to 25 GeV for the FHA). While no explicit requirement on the Level 1 calorimetry triggers is used in this analysis, it is by way of these triggers that most of the events used in this analysis were accepted.

The Level 1 muon triggers [25] are slightly different for each of the muon subsystems of the detector. The difference in drift times for alternate, radially–projective layers in the CMU gives an estimation of the slope of the muon path in the transverse plane. This slope, which is inversely proportional to the transverse momentum of the muon candidate, is used by the Level 1 CMU trigger to select only those tracks above a predetermined P_T threshold. The CMP trigger required coincidence hits in two of four cells traversed by muons of interest. The Level 1 muon triggers are not used in the identification of hadronic tau decays.

If the event passes the Level 1 trigger, then an "accept" signal is generated, the beam clock signal is inhibited, and the detector signals are not reset. The information for the event is then passed to the Level 2 trigger.

2.3.2 Level 2 Trigger

At the expense of incurring some deadtime (there remains the possibility that consecutive bunch crossings will both result in Level 1 trigger acceptance), the Level 2 trigger performs a more sophisticated check on the event taking $\sim 20\mu sec$ [26]. At this stage in the online processing, two new pieces of information are available:

- Clustering of calorimetry information into jet candidates
- Rough two-dimensional track information from the CTC

Custom processor boards cluster the 2048 calorimeter trigger towers into jet candidates. Two maps of the trigger towers are made, each corresponding to towers whose transverse energy is above a given threshold. The higher–energy threshold map corresponds to those towers that pass a "seed" cut, and are used as the starting points in the clustering algorithm. The lower–energy map lists the towers above the "shoulder" cut. For each seed tower, a check of the four adjacent towers in $\eta - \phi$ space is made to see if any are in the shoulder tower map. If so, the shoulder tower is added to the cluster associated with the seed tower, and another shoulder tower search is made of the those towers adjacent to the added tower. This is repeated until all neighboring towers have been checked, with the proviso that no tower is associated with more than one cluster.

Once the clustering algorithm has converged, the information for that cluster is computed from the constituent towers. This includes:

- $E_x = \sum_{towers} E \cos\phi \sin\theta$
- $E_y = \sum_{towers} E \sin\phi \sin\theta$

- $E_T = \sqrt{{E_x}^2 + {E_y}^2}$
- $\eta_{cluster}$, weighted by the E_T of the cluster towers
- $\phi_{cluster}$, weighted by the E_T of the cluster towers
- number of trigger towers used
- fraction of the cluster from the electromagnetic and hadronic calorimeter towers

and other useful quantities. Here, both θ and η refer to the detector coordinates (with respect to $z = 0$).

A real-time two-dimensional track reconstruction from the CTC is obtained using the Central Fast Tracker [27]. The CFT uses the timing information from the five axial superlayers of the CTC for crude momentum and azimuthal calculation. The CFT uses a look–up table to determine the momentum range of up to 64 identified tracks with a resolution of $\delta P_T/P_T^2 \sim 3.5\%$. The P_T information from the CFT is quantized in eight bins with central values ranging from 3.3 to 30.0 GeV/c. This information, along with the ϕ positions of the candidate tracks, is then accessible by the Level 2 processor for use in associating the tracks with jet and muon candidates.

Furthermore, the vector sum of the calorimetry energy is computed. The center–of–mass frame of the parton collision at CDF is typically boosted along the z axis, as discussed earlier, but there the boost in the plane perpendicular to the beamline is negligible. Conservation of momentum requires that the vector sum of the transverse components be zero. The extent to which this is not true can indicate the presence of particles (such as neutrinos) which went undetected. The vector sum of the transverse energy is:

$$\vec{E}_T = \sum_{towers} E_x \hat{x} + E_y \hat{y}$$

The amount of missing transverse energy ($\not\!\!E_T$) is the negative magnitude of this quantity, with an associated direction opposite that of the total $\vec{E}_T$ vector.

With the track and jet cluster information, the Level 2 processor then runs a variety of routines to make selections for various types of events. Some triggers, such as the JET70 trigger, require only that there be at least one jet candidate with $E_T > 70$ GeV. Others, such as the TAU_20_MET_20 trigger, require the association of CFT tracks in certain momentum ranges with jet clusters meeting energy and shape criteria. To associate a CFT track with a jet or muon candidate, the Level 2 processor computes the distance between the track and the jet/muon candidate in ϕ and compares with a threshold setting. Many such triggers are run at Level 2, with the option of dynamically prescaling the rates of triggers whose cross-sections are too large.

For certain portions of this analysis, requirements are made on the Level 2 triggers by which the event was accepted. In particular, it is required that the TAU_20_MET_20 trigger was satisfied by all events used in the search of $W \longrightarrow \tau + \nu_\tau + n$ jets. This trigger is discussed in detail in section 6.1.1.

Only after a Level 2 accept signal is generated is the entire detector read-out and digitized. The data is then formatted by hardware processors termed the Event Builders and passed to the Level 3 trigger.

2.3.3 Level 3 Trigger

The Level 3 trigger at CDF [28] consists of a set of commercial Silicon Graphics computers. The eight computers each hold six RISC CPUs with two data buffers for each of the CPUs, for a maximum of 96 data buffers online. Each data buffer holds one event, and the buffers are processed asynchronously to allow higher throughput.

In contrast to the highly-customized code run in the Level 2 processors, most of the Level 3 analysis code is written in FORTRAN. A smaller version of the standard CDF offline event reconstruction code is run at Level 3, which provides full CTC tracking, z vertex location, better calorimeter clustering, muon track reconstruction, and other global calculations. One note is that SVX tracking is not done at Level 3.

As with the Level 2 trigger, there are many distinct types of triggers employed

in Level 3 to determine whether the events are of interest. By this stage, the event has been sufficiently reconstructed to allow selection based on the presence of certain particles (electrons, muons, taus, and photons) and by event topologies (multi-jets, large missing energy, etc). The Level 3 triggers relevant to this analysis are discussed in a later chapter.

By using the multi-level trigger system, CDF is able to reduce the initial event rate of about 285 KHz to around 6 Hz. Events passing the Level 3 trigger are written to 8 mm tape for reprocessing and later analysis.

2.4 The Silicon Vertex Detector

Presented below is a discussion of both the detector hardware and the tracking software which provide the impact parameter information necessary for the identification of secondary vertices. The SVX was installed in 1991 as an upgrade to CDF. It was replaced at the end of Run 1a by a functionally-equivalent, radiation-resistant version for the next collider run after radiation damage reduced the utility of the SVX.

2.4.1 The SVX Hardware

The SVX (shown in figure 2.5) consists of four concentric layers of microstrip detectors in each of two modules. There is a 2.15 *cm* gap between the halves and a total active detection region of 51 *cm* along the z axis. The four layers, ranging in radius from 3.005 *cm* at layer 0 to 7.866 *cm* at layer 3, are divided azimuthally into 12 "ladders" which form projective wedges toward the z axis. A ladder, shown in figure 2.6, is composed of 3 DC-coupled microstrip detectors arranged along a supporting substrate. The three inner layers of the SVX have 60 μm pitch microstrip detectors, while the microstrip detectors in the outer layer have a 55 μm pitch. The SVX has a nominal signal–to–noise ratio of 9:1 for minimum ionizing particles at normal incidence.

The 46,080 channels of the SVX are read–out through 360 custom IC's operating in a sparse scan mode. While in sparse-scan mode, only those channels whose integrated

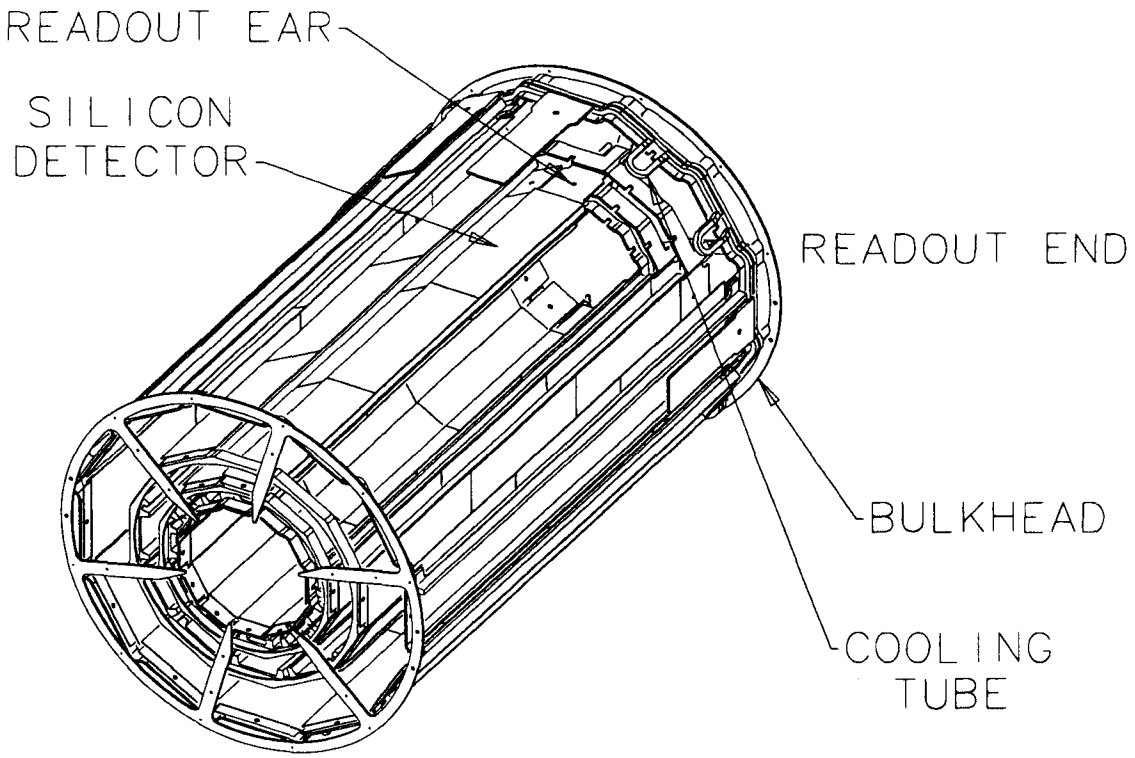

Figure 2.5: A cutaway view of the Silicon Vertex Detector.

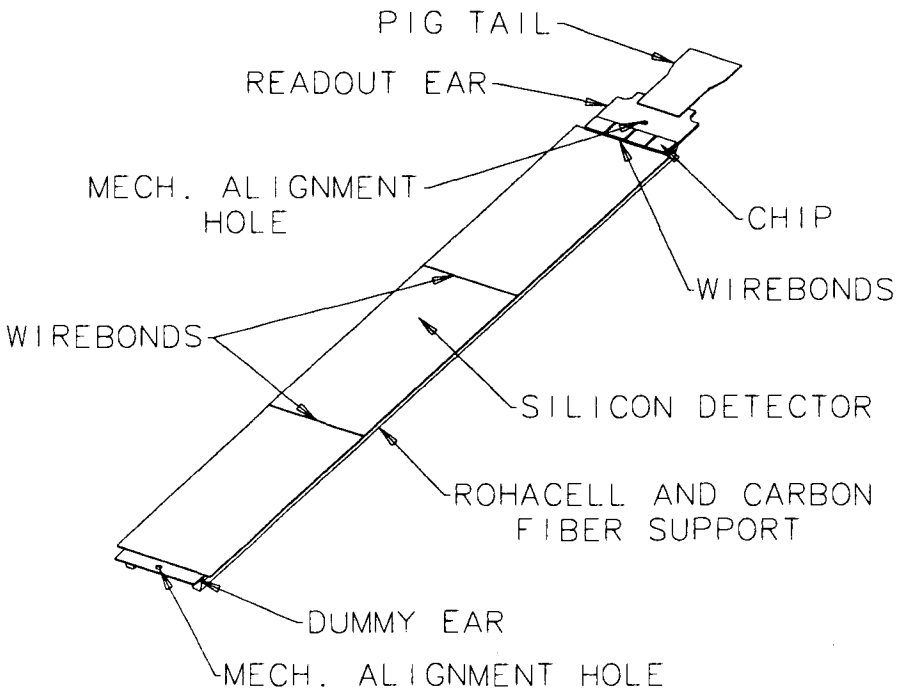

Figure 2.6: An SVX ladder.

charge is above a threshold are digitized for analysis. A "latch all" read–out mode in which all SVX channels are read–out is also available, but the read–out time in latch–all mode is prohibitively long for normal data taking. As such, the latch–all mode was used primarily for diagnostic purposes.

The channel data are passed to a set of four FASTBUS-based Sequencers [22] and four SVX RABBIT [23] crates, each with 6 digitizers, to cover the 24 SVX wedges. The SVX portion of the DAQ system is connected to the rest of the CDF online system by a set of SLAC Scanner Processors (SSPs), which store and reformat the SVX data according to CDF protocols.

The timing for the read–out and charge integration of the SVX is governed by clock-signals synchronized with the Tevatron. The SVX Sequencers are responsible maintaining this part of the SVX operation, as well as the synchronization with the 53 MHz CDF Master clock which drives the CDF DAQ system. The determination of whether a given SVX event is passed on to the DAQ is determined by the multi-level CDF trigger system, discussed in more detail in section 2.3.

2.4.2 SVX Track Reconstruction

The fine segmentation of the microstrips in the SVX permits extremely accurate measurements of the ϕ positions of the hits of charged tracks as they pass through the SVX. This allows the determination of the impact parameters of tracks to an asymptotic resolution of $\sim$ 16 μm. However, optimal track reconstruction is the result of the combination of information from all the tracking detectors at CDF.

The process of track reconstruction begins in the CTC, where a 2-dimensional fit in the transverse plane $(r-\phi)$ is performed using only the CTC axial superlayers. Information from the VTX about the z position of the primary event vertex is then considered as the hits in the CTC stereo superlayers are added to the tracks to attempt a 3-dimensional track reconstruction. Because the tracks can be represented by right circular helices whose axis

is known, there are only five independent variables needed to describe the track. CDF chooses, by convention, the following set of descriptors:

- Curvature: the 2-dimensional curvature obtained from the axial CTC superlayers which is inversely proportional to the transverse momentum of the track
- $\cot\theta$: the cotangent of the polar angle θ which is found from the CTC stereo superlayers; this variable is only available for tracks reconstructed in three dimensions
- impact parameter: the distance of closest approach of the track to the primary vertex in the transverse plane
- z_0: the z coordinate of the distance of closest approach as defined for impact parameter; only available for tracks reconstructed in three dimensions
- ϕ_0: the ϕ direction of the track at the distance of closest approach as defined for impact parameter

After track reconstruction is performed in the CTC, an attempt is made to associate SVX hits with those CTC tracks extrapolating into the SVX fiducial volume. By considering the uncertainties in the CTC track parameters during the extrapolation to the SVX a search region known as a road is defined. This road is searched for SVX hits.

It is possible that a single ionizing particle may cause more than one SVX microstrip to be above threshold. In order that such cases not be counted as multiple hits, a clustering algorithm is run in which contiguous strips are associated with a single cluster. Dead channels within a cluster may be included. Candidate clusters are checked against a threshold to reject clusters from noise fluctuations. The threshold for a cluster is based on the size of the signal relative to the measured noise in each strip. The thresholds are given in table 2.2.

The spatial resolution of reconstructed clusters is then computed. For clusters with more than 3 strips, or those with a total charge $> 11.7\ fc$, the position error is set to (strip pitch $\times$ number of strips)$/\sqrt{12}$. For clusters with 3 or fewer strips, the resolution is derived

Number of Strips	Multiplicative Factor
One	4.0
Two	2.5
Three - Eight	2.0
$\geq$ Nine	1.5

Table 2.2: The multiplicative factor for signal–to–noise in SVX hit clustering, by number of strips in the cluster candidate.

Number of Strips	Computed Resolution
One	15 μm
Two	13 μm
Three	25 μm

Table 2.3: The cluster spatial resolutions derived for SVX clusters with fewer than four associated strips.

from the distributions of the residuals from the final track fits in the data. These resolutions are given in table 2.3.

For each cluster found, the track parameters and error matrix are updated to reflect the addition information given by the cluster location as well as multiple–scattering and ionization energy loss corrections. The updated track is extrapolated inward toward the beampipe and a new search road is computed. Since each new road may yield multiple candidate SVX clusters for the track, the result is often an assortment of possible SVX tracks. The selection of the unique assignment of SVX clusters for a given CTC track (assuming any appropriate SVX clusters are found) is based on two criteria: SVX track χ^2, and the number of SVX clusters used in the fit.

The SVX χ^2 is defined to be the addition to the total track χ^2 caused by the addition of the SVX cluster information. It represents not only how well the SVX clusters are described by the track parametrization but also how much the previous tracking results must be modified to accommodate the SVX information. The SVX χ^2 is the sum of the contributions from the addition of each cluster to the fit, with the contribution of a single

cluster given by:

$$\chi^2_{SVX} = (\delta\vec{p})^T\ C^{-1}\ (\delta\vec{p}) + \frac{(x_{track} - x_{cluster})^2}{\sigma^2_{cluster}}$$

where:

$\delta\vec{p}$ is a vector containing the change in track parameters

C is the covariance matrix associated with the track parameters

x_{track} is the intersection of the extrapolated track with the SVX layer

$x_{cluster}$ is the location of the associated cluster

$\sigma_{cluster}$ is the cluster resolution

and all locations are given in the local ladder coordinate system, in which the x axis runs along the outer surface of the silicon parallel with the short edge of the ladder. This convention is used only during track reconstruction.

A rough quality assessment of the SVX candidate tracks based on the χ^2 is used to reject poor fits. The likelihood of the track χ^2 is calculated based on the number of degrees of freedom in the SVX fit. Track candidates with

$$\mathcal{P}(\chi^2_{SVX}) > 10^{-4}$$

are retained for analysis.

There is a preference toward tracks with larger numbers of SVX clusters. Four–hit tracks (one hit on each SVX layer) are sought first. If any acceptable candidates are found the one with the lowest total SVX χ^2 is chosen and that track is considered to be fully reconstructed. If not, then the program searches for tracks in which one layer of the SVX does not have a cluster associated with the track (a three-hit track). The missing hit may be caused by geometric factors such as detector gaps, by dead or noisy regions of the detector, or by a failure in reconstructing a cluster from a hit. The three–hit track with the lowest total SVX χ^2 is chosen from the available candidates, and if none is found the search continues by seeking two–hit tracks. SVX tracks with only one SVX hit are not considered, though such tracks do exist.

Although there are regions of overlapping coverage at wedge boundaries, giving the possibility of two hits from a particle on a given layer, only one of the two hits is used. The choice is made based on the χ^2 criteria given above. Finally, those tracks with unphysical characteristics, such as those crossing module boundaries more than once, are rejected.

Not all CTC tracks which extrapolate through the SVX are associated with SVX hits in the track reconstruction process. The efficiency with which tracks through the SVX fiducial region are reconstructed depends both on the tracking algorithm used and the physical performance of the detector. Because the performance of the detector decreased with time due to radiation exposure, the tracking efficiency decreased during the run. This is addressed in the following section.

2.4.3 Radiation Damage to the SVX

The radiation environment at a hadron collider is not favorable for the SVX. The leakage currents in the silicon detectors increase with accumulated radiation dosage. The DC–coupled CMOS read–out chips used are a rad–soft design which saturate at a leakage current of about 80 nAmp. The signal-to-noise of these chips is also adversely affected by radiation damage. The net result of the radiation damage is a decrease in the signal-to-noise ratio for the SVX with increased exposure. Testing of SVX prototype ladders suggested that a dose of approximately 15 *krad* would result in a factor of two degradation in the signal-to-noise ratio, and this was defined as the limit of acceptable performance loss for the detector.

To insure that the radiation exposure of the SVX was kept to a minimum, a system of monitors and alarm/abort systems was used. Sealed glass ion chambers (Beam Loss Monitors, or BLM's) were placed on the beampipe in the plug regions of the detector (approximately 2 m from the center of CDF) to give measurements of the ionizing dose levels on short time scales. The BLM's were read-out through logarithmic integrating amplifiers having time constants of 100 ms. The information from the BLM system was sampled at 5 KHz by a CAMAC–based analog-to-digital converter. These integrated values were stored

in $2K$ circular buffers, which provide a recent-history snapshot of interesting dosimetry events, as well as being fed to a software monitoring system maintaining running sums of the total dosage. The dose rates were compared against abort limits to offer protection against Tevatron irregularities. If the instantaneous dose exceeded the set values ($10\ rad/sec$ during beam injection and orbit adjustments at the beginning of a store, $2\ rad/sec$ during normal running) then a control mechanism removed a beam-permit signal and caused the Tevatron to dump all bunches into concrete absorbers. For situations in which the accumulated dosage was severe but the instantaneous rate was not high enough to trip the abort system, a protocol between the CDF control room and the Tevatron operations control room provided for the termination of the beam if the dose for any given store exceeded $100\ rad$ as measured by the BLMs.

The BLMs were cross-calibrated by using sets of thermo-luminescent diodes (TLDs) placed at the same locations along the beampipe as the BLMs. Arranged in concentric circles about the beampipe at three radii, the TLDs also allow observation of the radial and azimuthal dependence of the dose. However, the TLDs require extraction for determination of radiation exposure, and thus data from the TLDs is not available for loss protection purposes.

There were numerous difficulties in the early stages of Run 1a, resulting in numerous beam aborts. Figure 2.7 shows a small number of large accidents. The Tevatron operation was much smoother for the bulk of the data taking and, as seen in figure 2.8, about one third of the total SVX dose was accumulated during the first 10% of the delivered luminosity of the run. The steady increase in radiation exposure after the initial problems is from losses during beam injection and from beam-beam interactions. These unavoidable doses were present at a level of $\sim 350\ rad$ per pb^{-1} of delivered luminosity during most of the run.

The radiation damage to the SVX had an adverse affect on its tracking capabilities. The decreased signal-to-noise from the exposure results in a failure to reconstruct some clusters from hits ("lost hits") as well as spurious clusters formed from the increased noise ("junk hits"). The loss of information from lost hits decreases the tracking resolution,

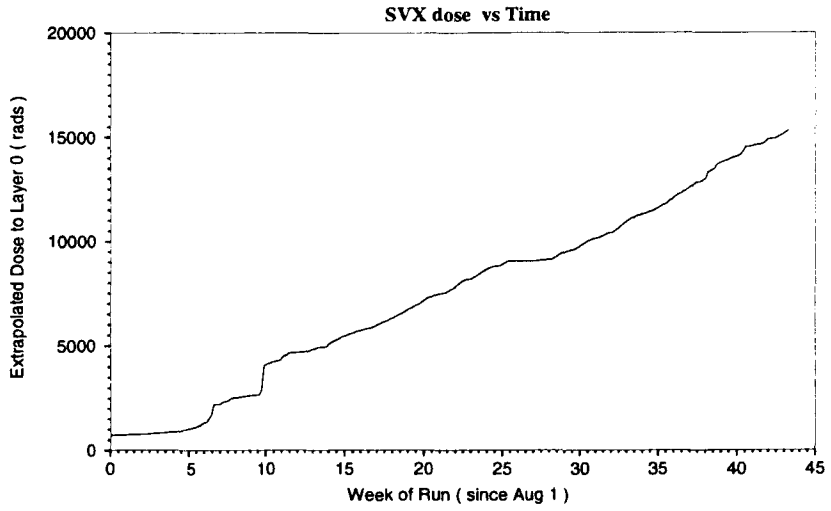

Figure 2.7: The estimated dose to the innermost layer of the SVX as a function of time. The value is extrapolated from the daily recordings of BLM dosage, using the a radial fit derived from the TLDs and a correction factor for the difference in z position of the BLMs and the SVX.

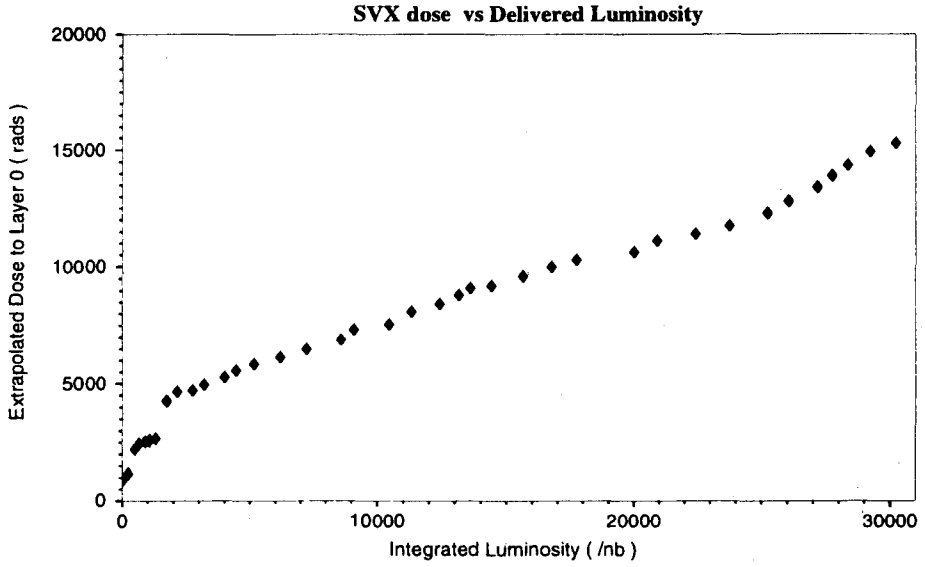

Figure 2.8: The estimated dose to the innermost layer of the SVX as a function of delivered luminosity.

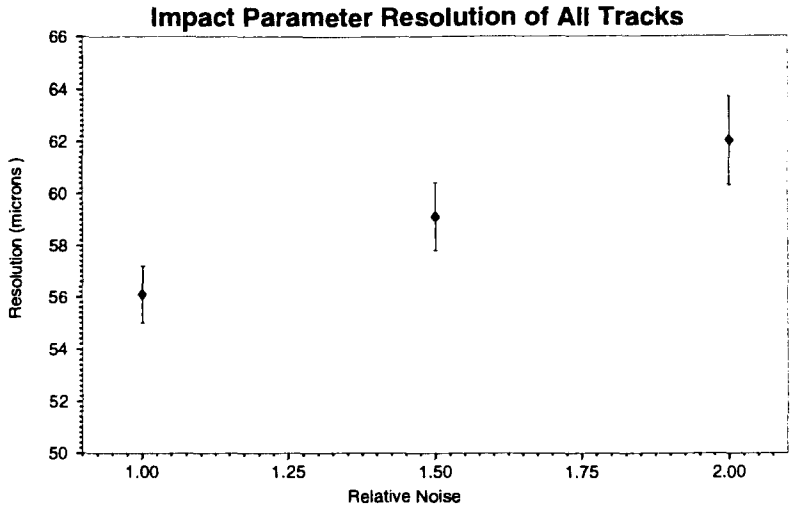

Figure 2.9: SVX impact parameter resolution of all tracks as a function of increasing noise. Based on Monte Carlo simulation of radiation damage.

while the junk hits worsen the resolution by introducing erroneous information during the track reconstruction process. These problems were studied by using a detailed detector simulation to model the effects of the radiation damage on a layer-by-layer basis, as well as measured from the data. From the studies, it was determined that making additional quality requirements on the SVX tracks permitted the recovery of the impact parameter resolution, albeit at the expense of efficiency. Adding the requirements of

- Track $P_T \geq 1.5$ GeV/c
- Track SVX $\chi^2 < 20$
- No 2-hit tracks in which the only hits are on layers 0 and 1

is sufficient to maintain the impact parameter resolution, as shown in figure 2.10. A detailed discussion of the impact parameter resolution is given in chapter 3.

Figure 2.11 shows the net resultant loss of efficiency required to maintain constant impact parameter resolution, using the cuts listed above, as a function of the relative increase

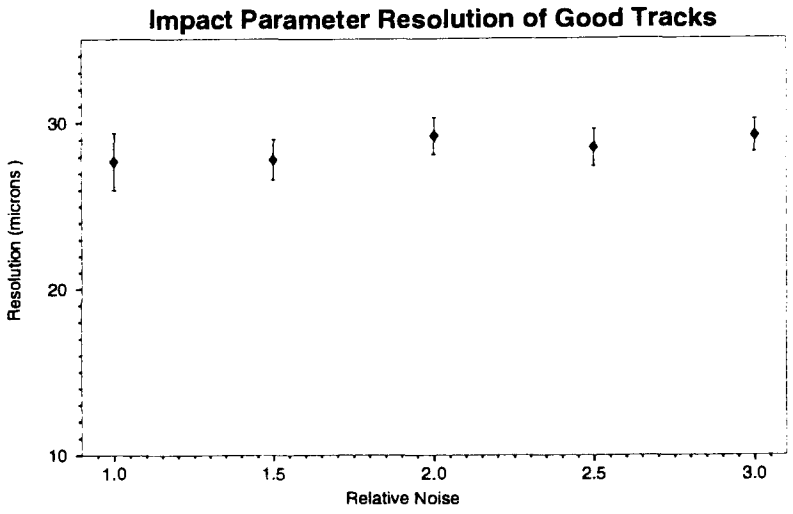

Figure 2.10: SVX impact parameter resolution as a function of increasing noise, with quality cuts. Based on Monte Carlo simulation of radiation damage.

in noise. Furthermore, the Monte Carlo study suggests that the ratio of 4-hit:3-hit:2-hit tracks should change as the radiation damage increases. This is the result of the loss of hits on the inner layers, which receive higher doses.

The data show the effects of radiation damage as predicted by Monte Carlo. SVX hit efficiencies are calculable by observing the fraction of CTC tracks extrapolating into the SVX fiducial volume which are associated with SVX hits. The hit detection efficiencies early in the run, when the radiation damage was minimal, are given in table 2.4. These values include inefficiencies caused by dead channels and gaps in the detector.

The decreased efficiencies given in table 2.4 for data taken late in the run include the presence of an increased number of bad channels. While only about 1% of the strips were bad at the beginning of the run, that fraction had increased to typically 5-6% on the inner layers and 1.5-2% on the outer layers by the end of the run. The signal–to–noise ratio on layer 0 decreased by about 28% during the run, primarily due to radiation damage.

The distribution of the number of clusters per SVX track also changed. The values

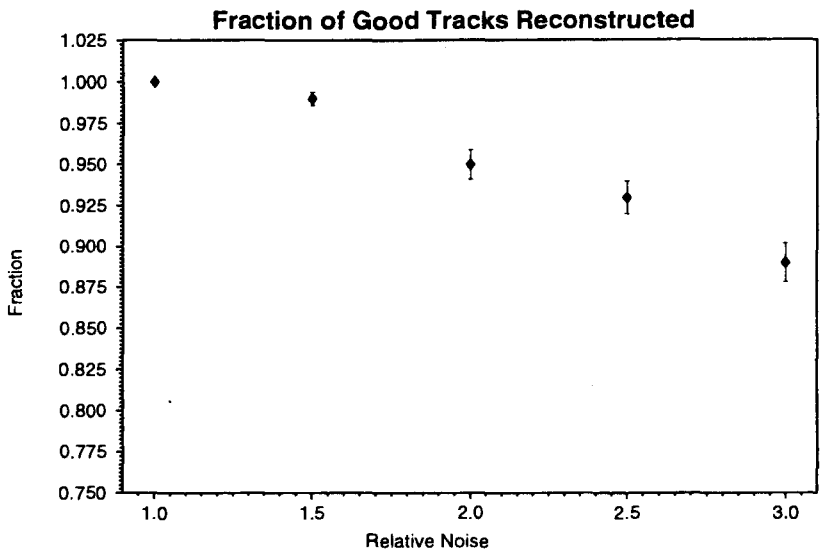

Figure 2.11: Relative number of good tracks remaining after radiation-required quality cuts as a function of noise, based on Monte Carlo studies.

SVX Layer	Hit Detection Efficiency (Early)	Hit Detection Efficiency (Late)
0	93%	89%
1	93%	85%
2	93%	91%
3	91%	89%

Table 2.4: Typical SVX hit detection efficiencies, by layer. Values listed are for measurements taken early in Runla and late in Run 1a.

Number of Hits	Early	Late
4	71.9%	59.7%
3	23.5%	31.4%
2	4.6%	8.8%

Table 2.5: The distribution of the number of SVX hits associated with SVX tracks for data early in the run compared with late in Run 1a. The difference is largely due to radiation damage, with more of the lost hits being on the inner layers. Typical statistical errors on the efficiencies are 1-2%.

for the early and late stages of the run are given in table 2.5. The overall tracking efficiency of the SVX dropped from 98% at the beginning of the run to 97% at the end.

Chapter 3

Impact Parameters and Displaced Vertices

The usefulness of the SVX in detecting displaced vertices from particle decays stems from its ability to measure the impact parameters of the decay products with high precision. In this chapter the concept of the impact parameter and its relation to displaced vertices is discussed.

3.1 Origin of the Impact Parameter

The impact parameter of a track is defined as the distance of closest approach of the track to the primary vertex of the event in the plane transverse to the beamline, with a sign determined by tracking convention. For tracks from the primary vertex, the impact parameter would ideally be zero. In reality, detector resolution, track reconstruction errors, and uncertainty in the location of the primary vertex result in the non–zero impact parameter of tracks from zero–lifetime sources (prompt particles or those from exceedingly short-lived particles) smeared in a near-Gaussian manner about zero.

Tracks associated with particles from sufficiently displaced decays do not necessarily extrapolate to the primary vertex. As shown schematically in figure 3.1, tracks from a displaced vertex can have a range of impact parameters before tracking resolution is taken into account. A particle travelling with speed βc in the lab frame, decaying after the proper time interval t, travels a distance $x = \beta ct/\sqrt{1-\beta^2}$ in the lab frame. The impact parameter

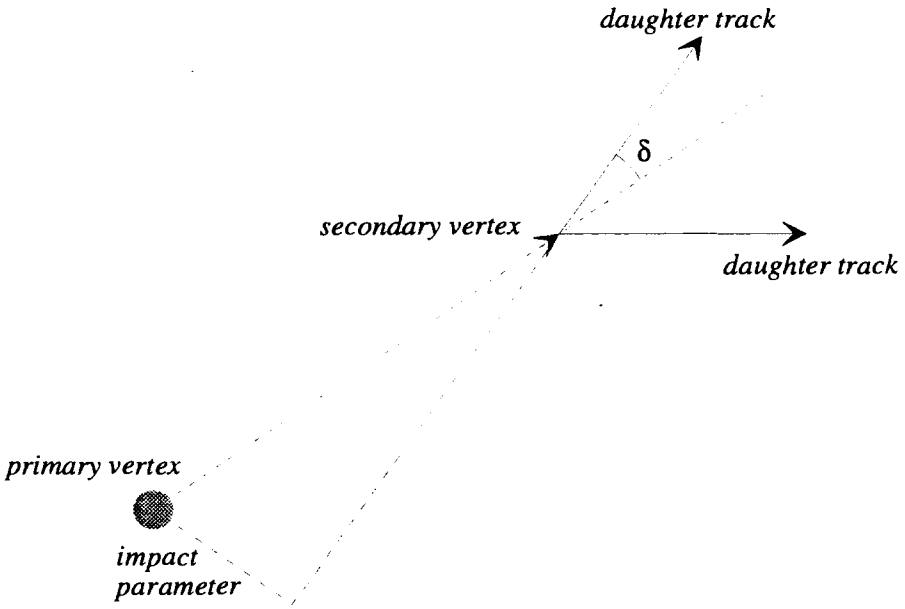

Figure 3.1: Origin of non-zero impact parameters from secondary vertices. Represented is the decay of a short–lived particle from the primary vertex of the event. See the text for discussion.

of a daughter track is determined by the distance travelled by the parent particle and the decay angle of the daughter with respect to the original path of the parent. For a decay product produced at an azimuthal angle δ in the lab frame, the impact parameter of the extrapolated track is $d_0 = \beta ct \sin\delta/\sqrt{1-\beta^2}$.

Analytic calculation of the impact parameter distribution for decay products of a particular process is typically difficult. The exponential distribution of the proper decay times of the parent particle must be convoluted with the energy spectrum for the production of that particle and then the various decay modes considered. For this analysis, all theoretical predictions concerning the tracks from hadronically decaying tau leptons are obtained by Monte Carlo, using the ISAJET [29] event generator and a detailed simulation of the CDF detector.

3.2 SVX Impact Parameter Resolution

The statistical significance of a measured impact parameter depends on the uncertainty of the measurement. For SVX tracks, this uncertainty depends both on the quality of the track reconstruction and on the knowledge of the location of the primary vertex. Considered first are the factors which contribute to the uncertainty in the process of track reconstruction.

Though the silicon microstrips are small compared to many other components of the CDF detector, they are of finite extent and thus limited resolution (see table 2.3). The contributions from scattering and energy loss as the particles traverse the material in the detector are added in quadrature to the uncertainty caused by the detector geometry. The resulting uncertainty, is plotted for a sample of SVX tracks in figure 3.2 as a function of the reciprocal of the transverse momentum of the particles. A fit of this distribution to

$$\sigma_{ip} = \sqrt{\sigma_{geom}^2 + \left(\frac{\sigma_{scattering}}{P_T}\right)^2}$$

yields $\sigma_{geom} = 16\mu m$ and $\sigma_{scattering} = 44\mu m$ – GeV/c. While the geometry determines the asymptotic resolution of the detector in the limit of an infinite–momentum track, the effects of multiple coulomb scattering dominate the impact parameter resolution of the SVX for most tracks.

The utility of a well-measured track is greatly minimized if the primary vertex location is not known for the event in question. In addition to the distribution of the primary vertex along the z axis caused by the lengths of the particle bunches in the Tevatron (see appendix B), the interaction region has a non-negligible width caused by the transverse extent of the proton and antiproton bunches. The beam spot is about 40 μm across in the $x - y$ plane of the detector, which is larger than the tracking resolution of the impact parameters of high P_T tracks. While the VTX provides a measurement of the longitudinal location of the primary vertex on an event–by–event basis, the SVX is the only detector at CDF capable of measuring locations in the transverse plane accurately enough to notice the beam width.

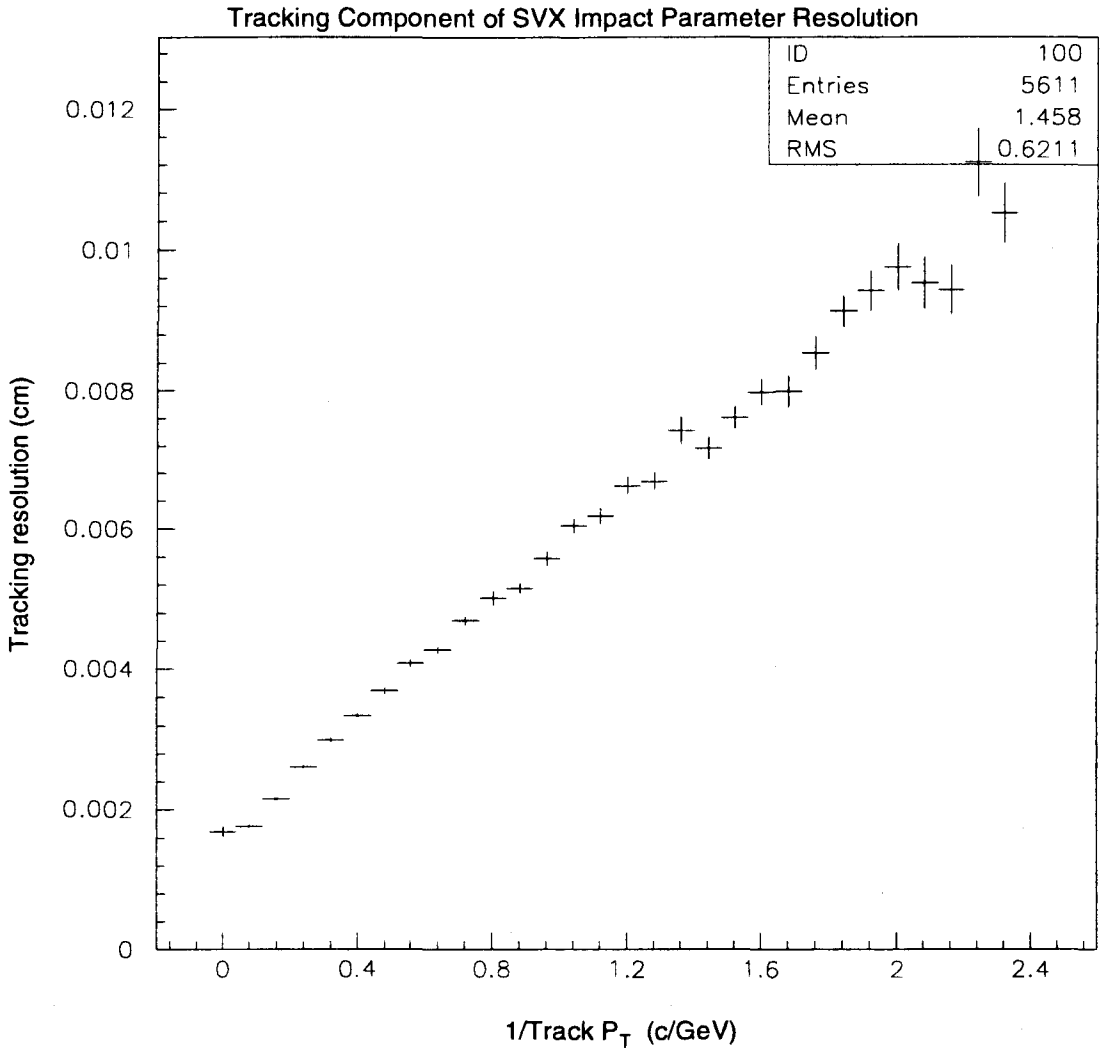

Figure 3.2: SVX impact parameter resolution versus $1/P_T$. The asymptotic behavior of the tracking–based error is seen in the left–most bins of the plot, where the intercept with the vertical axis is non–zero.

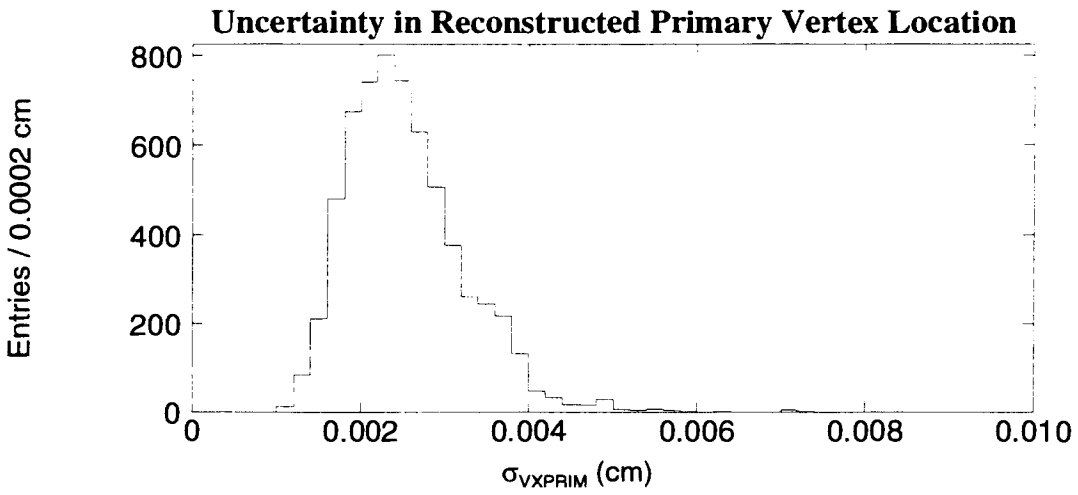

Figure 3.3: The uncertainty of the primary vertex location in the transverse plane for typical events at CDF.

To reduce the uncertainty in the primary vertex location, a vertex–locating algorithm is used. The primary vertex module (*VXPRIM*) weights SVX tracks by P_T and minimize the residuals of the tracks with respect to a fit point in space. This operates under the assumption that most of the tracks in the event come from the primary vertex, which is a valid assumption for the most events. To further improve the estimate of the primary vertex, *VXPRIM* is run on a large number of events during each store to map the interaction region. By maintaining the values for the slopes and intercepts of the beamline (betatron oscillations in the Tevatron cause the beamline to be slightly non-parallel with the CDF coordinate system) for each store, it is possible to use the z position obtained from the VTX to obtain a starting point for use in *VXPRIM*. By adding track information to this seed location, the primary vertex position is often determined to 20 μm in the transverse plane (see figure 3.3). For most tracks studied in this thesis, the error on the impact parameter is dominated by the uncertainty in the primary vertex location.

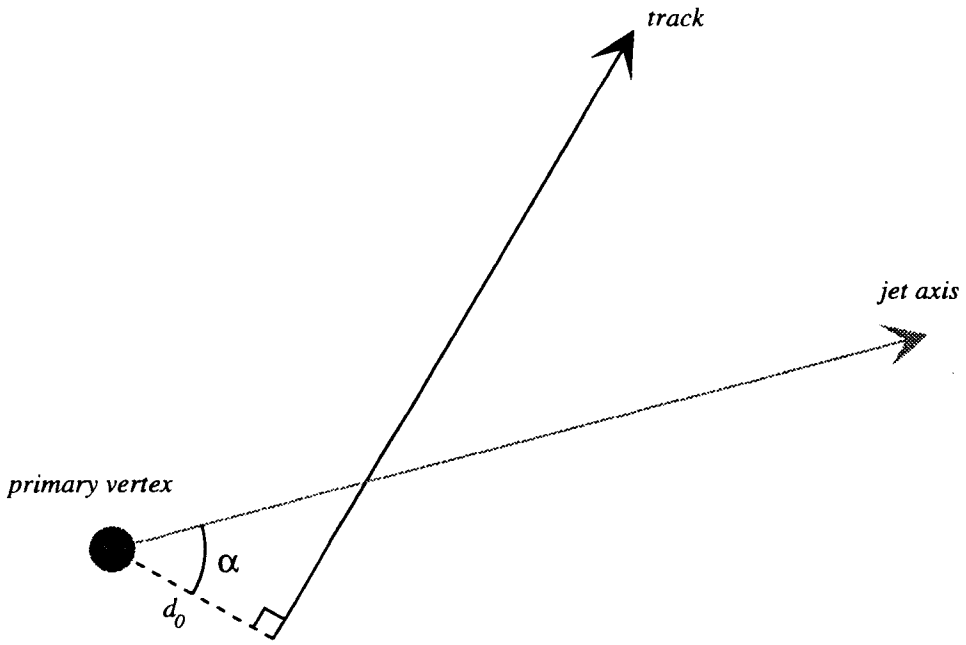

Figure 3.4: A symbolic view of the intersection of a track with a jet axis in the plane transverse to the beamline.

3.3 Signed Impact Parameter

The magnitude of the impact parameter is the distance of closest approach, as discussed above. However, there are no restrictions in the choice of a sign for the impact parameter. Rather than using the CDF convention for determining whether an impact parameter is given a positive or negative sign, a convention is chosen which preferentially chooses tracks from displaced vertices as being positive. This signed impact parameter utilizes the knowledge that the secondary decay products of interest come from energetic particles and are boosted in the same general direction as the parent particle.

The direction of the resultant jet (see section 2.3.2) is taken to be a good approximation of the direction of the decaying particle. The impact parameter d_0 (see figure 3.4)

is given a sign based on the angle α between the axis of the jet with which the track is associated and the line along which the impact parameter is measured according to the following prescription:

$$\text{sign of impact parameter} = \begin{cases} \text{positive}, & \text{if } \alpha < 90°; \\ \text{negative}, & \text{if } \alpha > 90°; \\ \text{zero}, & \text{otherwise.} \end{cases}$$

As seen in figure 3.1, tracks from the decay of energetic particles will intersect the the path of the parent particle "in front of" the primary vertex, resulting in $\alpha < 90°$.

Negative signed impact parameters result from two effects: resolution and sign flipping. The effect of limited resolution is the smearing of the measured impact parameters such that tracks from zero-lifetime sources have non-zero impact parameters. The sign given to such resolution-dependent impact parameters is random because there is no correlation with jet activity. Some fraction of displaced tracks are also given a negative signed impact parameter due to resolution effects, when the tracks are sufficiently mismeasured that the track is no longer consistent with having come from a displaced vertex. It is important to note that resolution effects concern not only the sign but also the magnitude of the impact parameter.

In contrast, the effect of "sign flipping" affects only the sign of the impact parameter and not its magnitude. Implicit in the determination of the sign of the impact parameter is the knowledge of the direction of the associated jet. The internal segmentation of the calorimeters, the presence of unmeasured or mismeasured particles, and the effects of the jet clustering algorithm in determining the jet direction all contribute to some uncertainty in the direction of the jet. Tracks associated with a jet whose axis is sufficiently different from the true direction of the parent particle can be erroneously signed.

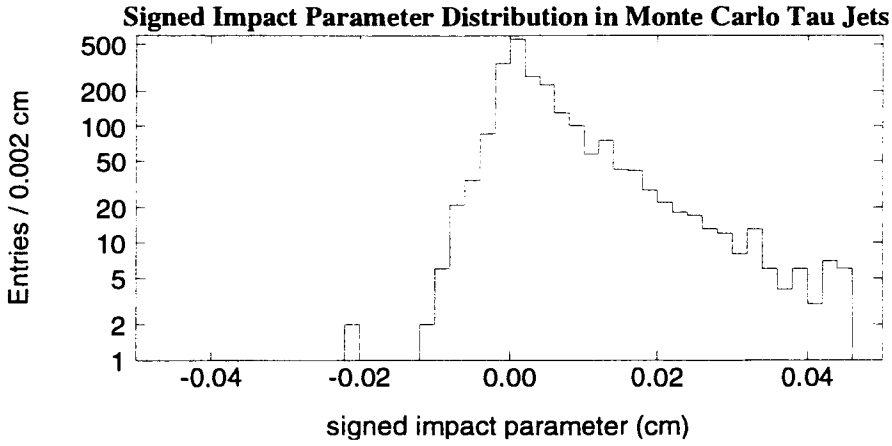

Figure 3.5: The signed impact parameter distribution of Monte Carlo tau tracks, with respect to the true τ direction.

3.4 Monte Carlo Studies of Taus

Before considering the data, the utility of the SVX in the identification of hadronic tau jets is examined by detailed Monte Carlo simulation. In this section, events of the form $W \longrightarrow \tau\ \nu_\tau$ are used as a source of hadronic decays from highly energetic taus. The simulations used the current world average tau lifetime $295.7 \pm 3.2\ fs$.

Considered first is the signed impact parameter distribution of the tau-descendent tracks with respect to the true (Monte Carlo) tau direction. This procedure, which cannot be duplicated in the data, represents the best case scenario. Because the true τ direction is used, there is (definitionally) no sign–flipping in figure 3.5. The only cause for the non-ideal presence of negative sign impact parameters are the tracking resolution and primary vertex errors.

Figure 3.5 reveals several points of interest. Most important for this analysis is the marked surplus of entries for positive signed impact parameters. This indicates that the sign convention used is robust with respect to effects from tracking resolution. Secondly, the distribution peaks at zero. This is a consequence of the daughter particles following roughly

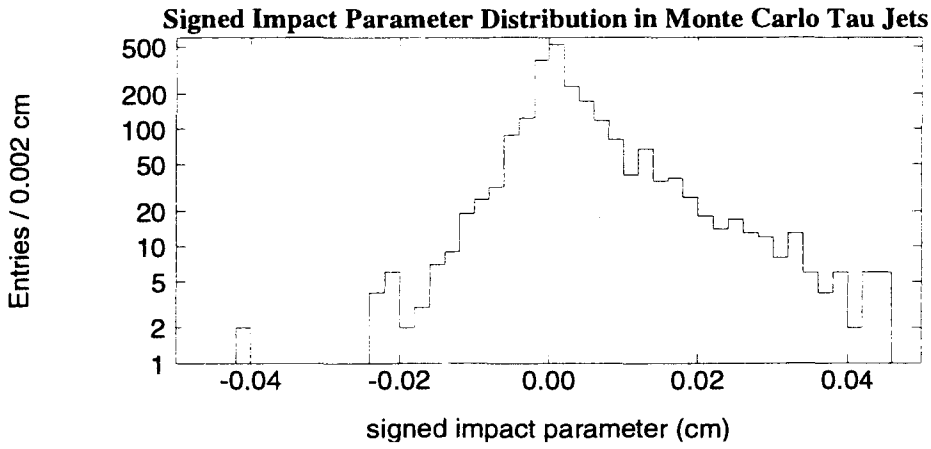

Figure 3.6: The signed impact parameter distribution of Monte Carlo tau tracks, with respect to the calorimeter jet direction.

the same direction as the parent tau thereby extrapolating back toward the primary vertex. Note that those entries on the negative side are near zero, while the positive tail extends out beyond 400 μm. The absence of tracks with large, negative signed impact parameters is contrasted with the signed impact parameter distribution when the reconstructed jet axis is used for the determination of the impact parameter sign (figure 3.6).

Because the only difference between figure 3.5 and figure 3.6 is the definition of the jet axis used, the sole change is the addition of any sign–flipping. The negative side of the distribution has a non-Gaussian shape because of the random addition of tracks from the positive side, and the positive side suffers a corresponding decrease in statistics. The Monte Carlo predicts that sign–flipping causes the erroneous signing of about 35% of tracks from tau decay.

As shown in chapter 4, the distribution of the signed impact parameters for tau-descendent tracks is sufficiently different from the expected backgrounds.

Chapter 4

Selection of Control Samples

In the development of any selection criteria, it is necessary to have a test sample with which to validate the technique. It is also helpful to have a data set representative of the background to the signal being sought. In this chapter the two control samples chosen to validate the tau tagging algorithm are detailed.

4.1 Selection of $W \longrightarrow \tau\ \nu_\tau$

To study the tau tagging algorithm developed in chapter 5 a sample enriched in hadronic tau decays is constructed. This analysis uses events of the type $W \longrightarrow \tau\ \nu_\tau$ (with no other jets associated with the W production) to obtain a statistically useful sample of high-energy taus. Such "monojet" events are well-suited for control studies because the taus produced are typically isolated from other particles in the events.

Monojet events are characterized by an energetic jet from the tau, no other jet activity, and missing energy from the neutrinos. The tau comes from the decay of a real W boson, and as such is usually highly relativistic in the lab frame. The decay products of the tau are significantly boosted, resulting in a highly-collimated jet in the detector.

It is not necessary to search the entire CDF data set to look for such events. During the offline processing of the data, the events were split into different streams corresponding to different physics interests. One such stream is the Exotics stream, where events which

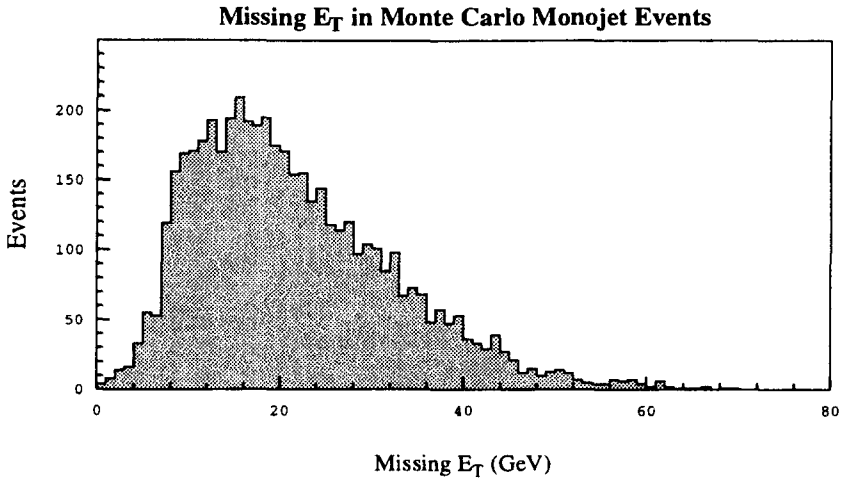

Figure 4.1: The missing transverse energy in Monte Carlo monojet events.

satisfy various Level 3 triggers for large $\not\!\!E_T$ or τ candidates are split off from the rest. The search is confined to the Exotics stream in this portion of the analysis, without particular attention given to which of the many possible triggers allowed the events. More rigorous requirements are imposed in later chapters during the calculation of the cross–sections to avoid complications arising from overlapping trigger criteria.

A restriction of 25 GeV $\leq \not\!\!E_T \leq$ 40 GeV is used in selecting the control sample, with cuts motivated by Monte Carlo studies of the likely neutrino energies in $W \longrightarrow \tau\ \nu_\tau$ events (see figure 4.1). Furthermore, as the events sought are those in which the tau jet is the sole jet in the event, events in which there is more than one jet of $E_T > 10$ GeV are rejected. Those events with more than 75 GeV total transverse energy are discarded, because Monte Carlo shows these are unlikely to be W events (see figure 4.2).

The topological cuts listed above are not sufficient to produce a suitably pure τ sample, so additional constraints are placed upon the tau candidate jet in each event to increase the fractional τ content of the sample. The selection criteria are:

- $|\eta_{detector}| < 1.1$, to select only events in the central calorimeter

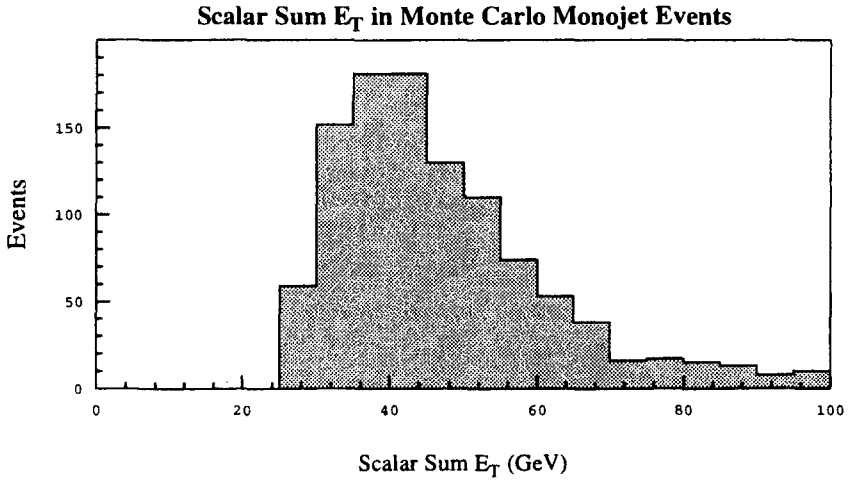

Figure 4.2: The scalar sum transverse energy in Monte Carlo monojet events, after jet and $\not\!\!E_T$ cuts.

- 15 $GeV \leq E_T \leq$ 40 GeV
- At least one SVX track of $P_T \geq$ 5 GeV/c within 10° of the jet axis
- No SVX tracks with $P_T \geq$ 1 GeV/c within the 10° – 30° annulus about the jet axis
- Charged track invariant mass $\leq$ 2 GeV/c^2
- Not an electron

Since this analysis pursues an SVX-based algorithm, only those events in which the jet is within the SVX fiducial region are considered. This is accomplished by demanding that the jet axis (as defined by calorimetry) be such that a track along the jet axis would hit at least 3 layers of the SVX. The short length of the SVX means most such jets are in the central calorimeters, but this is insured by the explicit requirement on the $\eta_{detector}$ of the jet.

There is also the requirement of at least one SVX track associated with the tau-candidate jet. To assign a track as being part of a jet, a cut on the separation of the track

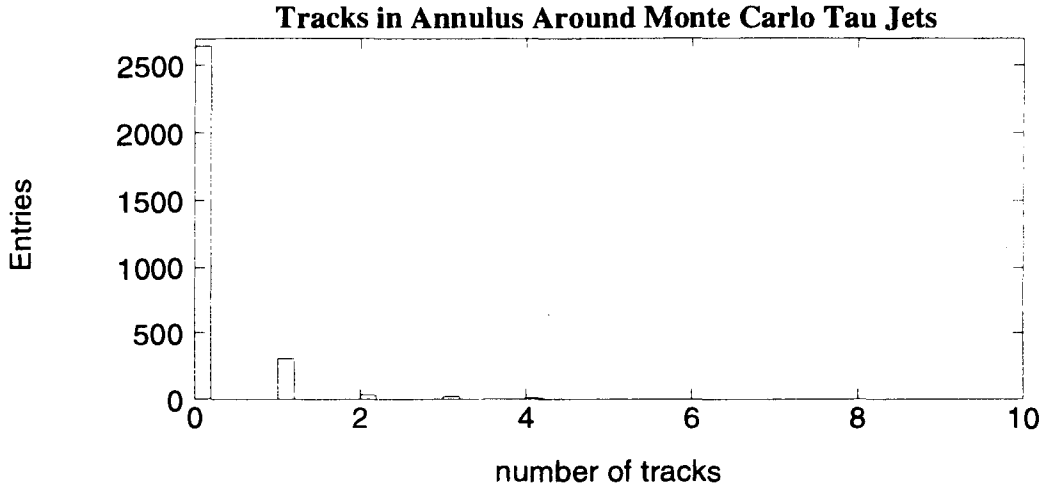

Figure 4.3: The number of tracks with $P_T \geq 1$ GeV/c in the $10° - 30°$ annulus about the jet axis for Monte Carlo tau jets.

and the jet axis in $\eta - \phi$ space, $\Delta R = \sqrt{(\Delta\phi)^2 + (\Delta\eta)^2}$ is made. While a value of $\Delta R \leq 0.4$ is more common for CDF analyses, the highly-collimated nature of the taus in question permits a more stringent limitation of $\Delta R \leq 0.1745$. This value is used by convention, and corresponds to cone whose half-angle is $10°$ in ϕ. Low momentum debris from the underlying event is excluded by requiring that associated tracks have $P_T > 1$ GeV/c.

The tau jets of interest are typically spatially isolated from other objects in the event. The tracking isolation of candidate tau jets is given by the number of tracks of $P_T \geq 1$ GeV/c within the annulus defined by $0.1745 \leq \Delta R \leq 0.5236$ $(10° - 30°)$ about the jet axis. Only those jets with a tracking isolation of zero are kept. Figure 4.3 shows the Monte Carlo prediction for the tracking isolation of τ jets in $W \longrightarrow \tau\ \nu_\tau$ events.

The background can be further reduced by placing an upper-limit on the invariant mass of the charged tracks associated with the tau candidate jet. The mass should be less than the mass of the tau lepton (1.784 GeV/c^2), with some variation due to tracking resolution. A cut of 2 GeV/c^2 prevents undue loss of signal. While this restriction does not remove a large number of background events, the type of background removed is significant.

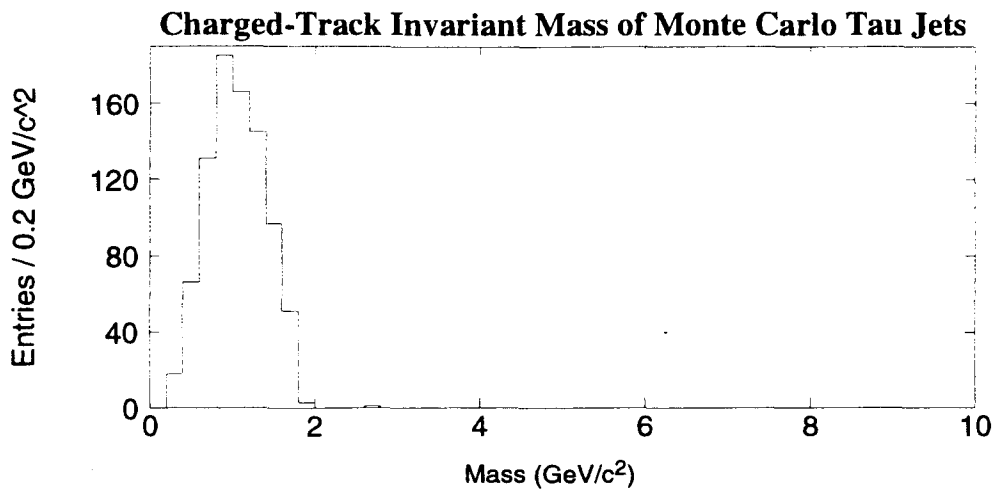

Figure 4.4: The charged–track invariant mass of hadronic tau jets in Monte Carlo. A cut at 2 GeV/c^2 is > 99% efficient. One track jets are not shown.

A mass requirement preferentially removes heavy flavor (especially jets from bottom quarks) from the sample. This is important, as the decays of B mesons result in displaced vertices which might be mistaken for those from tau decays. Figure 4.4 shows the expected mass distribution of the tau jets, based on Monte Carlo. The distribution for the background is discussed in section 4.2.

Nothing in the above cuts would necessarily reject electrons, and in particular, events of the type $W \longrightarrow e\ \nu_e$ pass these criteria and occur more often than the hadronic $W \longrightarrow \tau\ \nu_\tau$ events sought. An electron rejection algorithm explicitly removes these events. The comparatively low rest mass of the electron means that for relativistic electrons (any electron passing the E_T requirement is highly relativistic) one can make the approximation that $E = |\vec{p}|$. Taking into account the calorimeter response, it has been shown [31] that placing a cut of

$$\frac{E_{EM}}{E_{EM+HAD}} < 1 - \frac{P}{7 \times E}$$

will remove > 99% of electrons while retaining almost all hadronic tau jets.

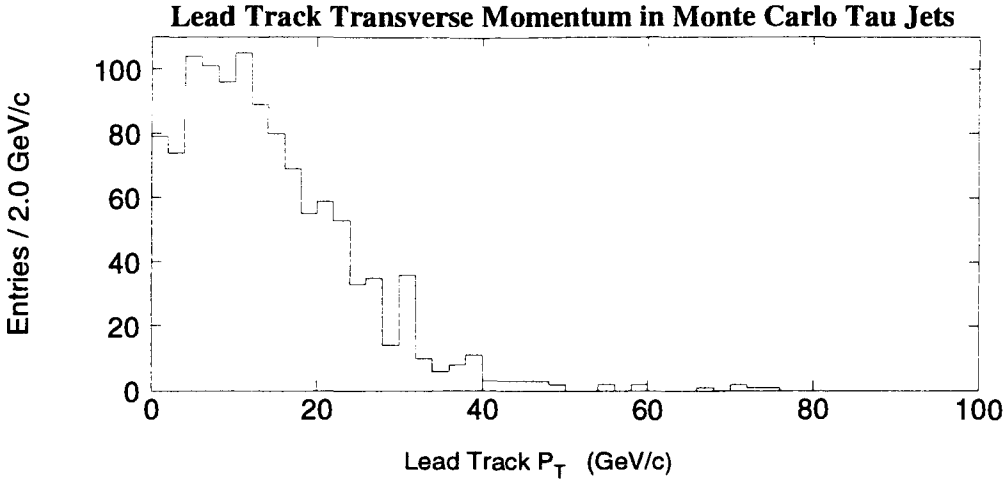

Figure 4.5: The P_T of the most energetic SVX track in Monte Carlo tau jets.

Because impact parameter measurements from the SVX are of prime interest, it is necessary to insure that large impact parameters are not merely the result of a poorly determined primary vertex for the event. Events are listed as having suitably reconstructed vertices if the transverse error meets the following condition:

$$\sigma_{VXPRIM} \equiv \sqrt{\sigma_x^2 + \sigma_y^2} \leq 40\mu m$$

A detailed discussion of the efficiencies for these cuts is given in the context of the cross-section calculations, and is found in section 6.1.3.

When the above selection criteria are applied to the Exotics stream, a data set containing 721 events remain. This is the monojet sample.

4.2 Selection of JET_20

The dominant source of background events in the monojet sample is QCD dijet events in which one jet is badly mismeasured or is missed by the detector altogether, giving a large amount of missing energy. Whether such an event passes the remaining tau selection

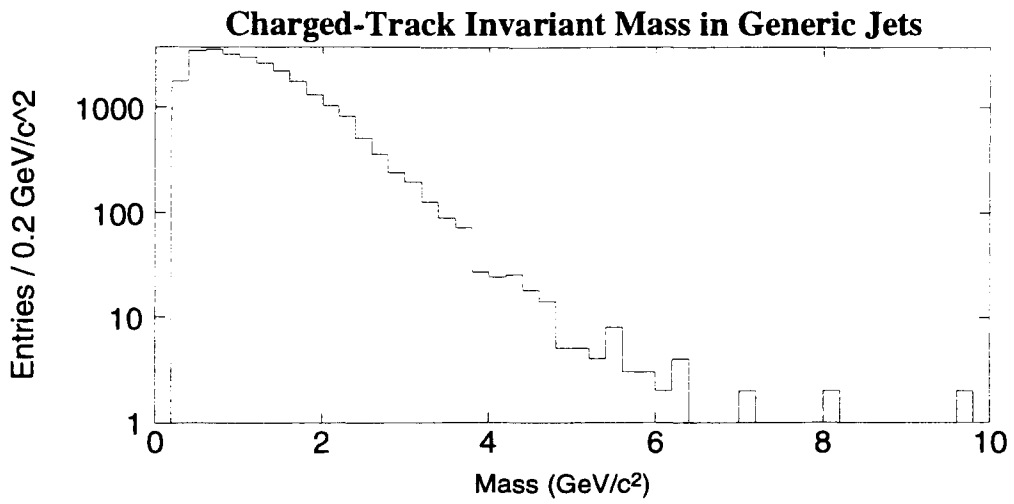

Figure 4.6: The charged–track invariant mass of generic jets in the JET_20 sample. One track jets are not shown.

criteria then depends only on the characteristics of the jet that was reconstructed. To study these jet properties, and thus better characterize the expected background, a sample of QCD dijet events is split from the data and the leading (most energetic) jet is considered.

The CDF trigger scheme for Run 1A includes a calorimetry-based trigger (JET20) which selects events with one or more jets of 20 GeV transverse energy as determined by the level 2 trigger. Events passing this trigger have a leading jet in an energy range comparable to those expected for the tau monojet sample. Energy–dependent variations with this range are found to be negligible.

From $\sim$ 85,000 JET20 events, only those whose lead jet meets the same jet selection criteria as the tau candidate jets in the monojet sample (see section 4.1) are kept. A sample of 2,993 such events remain from the data in Run 1a. The need to match the jet selection criteria as closely as possible to model the background has the consequence of rejecting most of the QCD events. The charged–track invariant mass distribution for the JET_20 sample is shown in figure 4.6.

Since there are few neutrinos in dijet events, the amount of missing energy JET_20

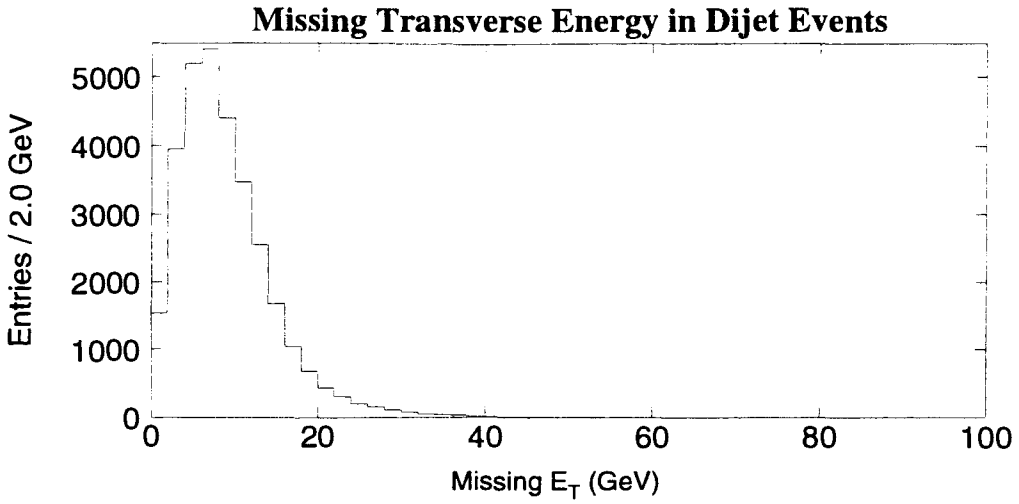

Figure 4.7: The missing transverse energy distribution in generic dijet events.

sample is primarily determined by detector effects. This makes the JET_20 sample useful in characterizing events in which large $\not\!\!E_T$ is from non-physics sources. The $\not\!\!E_T$ distribution for the JET_20 sample is shown in figure 4.7.

The signed impact parameter distribution for the JET_20 sample is shown in figure 4.8. The distribution is nearly symmetric about zero, with only a slight positive surplus. This small positive excess corresponds to the small amount ($< 2\%$) of heavy flavor present in the sample. The plot is normalized to unit area, and one can clearly see that nearly all the tracks are within 100 μm of the origin. This is in sharp contrast to the signed impact parameter distribution for the Monte Carlo tau jets (figure 3.6), which extends to 400 μm. It is this difference that is exploited in the identification of taus with the SVX, as detailed later.

4.3 Measuring Tau Fraction with Track Multiplicity

The utility of the monojet sample depends on the knowledge of the tau content of the sample. In this section the purity of the monojet sample is determined from the

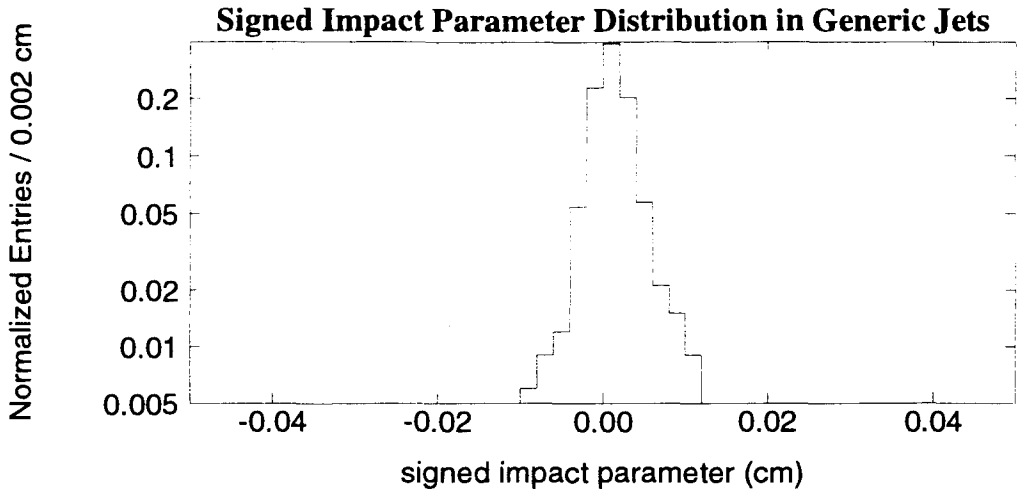

Figure 4.8: Signed impact parameter distribution in the generic jet sample.

charged track multiplicity distribution, a method independent of the impact parameters of the tracks. This provides a confirmation of the presence of taus in the control sample, and will be used later in the analysis.

4.3.1 Tau Track Multiplicity

Electric charge conservation requires the singly-charged tau lepton to decay to an odd number of charged tracks. The branching fractions for the tau show that those decays resulting in a single charged track ("one-prong taus") dominate, with a smaller number of 3-prong taus and a few 5-prong or higher.

In practice, one does not always find an odd number of charged tracks with tau jets. Tracking inefficiencies and selection criteria can result in the loss of one or more tracks, and tracks from the underlying event may be found within the tau jet. Both of these limitations tend to produce 2-prong tau jets. These effects can be adequately modeled using Monte Carlo, shown in figure 4.9.

A sample enriched in tau decays is expected to have a charged track multiplicity

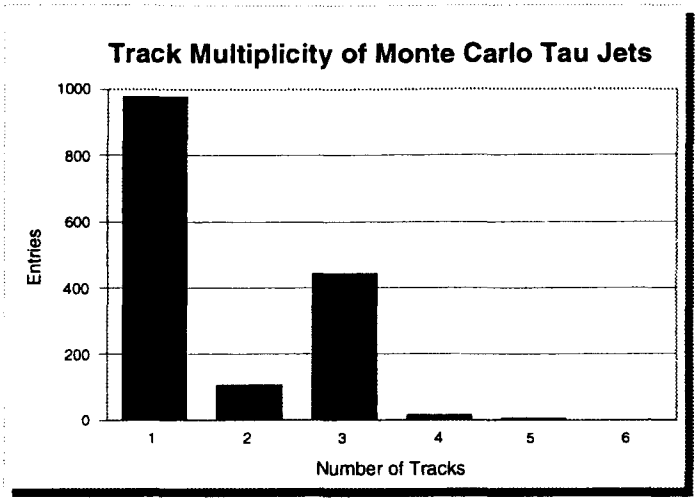

Figure 4.9: Charged track multiplicity distribution for hadronic tau decays in monte carlo monojets

distribution which exhibits these 1–prong and 3–prong peaks, which is seen in the monojet sample (figure 4.10).

4.3.2 QCD Track Multiplicity

The charged track multiplicity distribution for the QCD control samples is shown in figure 4.11, and is noticeably different from the Monte Carlo tau track multiplicity distribution in figure 4.9. Rather than pronounced peaks in the 1-prong and 3-prong bins, the histogram for the background sample shows a smoother distribution which peaks in the 2-prong bin. The distributions are sufficiently distinct that is it possible to determine the fractional tau content of the monojet sample.

Note that the track multiplicity distribution is, in general, dependent on the energy spectrum of the sample. However, for the limited kinematic regime of interest here, the track multiplicity is well-behaved and does vary measurably with the E_T of the jets. This is demonstrated in figure 4.12.

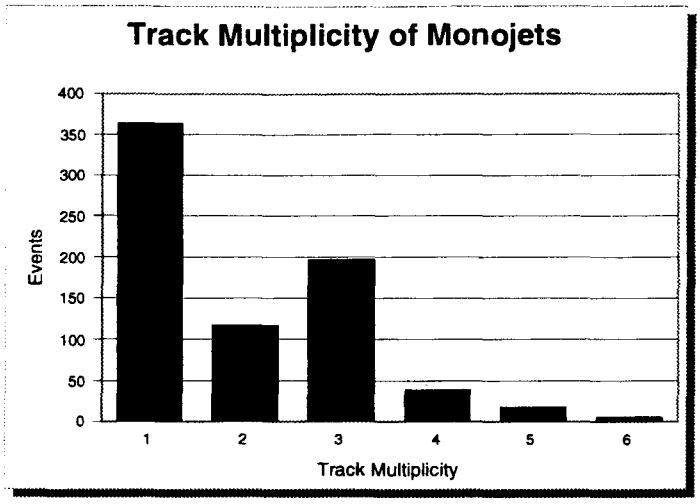

Figure 4.10: Charged track multiplicity distribution for the monojet sample.

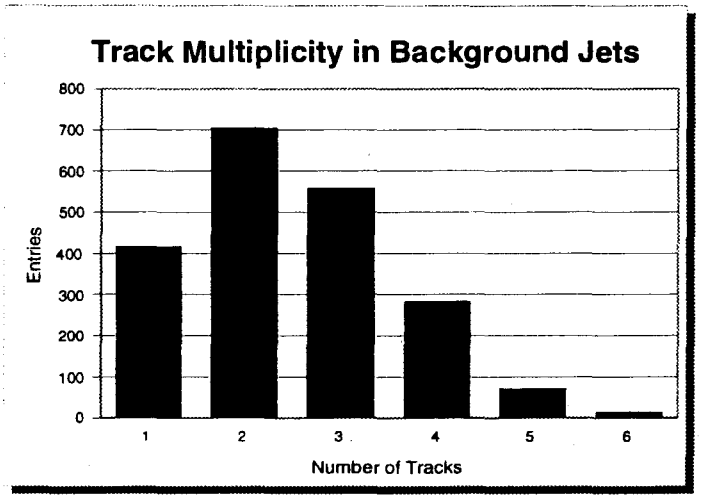

Figure 4.11: Charged track multiplicity distribution of background control sample

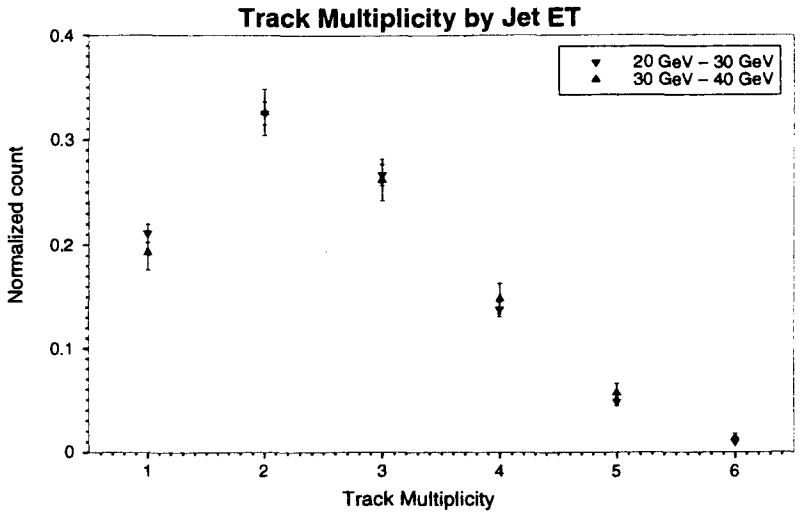

Figure 4.12: The track multiplicity distribution for the JET_20 sample in two E_T bins.

4.3.3 Fitting the Monojets

Under the assumption that the monojet sample is a combination of $W \longrightarrow \tau\ \nu_\tau$ events (modeled by the Monte Carlo) and QCD background (described by the dijet control sample), a least-squares fit to the track multiplicity distribution of the monojet sample as a linear combination of the (normalized) track multiplicity distribution for the $W \longrightarrow \tau\ \nu_\tau$ Monte Carlo and dijet control samples is done. The result of the fit is shown in figure 4.13, where the data is shown along with the fitted values for the contributions from taus and QCD background. A value of 71 $\pm$ 2(stat) $\pm$ 3(sys)% is extracted for the fractional tau content of the monojet sample.

4.4 Measuring Tau Fraction Via Impact Parameter

In this section the ability of the SVX to statistically distinguish hadronic tau jets from generic jets is demonstrated. By using the signed impact parameter, it is possible to

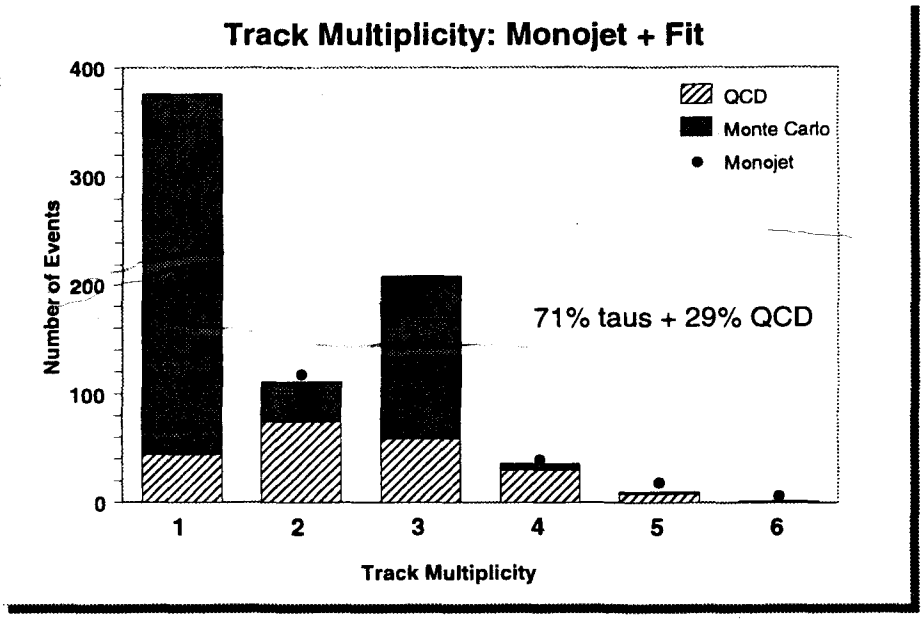

Figure 4.13: A least-squares fit of the track multiplicity distribution of the monojet sample as a combination of monte carlo taus and QCD dijet background

fit the fractional tau content of the monojet sample in a manner analogous to that done for the charged track multiplicity distribution.

4.4.1 Track Quality Cuts

The signed impact parameter distribution of the monojet sample is now considered. For any meaningful analysis of the signed impact parameter it is necessary to require that the tracks used are of suitable quality. Tracks which share hits with other tracks, have too few SVX hits, have large χ^2 , or have bad SVX hits used in the fit are considered to be of poor quality and the impact parameters from such tracks are unreliable. To insure that large impact parameters are due to secondary vertices rather than reconstruction errors, a set of track quality cuts (based on those used in b-tagging studies [32]) is employed:

- at least 3 SVX hits associated with the track
- at least 2 non-shared SVX hits
- $\chi^2 < 20$
- K_S and Λ particles removed
- $|Z_{\rm track} - Z_{\rm VXPRIM}| < 5$ cm

K_S and Λ mesons are explicitly removed because they can also cause displaced vertices which might be detected by the SVX. The restriction on the distance in z between the track's distance of closest approach and the primary vertex is to remove tracks which originate from separate events. The high instantaneous luminosity of the Tevatron leads to the possibility of multiple interactions in a single bunch crossing. Because the events are not likely to occur at the same place, the impact parameter of tracks from one vertex are likely to be displaced with respect to the other, producing erroneous impact parameters. This cut removes most such occurrences.

The low track density near the tau jets in $W \longrightarrow \tau\ \nu_\tau$ events results in few tracking errors. The Monte Carlo studies suggest that these track quality cuts retain $80 \pm 2\%$ of τ

tracks which passed the tau jet selection criteria. This compares with $78 \pm 2\%$ of similar tracks in the JET_20 sample. Though these values are consistent, the difference of 2% is taken as a systematic error.

As stated in section 4.1, a requirement of $\sigma_{VXPRIM} < 40\ \mu m$ provides confidence that large impact parameters are from displaced tracks rather than from the tails caused by poorly-reconstructed primary vertices. Varying the cut to 30 μm serves only to decrease statistics and does not significantly affect the tau fraction of the sample as determined from track multiplicity. A 2% systematic error is assigned to this criterion due to slight difference between the JET20 and monojet distributions.

4.4.2 Monojet Signed Impact Parameters

The signed impact parameter distribution of the monojet sample, after track quality cuts, is given in figure 4.14. The distribution is not symmetric about zero. The asymmetry is measured by

$$A = \frac{N_+ - N_-}{N_+ + N_-}$$

where N_+ is the number of tracks with positive signed impact parameters and N_- is the number of tracks with negative signed impact parameters. The asymmetry of 19% for the monojet sample compares with the $18 \pm 2\%$ asymmetry found in the τ Monte Carlo, and is significantly higher than the $1.2 \pm 0.5\%$ for the JET_20 sample.

It is also observed that the size of the impact parameter is not consistent with that expected from the generic jet data. The tails of the distribution extend beyond 200 μm, well outside what is seen in the jet data (figure 4.8). By itself, this is not sufficient to establish the presence of a non–zero lifetime source, as there may be unaccounted-for differences in the resolutions of the samples. When the positive-negative asymmetry is taken into account, this possibility is removed. Were the larger impact parameters merely a result of unexplained differences in resolution, there would be no preference toward positive impact parameters as seen here.

The signed impact parameter distribution is fit as the sum of the distributions from

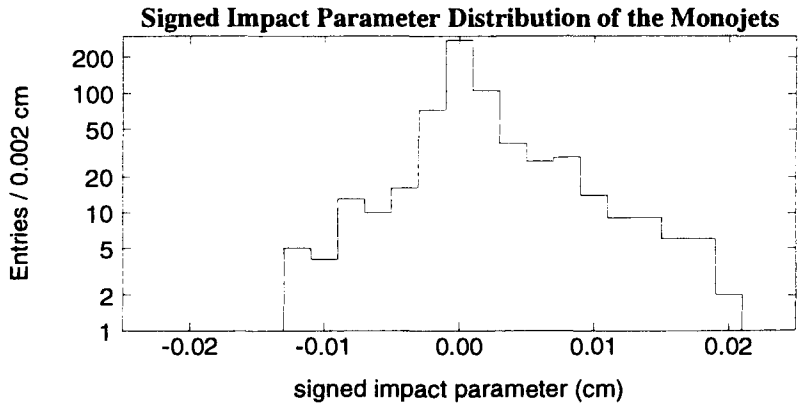

Figure 4.14: The signed impact parameter distribution of the monojet sample.

the Monte Carlo and the JET_20 control samples. The result of the log-likelihood fit is shown in figure 4.15. The fit value of $65^{+12}_{-10}\%$ τ fraction is consistent with the value of $71 \pm 4\%$ obtained from the fit of the track multiplicity distribution.

The bulk of the uncertainty in the tau fraction obtained by this method is from the fit itself. The log-likelihood indicator is well–behaved but shallow in the region of interest, resulting in a large uncertainty in the location of the minimum. Figure 4.15 demonstrates that the positive side of the distribution is better represented by the combination of the Monte Carlo and background than is the negative side. The direction of the disagreement again points to an overestimation of the sign–flipping in the Monte Carlo. This is remedied by a fit of the absolute value of the impact parameter rather the signed impact parameter.

4.4.3 Monojet Absolute Impact Parameters

The fit of the absolute impact parameter distribution for the monojet sample is given in figure 4.16. The tau fraction of the monojet sample is measured as $62^{+9}_{-10}\%$ by this method, which is again consistent with the number found via the track multiplicity technique. The smaller errors indicate the better fit achieved without the complications of sign–flipping.

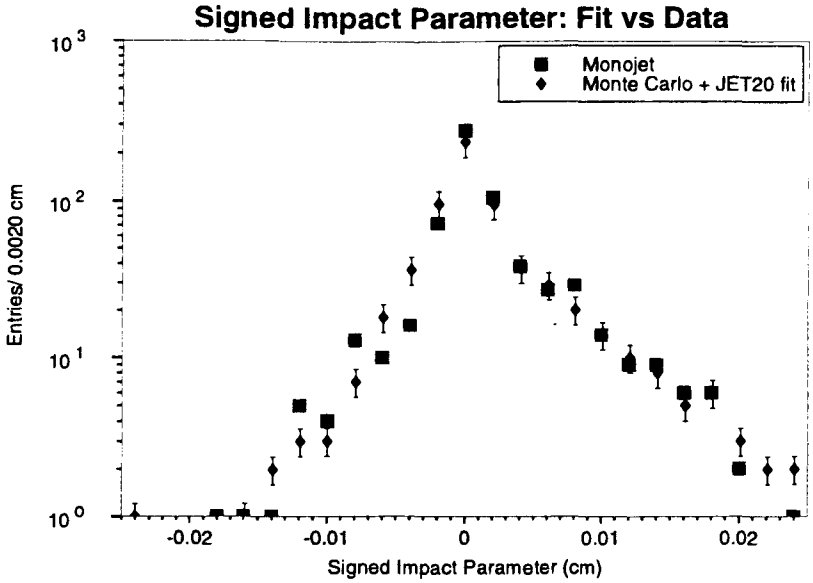

Figure 4.15: A log-likelihood fit of the signed impact parameter distribution of the monojet sample as the sum of Monte Carlo taus and generic jets. A fit of $65^{+12}_{-10}\%$ τ content is found.

The agreement of the fractional tau content derived from the impact parameter fits with that obtained from the track multiplicity distribution verifies the presence of taus in the monojet sample and the distinctiveness of the tau impact parameter distribution compared with that of generic jets.

4.5 Measuring Tau Lifetime

One feature that has been implicitly used in the fit of the impact parameter is the lifetime of the τ. The Monte Carlo was generated using the current world-average value of 295.7 ± 3.2 fs, and one must consider the influence of the lifetime on the fits. The uncertainty on the value of the lifetime is small (± 3.2 fs corresponds to a spatial difference of $\Delta c\tau = \pm 0.96$ μm) and is negligible when compared to the 200 μm scale dealt with here. The sensitivity of the impact parameter distribution to the tau lifetime is now considered.

Here there is the advantage of knowing the tau content of the sample in a manner

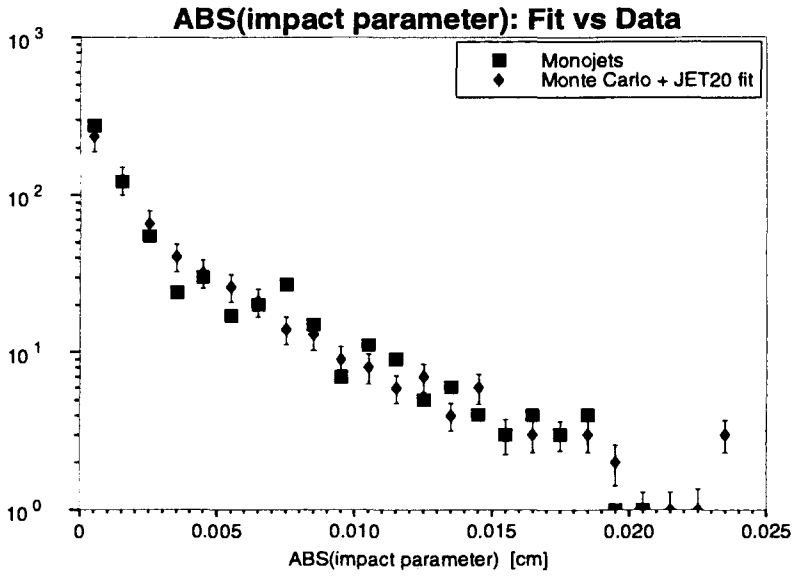

Figure 4.16: A log-likelihood fit of the absolute impact parameter distribution of the monojet sample as a combination of Monte Carlo τ's and generic jets. Shown is the superposition of the monojet distribution and the fit result of 62^{+9}_{-10}% tau content.

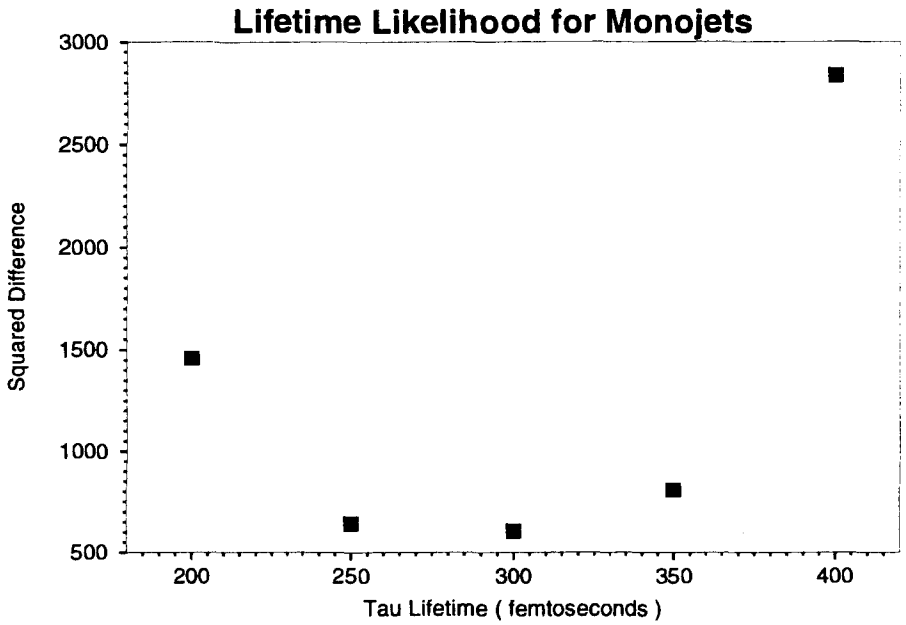

Figure 4.17: Quality of fit to the monojet sample as a function of Monte Carlo tau lifetime. The tau fraction is fixed at 71%.

derived independently of the impact parameter distribution. By fixing the tau fraction to be that obtained from the track multiplicity, the absolute impact parameter distribution is refit as a function not of the tau fraction but of the lifetime used in the Monte Carlo. Taking the summed-square difference to be a measure of fit quality, it is found that the distribution best describes a particle of lifetime $\sim$ 300 fs. A fit of figure 4.17 gives a result of $300^{+27}_{-51}(stat) \pm 17(sys)$ fs. This value is consistent with the world average, suggesting that the tracks are from tau decays.

Chapter 5

Development of a Tau Tagging Algorithm

Having demonstrated that the impact parameter distribution of hadronic jets from tau decays is distinguishable from that of generic jets, the analysis turns now to the issue of whether the impact parameter can be used to differentiate between tau jets and generic jets on an event-by-event basis. In this chapter, a technique in which the impact parameter information is used in conjunction with a calorimetry–based selection to provide such a tag is discussed.

5.1 Jet Probability

The most obvious method for selecting tau jets based on impact parameter, or even signed impact parameter, would be to make a lower–bound cut. While this would work for 1–prong taus, it is not ideal for 3–prong taus. As the number of tracks in the candidate jet increases, the likelihood that any one of them has an impact parameter greater than the chosen cut increases as well. For this reason, the SVX–based tagging algorithms typically look for correlations between the tracks. There were a variety of b-tagging techniques developed at CDF during the course of Run 1a [33],[34],[35] which worked along these lines; some looking for correlations between the impact parameter and the ϕ direction of the tracks, others attempting to explicitly reconstruct a secondary vertex from the tracks in the

suspect jet. These techniques are rejected for this analysis because they require at least 2 SVX tracks in the jet — which would result in the loss of all 1–prong tau decays.

Instead, a technique known as jet probability is considered [33]. The tagger is based on the premise that most tracks are from prompt sources and that the only causes of the non–zero impact parameters for these tracks are the tracking and resolution effects mentioned in chapter 3. By considering the signed impact parameter, most tracks from displaced vertices should appear on the positive side of such a distribution (with some small amount entering the negative side due to resolution and sign–flipping effects). This leaves the negative side as a representation of the final impact parameter resolution of the SVX, including all effects of pattern recognition, primary vertex location, multiple–scattering, etc. By dividing the signed impact parameter by its error to form the signed impact parameter significance, the positive–negative asymmetry remains, but effects caused by track momentum (which affects the uncertainty of the impact parameter, as shown in figure 3.2) are removed. Figure 5.1 shows the distribution of the impact parameter significance for a set of tracks in generic jets.

An analytic form for the resolution function is obtained from a fit of the negative side of the signed impact parameter significance distribution. From the resolution function, the cumulative distribution function is computed. The likelihood for a given track to have a measured impact parameter significance is determined from the cumulative distribution function. The probability for a given track ranges from 0 to 1, with values near 0 being very unlikely (highly displaced tracks) and values near 1 being very probable (impact parameters near zero). The probabilities for each of the tracks in a given jet are then combined into a single "jet probabilty," which provides a measure of the likelihood that a given jet is consistent with the hypothesis that it came from the primary vertex. The jet probability is computed for a jet with N tracks as:

$$\mathcal{P}_{jet} \equiv \Pi \sum_{k=0}^{N-1} \frac{(-\ln \Pi)^k}{k!}$$

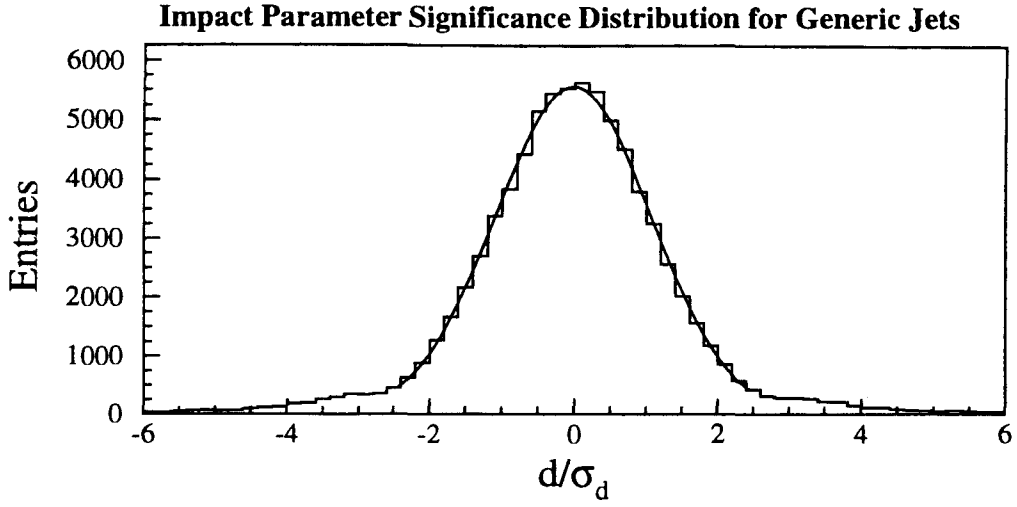

Figure 5.1: The impact parameter significance distribution of tracks in jets from a 50 GeV jet calorimeter trigger. The Gaussian fit to the region about zero has a width of 1.08 ± 0.01, compared to an ideal value of 1.

where

$$\Pi = \prod_{i=1}^{N} \mathcal{P}_{track,i}$$

Jets from secondary vertices can appear quite different when viewed in terms of jet probability. While some of the tracks in the jet may point back toward the primary vertex (the most probable value for the impact parameter is still zero, even for tracks from displaced vertices), there tend to be a larger–than–normal amount of highly displaced tracks associated with such jets. Therefore, the jet probability tends toward zero for such jets, indicating that they are unlikely to have come from the primary vertex. It is then possible to make a cut based on the jet probability to preferentially select jets from non–prompt sources.

This technique is well–suited for tau studies, as it allows the use of a single charged track. In the case of a 1–prong tau, the jet probability is equal to the track probability of the sole associated track.

5.1.1 *Selection of the Resolution Functions*

To assure that the resolution functions used in the jet probability tagger are representative, the SVX tracks were chosen from a large set of jets from calorimetry–based trigger streams. This generic jet data provides coverage of a wide range of energy and momentum spectra, as well as having a relatively small ($\sim$ 2%) heavy flavor component. The SVX tracks were then catagorized by the number of SVX hits associated with the track and by the number of SVX hits uniquely assigned to the track. Because the SVX tracks only in $r-\phi$, and because of the high concentration of tracks in some jets, it is not uncommon for a single SVX hit to be linked to more than one track during track reconstruction. Such shared hits are part of the pattern recognition difficulties associated with tracking algorithms, and have a detrimental effect on impact parameter resolution. As a base level of track quality, each track is required to have a least two non–shared hits. Combined with the requirement of at least two hits per track, this results in a total of six resolution functions.

To describe the shape of the impact parameter significance distribution, and in particular the tails of the distribution, the resolution function fit to the data is a combination of two Gaussian curves and an exponential. The first Gaussian describes the central core of the distribution, as seen in figure 5.1. The second Gaussian and the exponential curve are used to match the tails of the negative side of the signed impact parameter distribution to account for deviations from the central Gaussian. Though these deviations occur for only a few percent of the total number of tracks, it is precisely those atypical portions of the tracking which may account for erroneous tags.

This method of computing the resolution function will slightly overestimate the true width of the prompt–source distribution, as there are some entries from displaced tracks in the negative region of the signed impact parameter significance distribution. This will result in a small overestimate of the background levels, but this conservative estimate is not considered to be a problem.

The values computed for the resolution functions are listed in table 5.1.

Number of SVX Hits	Shared Hits	$Mean_1$	$Width_1$	$Mean_2$	$Width_2$	Exponential Slope
4	0	0.00388	0.92667	0.03522	2.15120	6.64640
	1	-0.00052	0.95680	0.14529	2.25450	8.09810
	2	-0.00348	1.00690	0.06353	2.16610	9.22420
3	0	0.00369	0.99610	-0.01936	2.16410	8.81490
	1	-0.01903	1.01910	0.14951	2.46840	14.13600
2	0	-0.00952	1.34640	0.01365	2.74570	11.59800

Table 5.1: The resolution functions used in the jet probability tagger. The values are listed for the 2 Gaussians and the exponential, in order of decreasing contribution. In all cases, the first Gaussian accounts for more than 90 % of the total resolution function.

5.1.2 Jet Probability Distributions

The resolution functions derived for the SVX give only the track probabilities; there remains the question of how to form the jet probabilities. Three choices present themselves for consideration in studying the jet probability:

- Use only those tracks with negative signed impact parameters.
- Use only those tracks with positive signed impact parameters.
- Use all tracks, regardless of sign.

Each of these is considered in turn. The jet probability formed from only those tracks with negative signed impact parameter should not be of particular use in identifying displaced vertices given the choice of the sign convention. It is, however, a useful check of the resolution functions to observe this distribution. Since the resolution functions were derived from the negative side of a signed impact parameter significance distribution, a distribution made from only the those tracks from the negative side should be flat. This is indeed the case, as shown in figure 5.2 for a sample of JET_20 data. This is reassuring given that the JET_20 data were not used in the construction of the resolution function (higher energy triggers, such as JET_50 and JET_70 were used).

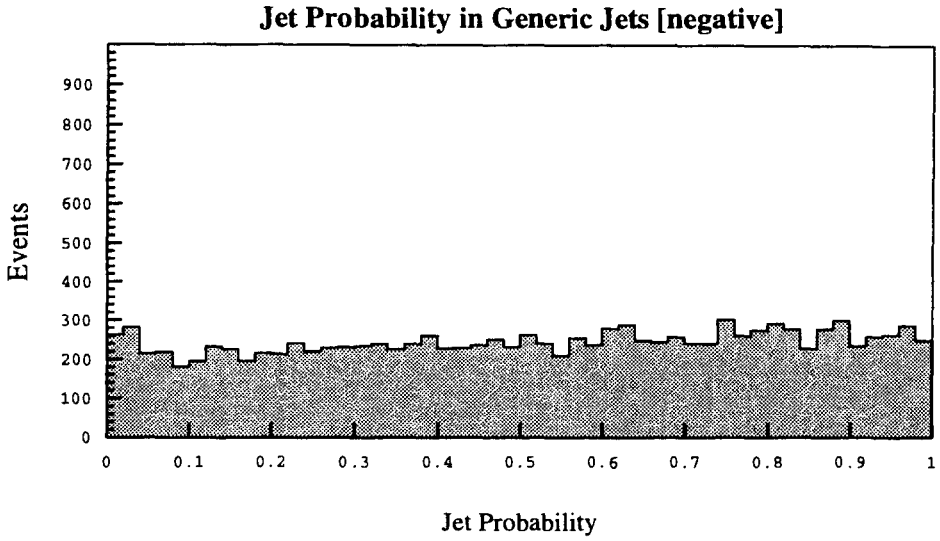

Figure 5.2: The jet probability distribution for JET_20 data, using only those tracks with negative signed impact parameters.

Of more interest is the jet probability constructed only from those tracks with positive signed impact parameters. By design, these should contain most of the tracks which come from displace vertices and should be the best choice for tagging. When the jet probability for the same JET_20 sample is plotted, this time using only those tracks with positive signed impact parameters, a markedly different distribution is observed (figure 5.3).

Most of the distribution is flat, corresponding to those jets which originated near the primary vertex. However, there is a noticeable spike at low values of jet probability. This corresponds to displaced vertices in the sample, primarily from heavy flavor. To tag the heavy flavor, one need merely make an upper–bound cut on the jet probability. This technique has been used with considerable success in the identification of bottom quarks at CDF.

There is a concern about such a cut when searching for taus, namely that of sign–flipping. For heavy flavor, there are typically many tracks in the jet, and the likelihood that

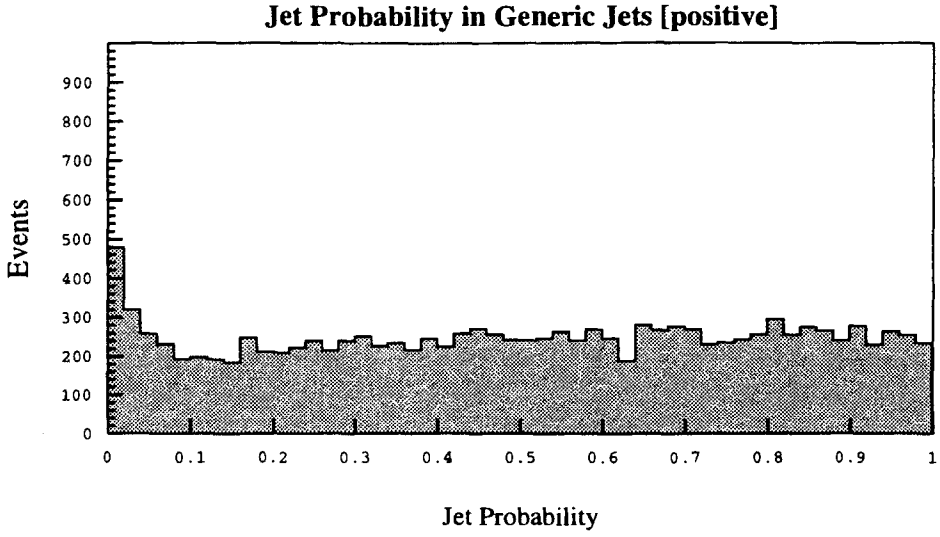

Figure 5.3: The jet probability distribution for JET_20 data, using only those tracks with positive signed impact parameters.

all of them are sign–flipped into the negative region is small. This is not the case for taus, because most of the hadronic tau jets contain a single track. To require that it be positive would result in the loss of a considerable fraction of the 1–prong taus. This is remedied by using all of the tracks in the jet to form the jet probability, without regard to the sign. This is a valid construction, because the resolution function for prompt tracks is, presumably, symmetric about zero. The disadvantage is that the background is double that of using the positive-only tagger. This is analogous to the fit of the tau fraction using the absolute impact parameter in section 4.4.3. The peak at low jet probability using all tracks is shown for the JET_20 data in figure 5.4.

5.2 Eta-Width

As is shown in chapter 6, the use of the jet probability cut is not necessarily sufficient to achieve the tau purity desired. An additional requirement based on the narrowness of the

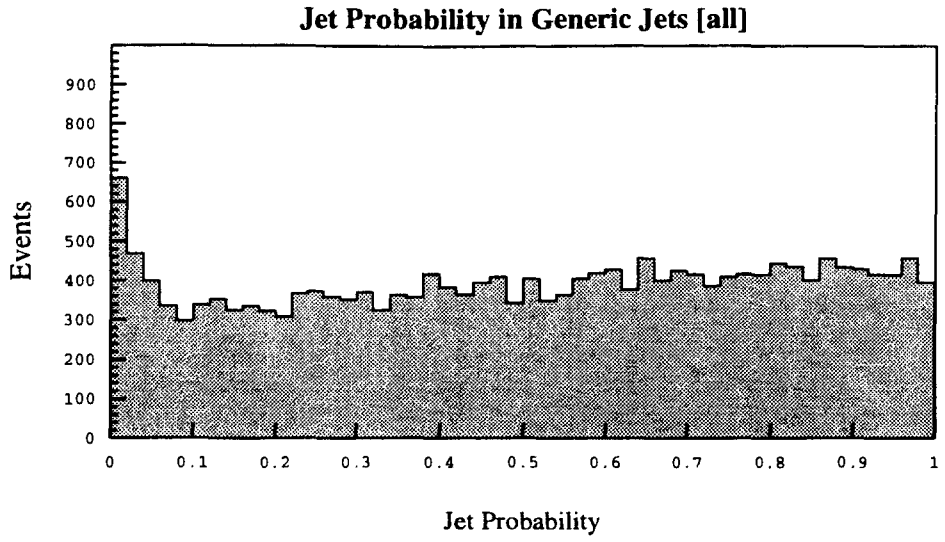

Figure 5.4: The jet probability distribution for JET_20 data, using all tracks.

tau jets is now introduced [36]. The width of the jet in η is defined as the energy–weighted second η–moment of the jet cluster (clustered with a cone of $\Delta R = 0.4$),

$$\langle \eta \rangle \equiv \frac{\sum_i E_i \eta_i^2}{\sum_i E_i} - \left(\frac{\sum_i E_i \eta_i}{\sum_i E_i} \right)^2$$

where E_i are the energies in each η section (summed over the ϕ towers) and η_i are the locations of the center of each tower. This shape parameter is computed during the jet clustering.

By using the η-width, a measure of calorimetric isolation is obtained which is analogous to and correlated with the tracking isolation described in chapter 4. For generic jets, the η-width distribution is quite wide. However, this analysis is concerned only with jets which have already passed the tracking isolation cut and tend to be somewhat narrower. The η-width distribution for the JET_20 control sample is shown in figure 5.5.

This compares with the much narrower distribution for taus predicted by the Monte Carlo, shown in figure 5.6. Even with the correlations brought about by the tracking

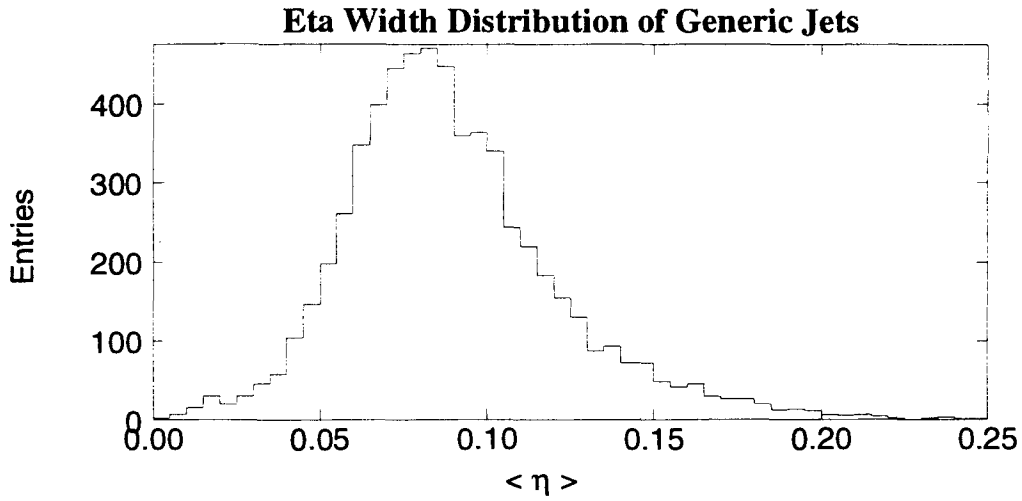

Figure 5.5: The η-width distribution of JET_20 lead jets which pass kinematic selections, including tracking isolation.

isolation requirement, the tau jets remain considerably more collimated than the generic jets in the JET_20 control sample. This permits the selection of an upper-bound cut on the η-width of the jets to enhance the tau purity of a given sample. Studies in which the η-width alone is used to tag tau jets [36] found that requiring $\langle\eta\rangle < 0.06$ provides considerable background rejection with a minimal loss of efficiency for retaining taus. This cut is duplicated in this analysis.

The correlation between the η-width and the track multiplicity is discussed below.

5.3 Combined Jet Probability – Eta Width

Here the jet probability alogrithm and the η-width cut are combined with the kinematic and tracking isolation requirements already made to select hadronic tau jets. This section details the investigation of the effects of combining these cuts, both in terms of background rejection and tau selection.

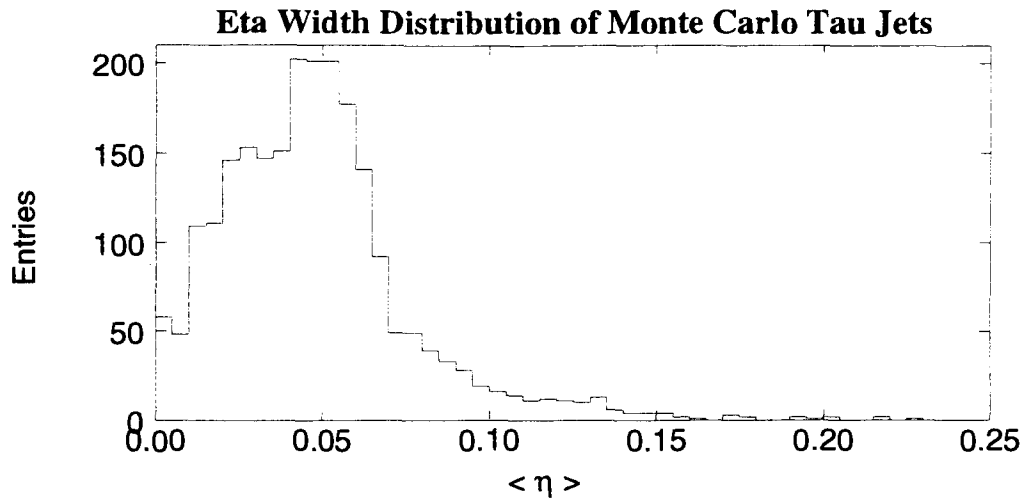

Figure 5.6: The η-width distribution of tau jets in Monte Carlo $W \longrightarrow \tau\ \nu_\tau$ events, after kinematic selections including tracking isolation.

5.3.1 Results of Tagging on Monte Carlo τ's

The effects of a tagging selection on the track multiplicity distribution are determined from the $W \longrightarrow \tau\ \nu_\tau$ Monte Carlo. In chapter 6, the efficiency of the cuts on the monojet sample is determined from the data.

The jet probability algorithm, by its very design, is more efficient for jets with greater track multiplicity. Not only is there greater statistical significance in the presence of more displaced tracks, but there is less likelihood that the jet will be rejected because none of the tracks pass the quality requirements. For tau studies, the latter is not of great concern because the jets tend to be of low enough track multiplicity that there is little confusion during the pattern recognition. But since the majority of hadronic tau decays produce a single charged track, the effect of placing tight cuts on the jet probability is a markedly different track multiplicity distribution.

The jet probability distribution for Monte Carlo taus is shown in figure 5.7. The displaced vertex of the tau is responsible for the large spike at low jet probabilities. The flat area extending toward a jet probability of 1 correspond to those jets for which either

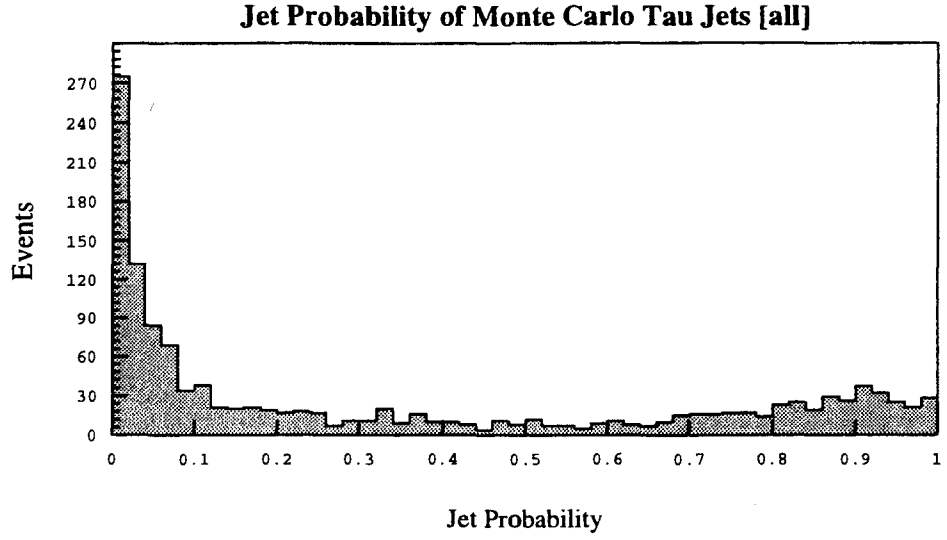

Figure 5.7: The jet probability distribution (all charged tracks) for Monte Carlo taus.

the tau did not travel far before decaying or the decay products along the line of flight of the tau. It is noted that the fraction of taggable taus (those taus with at least one good SVX track) in the leftmost bin is much smaller than the corresponding fraction for jets from bottom quarks; an effect due to the shorter lifetime of the tau and the lower track multiplicity of tau jets.

Figure 5.8 shows the expected efficiency for the tau tagger based on the Monte Carlo. This includes the effects of the different efficiencies for the 1–prong and 3–prong taus. The efficiency can also be computed by track multiplicity, as shown in figure 5.9. Note that the efficiency for the 3–prong tau jets is systematically higher than the efficiency curve for the 1–prong tau jets. The effects of the changing efficiency are visible in the changing track multiplicity distribution as tighter cuts are imposed, and are shown in figure 5.10. The change in the ratio of 1–prong to 3–prong taus as tighter jet probability cuts are imposed is important, because it is by the track multiplicity that the number of taus present in the sample is determined. Therefore, in order to get accurate values for the number of taus

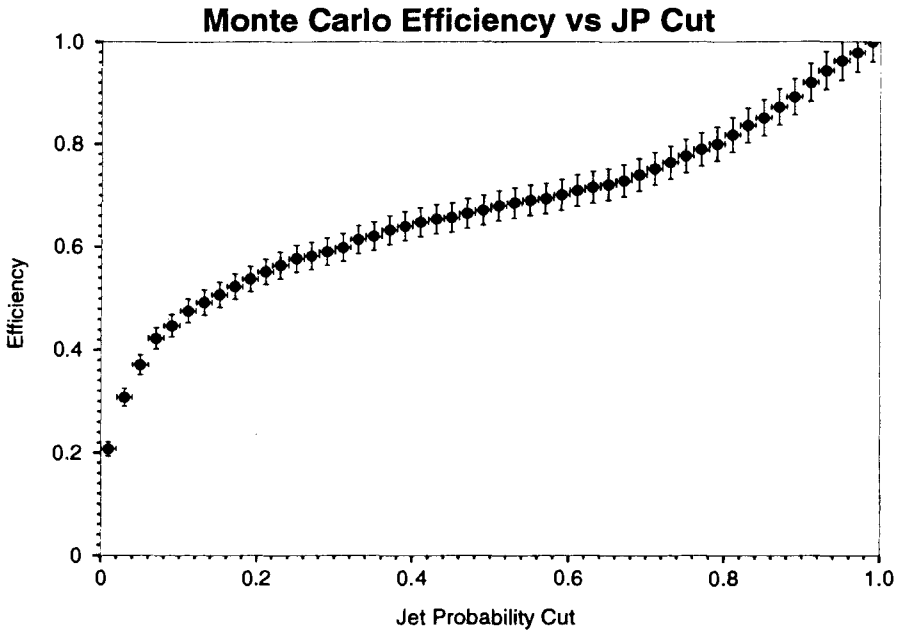

Figure 5.8: The fraction of taggable Monte Carlo τ jets remaining as a function of the jet probability cut used. The jet probability is constructed using all good tracks, regardless of the sign of the impact parameter.

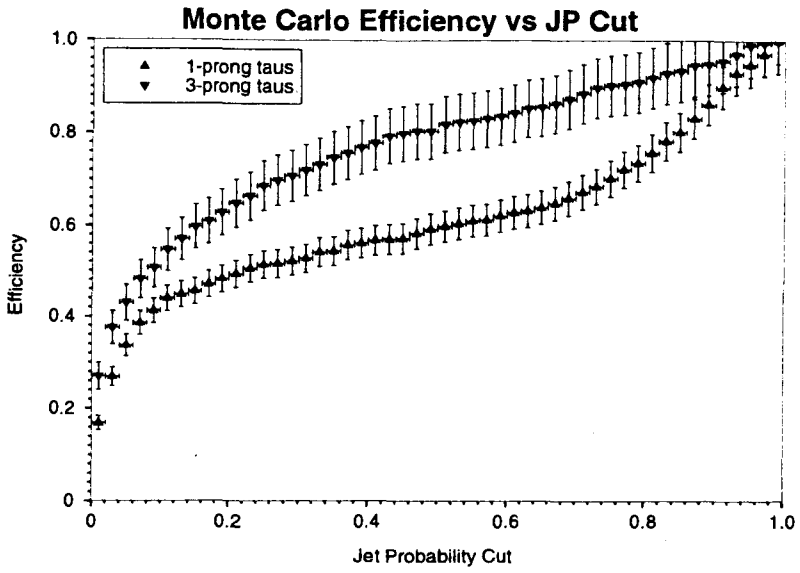

Figure 5.9: The fraction of taggable Monte Carlo τ jets remaining as a function of the jet probability cut used and plotted separately by track multiplicity. The corresponding curve for 2–prong τ jets falls between the curves shown here, but is not included for clarity.

present in a sample after making the cuts, it is important to know the effects of the cuts on the track multiplicity distributions of both the taus and the background. The background is discussed in the next section.

For the $W \longrightarrow \tau + \nu_\tau +$ jets analysis, an upper–bound cut of $\mathcal{P}_{jet} < 0.2$ is chosen. Examination of figure 5.8 shows this to be in the "shoulder" region of the efficiency curve. The validation of this selection is seen in chapter 6.

The effect of the η-width cut is not as pronounced because the choosen cut of $\langle\eta\rangle < 0.06$ is fairly loose for tau jets. The track multiplicity distribution of the Monte Carlo is not noticeably effected by the η-width criterion. The normalized track multiplicity distributions, before and after application of the η-width cut, are shown in figure 5.11.

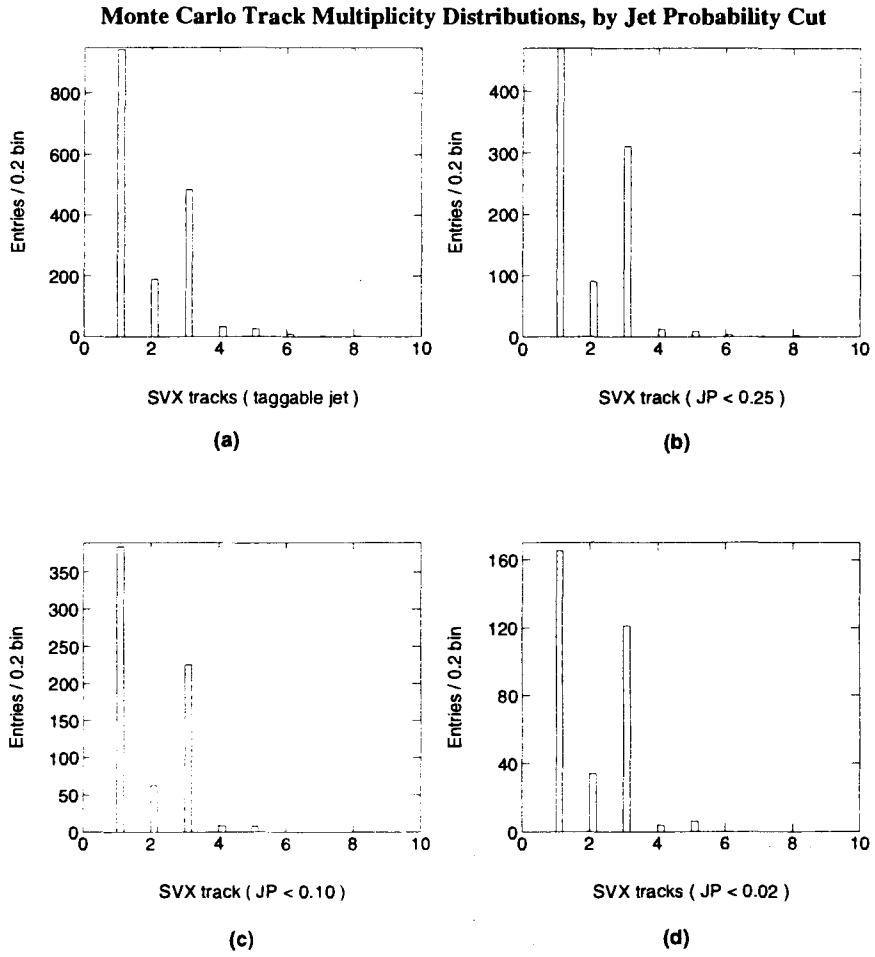

Figure 5.10: The SVX track multiplicity of taus in the Monte Carlo $W \longrightarrow \tau\ \nu_\tau$ sample as a function of jet probability cut. Figure (a) shows the nominal distribution for taggable jets. Figures (b), (c), and (d) show the distributions for jet probability cuts of 0.25, 0.10, and 0.02, respectively.

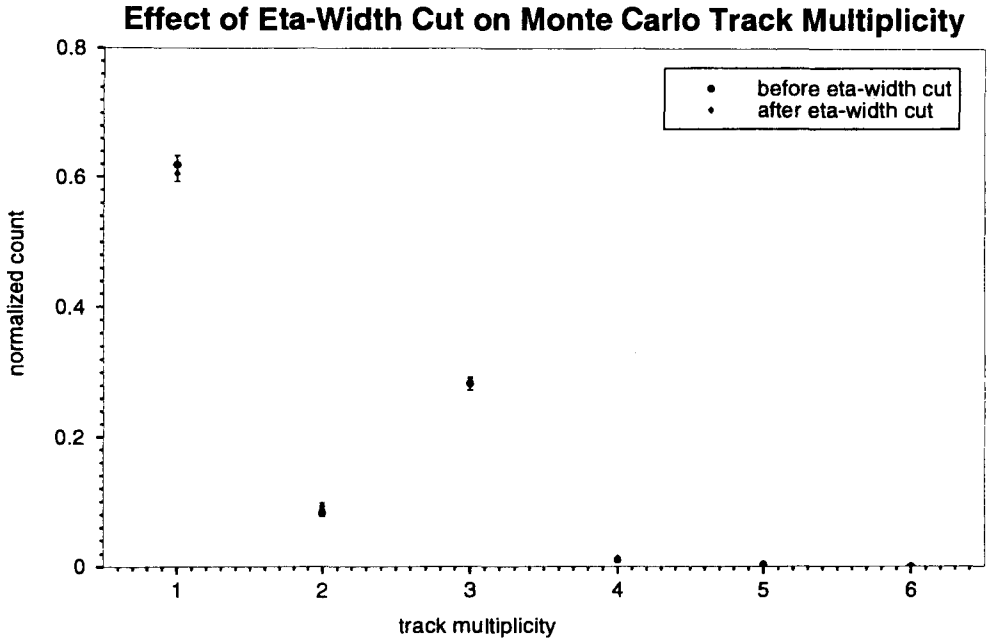

Figure 5.11: The effect of adding an η-width cut on the track multiplcity distribution of Monte Carlo tau jets. The values are consistent, indicating that there is no bias added to the distribution by the cut. Tracking isolation, and other kinematic cuts, were previously applied.

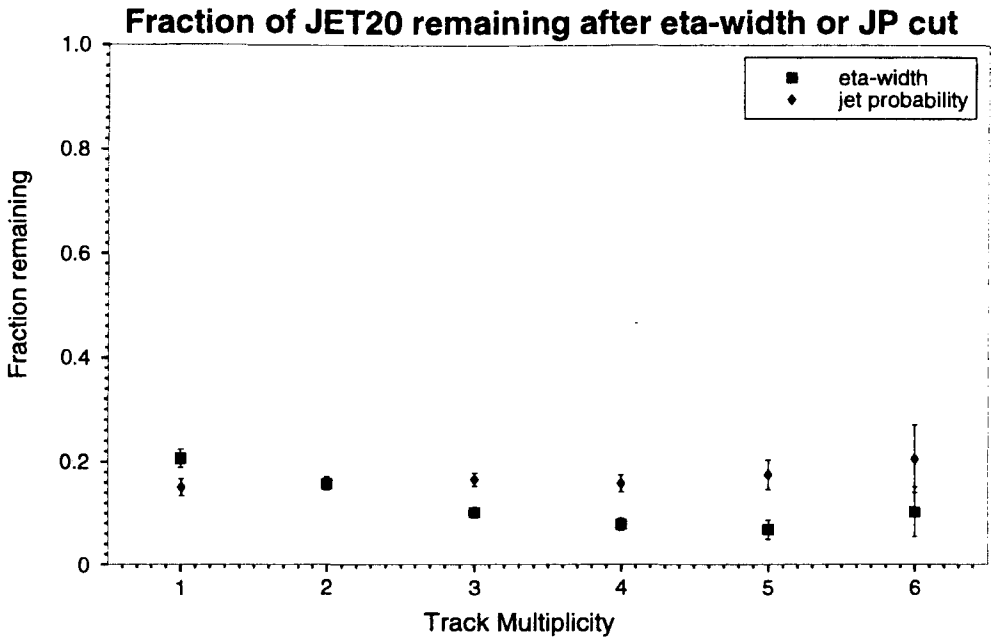

Figure 5.12: The relative fraction of jets remaining in a JET_20 sample after application of a jet probability or an η-width cut, as a function of track multiplicity.

5.3.2 Results of Tagging on Generic Jets

Both the jet probability and the η-width cut affect the track multiplicity distribution of the JET_20 sample. The jet probability tag demonstrates a slight preference toward higher-multiplicity jets. The dependence on the η-width cut is more pronounced, with a greater preference for low-multiplicity jets. These effects are demonstrated in figure 5.12 for a jet probability cut of 0.2 and an η-width cut of 0.06, .

That the effect of the η-width cut is much more pronounced in the JET_20 sample than in the Monte Carlo taus is not surprising. The cut was fairly loose for the Monte Carlo, with most jets passing, but is tight on the background (see figure 5.5). That the imposition of a cut which prefers narrow jets should greatly prefer jets with fewer tracks reflects the correlation between the collimation of a jet as viewed in tracking with the collimation as viewed by the calorimeter.

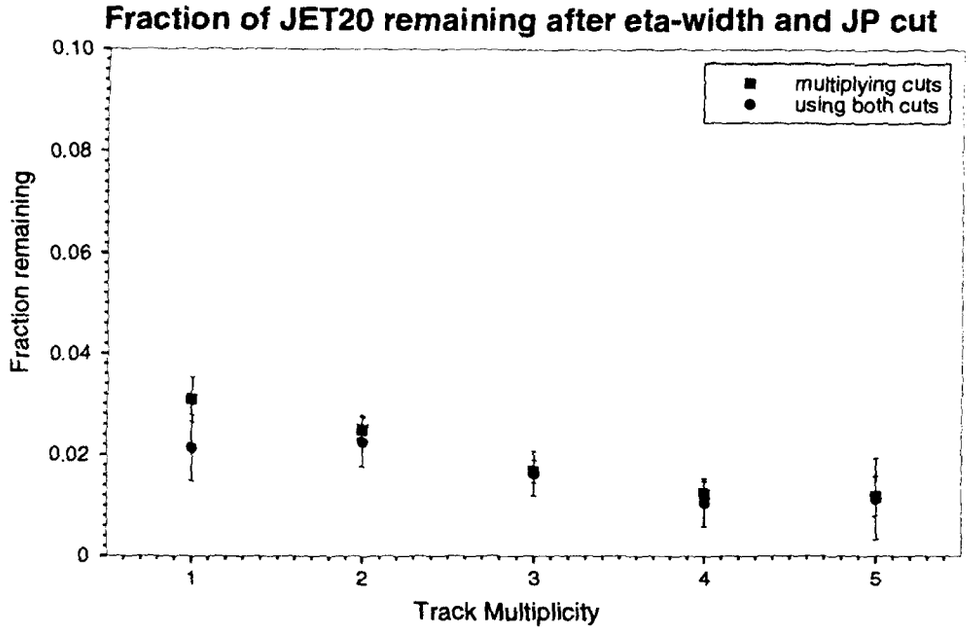

Figure 5.13: The relative fraction of jets remaining in a JET_20 sample after application of a jet probability and an η-width cut, as a function of track multiplicity. Also shown are the predicted results from multiplying the individual rejection factors.

It is worth mentioning at this point that one of the primary reasons for the use of the jet probability and the η-width cuts is that they are likely to be independent. There is no reason to suspect *a priori* that narrow jets in the calorimeter are predominantly from displaced vertices. This assumption is checked in the JET_20 data using the results shown in figure 5.12. If the cuts are truly uncorrelated, the results of applying them simultaneously should be the same as multiplying the fractional results of figure 5.12. This is done, using the same cuts, in figure 5.13.

The computed values for the rejection of background based on the individual plots of figure 5.12 are the consistent with those computed from using both cuts on the data. The statistical error bars are large, representing the unavoidable side-effect of having made a selection which significantly suppresses the background. Of the ~85,000 jet events initially studied, with 2993 passing the kinematic criteria, only 53 survive both the jet probability

and the η-width cuts. The results obtained from multiplying the rejection factors is slightly higher, and these are used for a conservative (overestimate) of the background.

The crossing of the rejection factor curves shown in figure 5.12 is a matter of some concern. If the combination of the cuts were to result in preferences toward 1–prong and 3–prong jets in the background, distinguishing between tau jets and background would be much more difficult. Fortunately, this is not the case. The track multiplicity distribution of the background after the cuts (figure 5.14) is still quite distinct from that of the tau jets.

5.4 Application to the Monojets

The monojet sample is now considered in the terms of the SVX–based jet probability. The jet probability derived from the positive signed impact parameter tracks is shown in figure 5.15. A large spike at low jet probability corresponding to the secondary vertices is observed. It is seen that in a sample of 71% taus, only about 10% of the events are in the leftmost bin. This is because the most likely value for the impact parameter, even for tracks from secondary decays, is zero (see chapter 3).

The distribution of the jet probability based on only tracks with negative signed impact parameters is given in figure 5.16. It is flat, as expected for a distribution which should be dominanted by background (from the definition of the signed impact parameter).

The effect on the track multiplicity distribution of the monojet sample with increasingly stringent requirements in the jet probability is demonstrated in figure 5.17. The expected change in the balance of 1–prong to 3–prong taus is observed at very low values of jet probability. The fractional tau content of the sample after such cuts also increases, as determined by track multiplicity. Use of the tau fraction obtained from the track multiplicity for varying jet probabilities allows the calculation of the tau efficiency as a function of the jet probability tag first from the data and then comparison to the Monte Carlo. This is done is chapter 6.

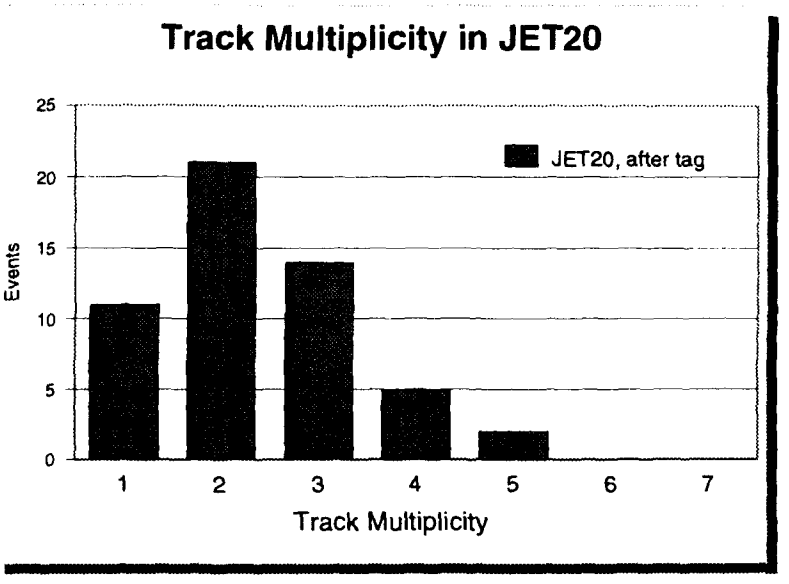

(a)

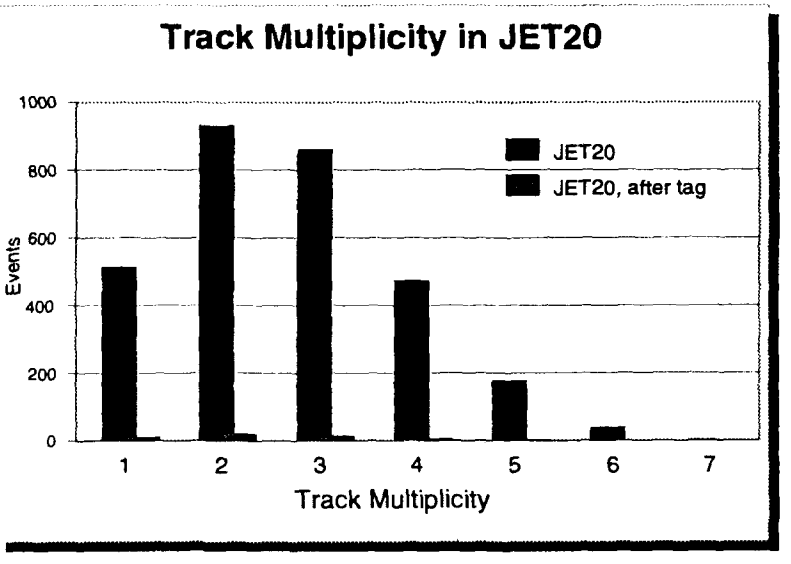

(b)

Figure 5.14: The track multiplicity distribution of the JET_20 data after application of both the jet probability and η-width cuts. Figure (a) shows the track multiplicity for only those events which pass both cuts, while figure (b) shows those events alongside the JET_20 data before the cuts.

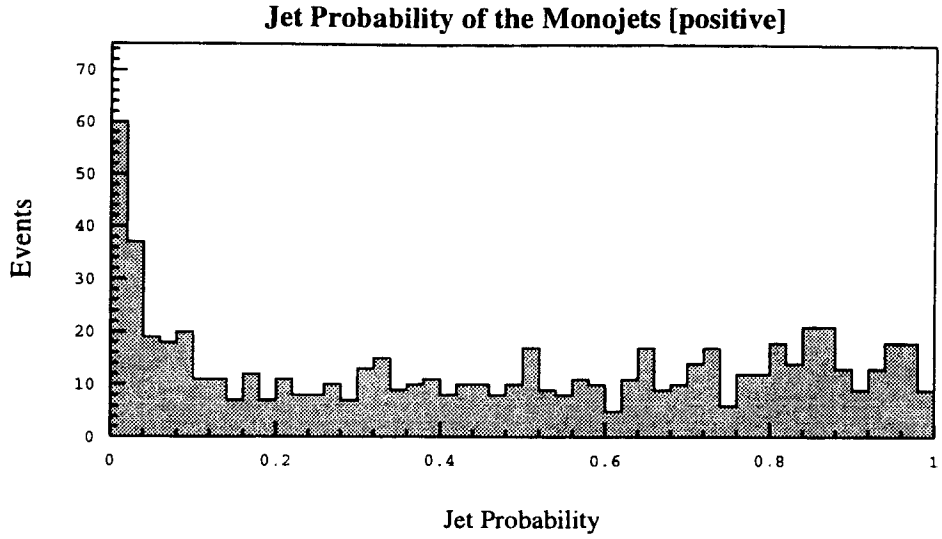

Figure 5.15: The jet probability (positive tracks) for the monojet sample.

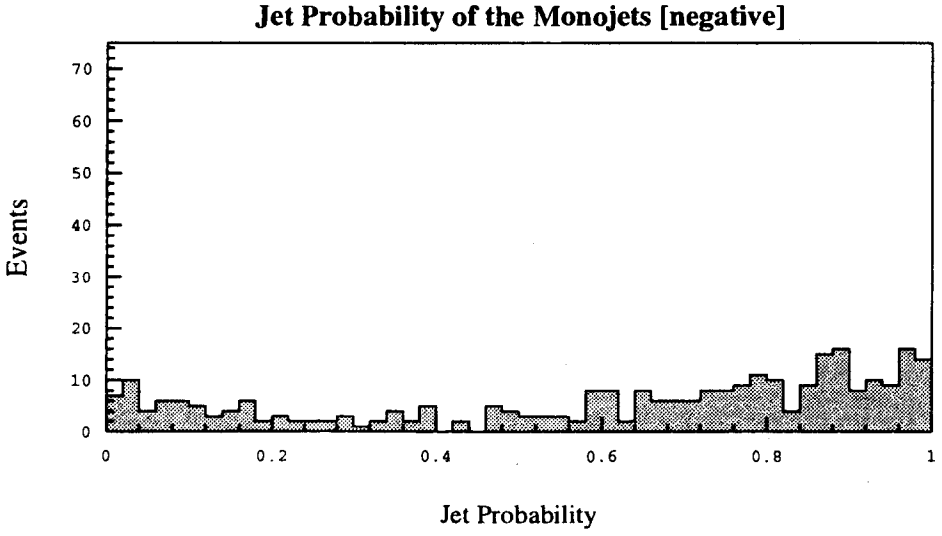

Figure 5.16: The jet probability (negative tracks) for the monojet sample.

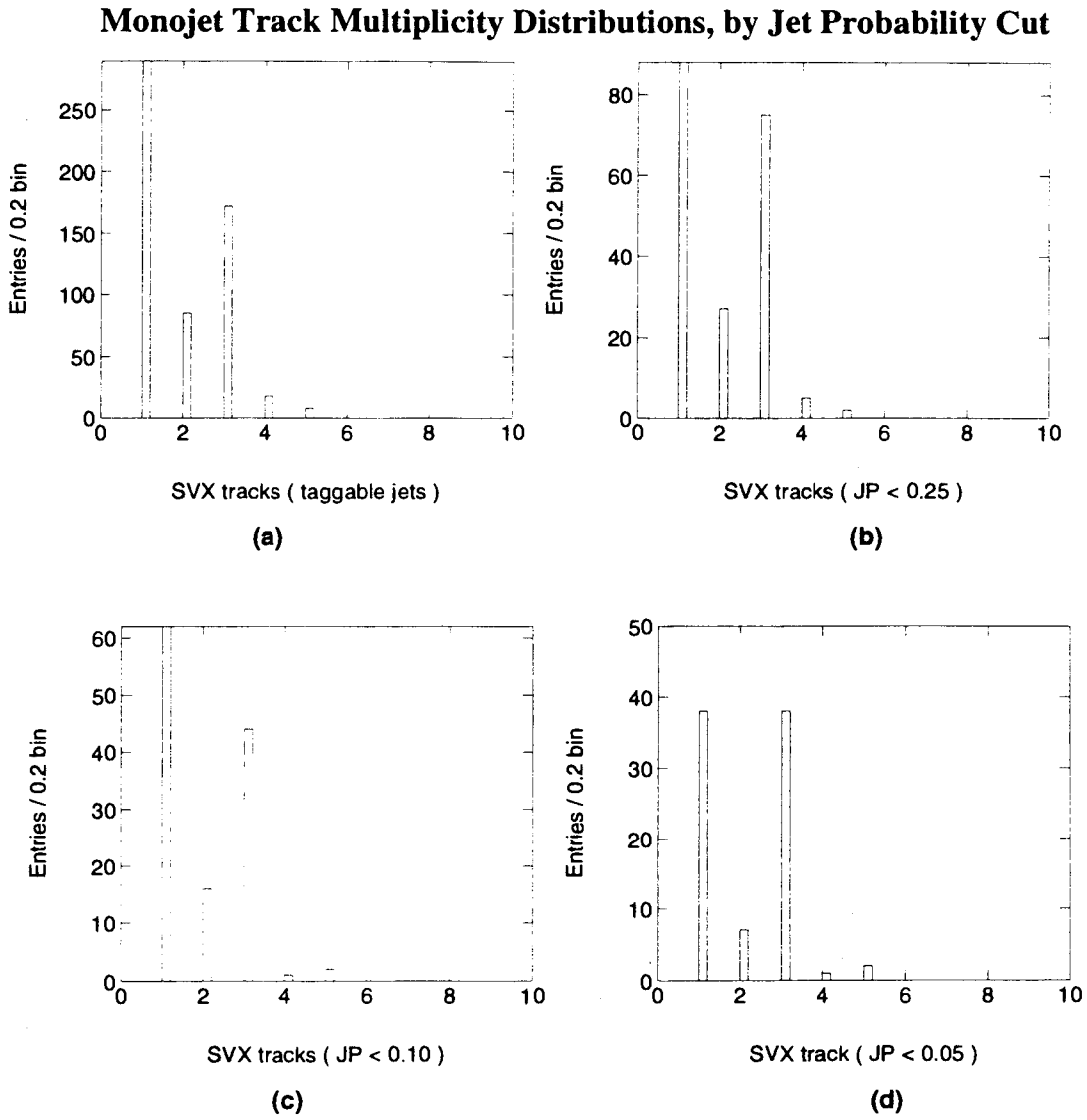

Figure 5.17: The changing track multiplicity distribution of the monojet sample for increasingly tight cuts on the jet probability. Figure (a) shows the track multiplicity for all jets with at least one good track, while figures (b), (c) and (d) show the distributions for jet probability cuts of 0.25, 0.1, and 0.05, respectively.

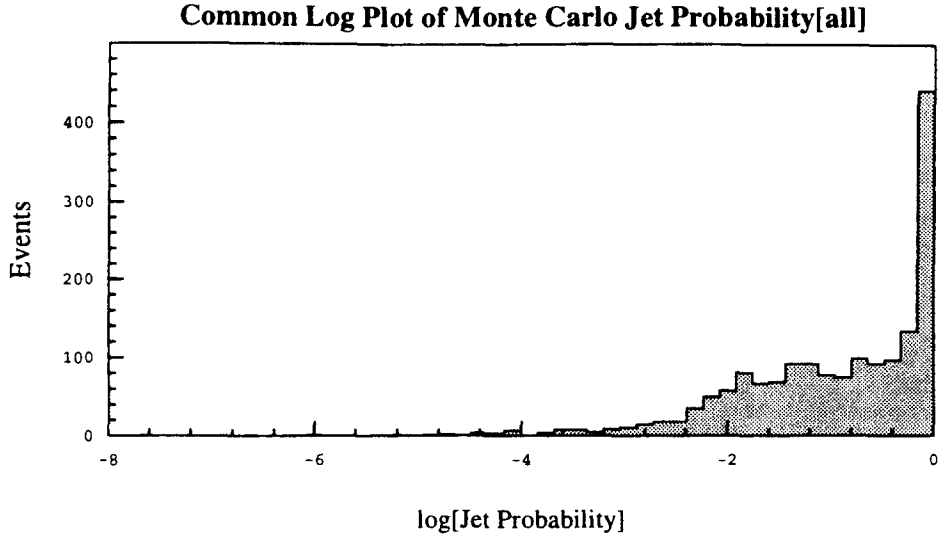

Figure 5.18: The common logarithm of the jet probability of hadronic tau jets in Monte Carlo.

5.5 A Window Cut on the Jet Probability

Placing an upper-bound cut on the jet probability is sufficient to purify the monojet sample. For a sample with a lower signal-to-noise, additional restrictions are requried to suppress heavy flavor in the data. While the mass cut and tracking isolation remove most such events, a jet probability tagger will preferentially select those jets from heavy quark production. One solution is the addition of an η-width cut, which rejects heavy flavor at the same rate as other QCD jets. Another beneficial modification is the choice of a windowing cut on the jet probability.

Figure 5.18 shows a plot of the logarithm of the jet probability for Monte Carlo τ jets. In this manner, the region of low probability is graphically enhanced. The large spike near zero on this plot corresponds to the extended flat region in the linear plot of figure 5.7, while the remainder of the distribution displays the spike at low jet probability seen earlier.

It is seen in figure 5.18 that few of the tau jets have a jet probability below 10^{-3}.

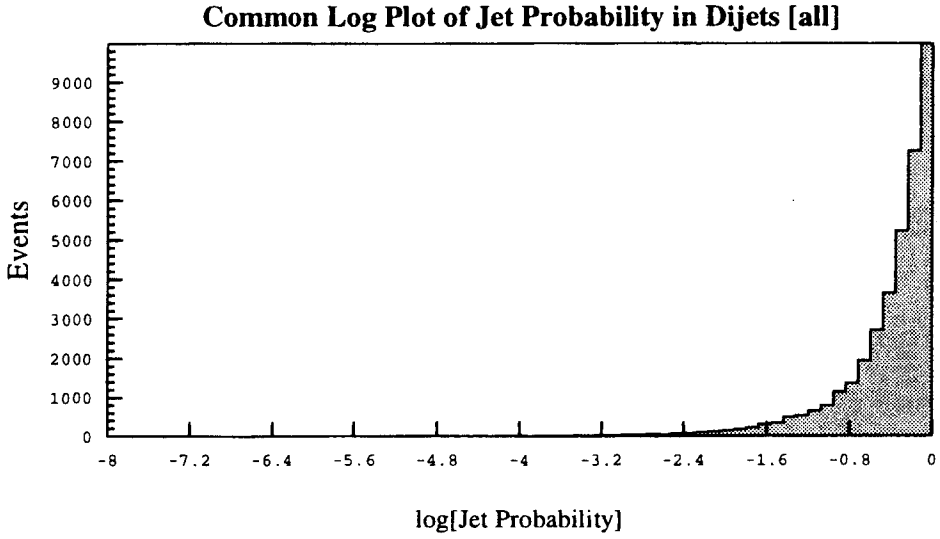

Figure 5.19: The common logarithm of the jet probability of the JET_20 control sample.

While this is also true of the generic jet sample (see figure 5.19), it is not the case for heavy flavor. Since jets below this value are unlikely to be taus, there is little reason to include them in the sample. A lower-bound on the jet probability at 0.005 is introduced to further reduce the background. This has a small affect on the track multiplicity distributions of the Monte Carlo and the generic jets which is taken into account in later chapters during fitting.

Chapter 6

Hadronic Tau Decays in W + jets Events

The tau–tagging algorithm developed in chapter 5 is used to select a data sample in which real W bosons are accompanied by radiated jets and the W subsequently decays to a tau. This event topology is suitably challenging because the background of generic QCD processes is large compared to the expected signal. The production of W + jets has so far been observed only in the electron and muon decay modes of the W.

6.1 Event Selection

The event selection for the W + jets data sample is similar to that for the monojet sample listed in chapter 4, but differs in a few key areas. For this sample, the cuts on the number of jets in the event and the cut on the $\sum E_T$ of the events are removed. Because the cross-sections of the various topologies are measured, the choice of trigger is restricted to avoid the complications of computing the efficiencies for overlapping trigger requirements.

6.1.1 Trigger Requirements

Requirements are placed on the Level 2 and Level 3 triggers used to select the events. The primary Level 2 tau trigger at CDF during Run 1a was the TAU_20_MET_20 trigger, which required 20 GeV $\not\!\!E_T$ as well as at least one jet which satisfied the following criteria:

- the jet is in the central calorimeter

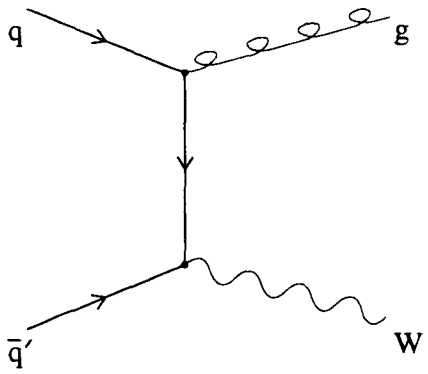

Figure 6.1: Production of a W boson with associated jets at CDF.

- no more than three trigger towers are associated with the jet
- at least one CFT track of $P_T > 4.8$ GeV/c within 30° of the jet
- at least 20 GeV energy in the calorimeter
- non-zero amount of energy deposition in the electromagnetic portion of the calorimeter

After these Level 2 trigger requirements, additional constraints are made by the Level 3 trigger before the event is passed on the chosen TAU_10_MET_20 trigger. While the more sophisticated jet clustering at Level 3 has some affect on the identification of taus, the dominant effect is the imposition of a dijet rejection cut. Because most of the background to taus is QCD dijet events, in which the jets tend to be back-to-back, a cut is sometimes made on the azimuthal angle between the lead jet and other jets to remove these events. The choice of whether this dijet rejection is applied depends on the amount of $\not\!\!E_T$ in the event, as summarized in table 6.1.

Beyond $\not\!\!E_T$= 40 GeV, there is no dijet removal applied at the Level 3 trigger under the assumption that such events are more likely to have "real" sources for the missing energy.

$\not\!\!E_T$	E_T cut for other jet	$\Delta\phi$ cut
< 20 GeV	(not in trigger)	(not in trigger)
20 - 40 GeV	MAX(10 GeV,$0.5 \times \not\!\!E_T$)	$< 165°$
> 40 GeV	(no cut)	(no cut)

Table 6.1: The dependence of the Level 3 dijet rejection on the amount of missing energy in the event. The dijet rejection is applied to τ triggers, and not to all events.

Events satisfying these requirements are split off into the Exotics stream during the offline reprocessing of the data, eliminating the need to search the entire CDF data set. As the triggering information is stored with each event record, the selection of the events based on which trigger fired is straight-forward.

6.1.2 Other Cuts

As with the monojet sample, constraints beyond those of the trigger are made on the data sample. For the selection of $W \longrightarrow \tau + \nu_\tau + n$ jets, it is required that:

- 25 GeV $\leq \not\!\!E_T \leq$ 40 GeV
- $\Delta\phi(\not\!\!E_T, \text{jets}) > 0.5$
- $\sigma_{\text{VXPRIM}} \leq 40\ \mu m$

The windowing cut on the $\not\!\!E_T$ is placed based on Monte Carlo studies. Because the W bosons produced are real, it is unlikely that the neutrino from the W decay is produced with $P_T > 40$ GeV. Most events with more than 40 GeV $\not\!\!E_T$ are found to be background, and are removed at the expense of some small signal loss.

The imposition of additional multijet rejection is guided by the consideration of the case of mismeasured jets in the calorimeter. If the source of $\not\!\!E_T$ in the background is due to a jet reconstructed with substantially less energy than should be, the direction of the $\not\!\!E_T$ vector will be near that mismeasured jet. When the azimuthal angle between the $\not\!\!E_T$ and the various reconstructed jets in the event is plotted, it can be seen that there is indeed a

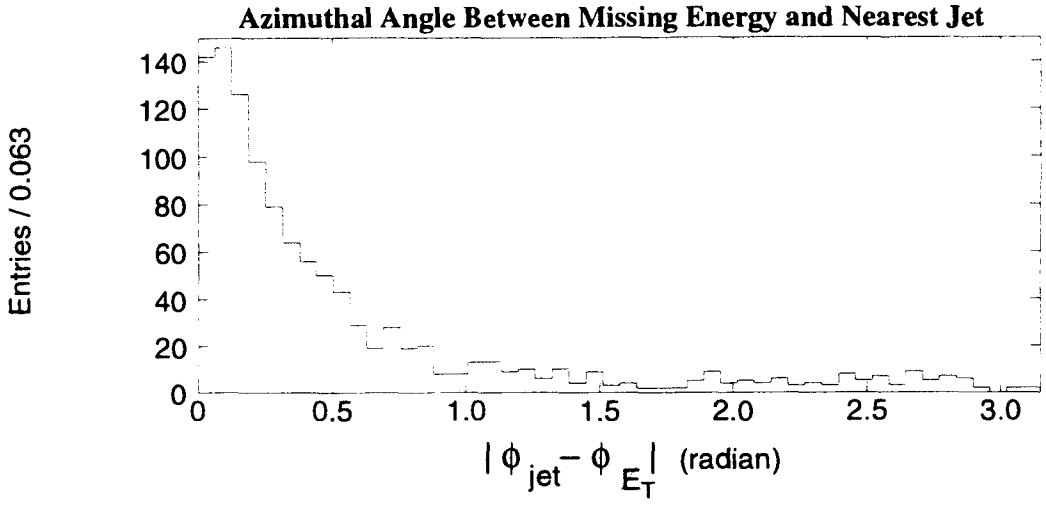

Figure 6.2: The ϕ angle between the $\not\!\!H_T$ vector and the nearest jet. The jet clustering was done with a cone of $\Delta R = 0.4$.

strong correlation. Figure 6.2 shows the ϕ angle between the $\not\!\!E_T$ vector and the nearest jet in JET_20 events with more than 20 GeV $\not\!\!E_T$. The spike near zero indicates that the $\not\!\!E_T$ vector was near a jet. More precisely, given a jet clustering cone of $\Delta R = 0.4$, the $\not\!\!E_T$ vector was inside a jet. This is consistent with the assumption that the missing energy resulted from a mismeasured jet.

This is not necessarily the case when real neutrinos are present. For the the case of $W \longrightarrow e\ \nu_e$ + jets the angle between the $\not\!\!E_T$ direction (which should be dominated by the ν_e) and the other jets is less correlated. Figure 6.3 shows this distribution. There is a slight bias in the plot toward the low end introduced by the definition of the variable being plotted.

A requirement of $\Delta\phi \geq 0.5$ radian between the $\not\!\!E_T$ vector and the nearest jet is imposed, providing considerable rejection against background while maintaining acceptable efficiency for signal. The efficiency decreases at larger jet multiplicities from the higher likelihood that one of the jets will happen to be near the neutrino.

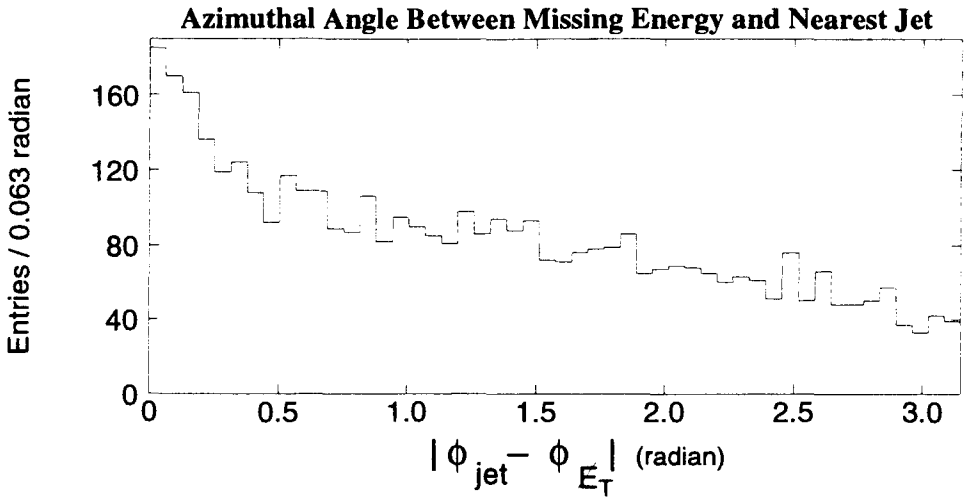

Figure 6.3: The ϕ angle between the $\not\!\!E_T$ vector and the nearest jet in $W \longrightarrow e + \nu_e +$ jets events.

A cut on the uncertainty on the location of the primary vertex is made to provide confidence in the validity of the impact parameters. This cut is a function of the jet multiplicity of the events. Events with large numbers of jets tend to have large numbers of tracks, which assist in the reconstruction of the primary vertex location. As will be seen in section 6.1.3, the cut removes only a few percent of the events at high jet multiplicities.

The jet requirements used from the monojet selection criteria are here repeated.

6.1.3 Efficiencies

The event selection efficiencies are determined from a combination of Monte Carlo and data. Modeling of the τ decays and their affect on the efficiency is based the ISAJET [29] Monte Carlo. The efficiency of the CFT at locating the tau-descendent tracks at the Level 2 trigger is derived from the minbias and JET_20 data. However, some of the more difficult variables to simulate, such as the $\not\!\!E_T$ distribution, require a combination of data and Monte Carlo. Data $W \longrightarrow e + \nu_e$ events are used, with the electron replaced by a simulated

tau. In the absence of accurate Monte Carlo representation of the underlying event and the corresponding detector response, this is believed to be the most reliable estimate of the correct behavior.

The narrow kinematic region allowed for the identification of tau jets has the added advantage of limiting the range of those quantities dependent on the jet energy. This being the case, the efficiency is factored into those portions which are essentially constant over the energy range in question and those portions which affect the total number of events in that energy range. The Monte Carlo shows this to be an accurate approximation to within 5%, which is taken as a systematic error.

Analysis begins with the Level 2 trigger response to hadronic tau jets. Figure 6.4 shows that the number of trigger towers in Monte Carlo tau decays is largely independent of the energy of the jet in the region of interest. A value of $82 \pm 4\%$ is taken for the efficiency of this criterion.

The CFT track requirement used in the Level 2 tau trigger is difficult to model in the Monte Carlo. Tracks from the dijet events are used to determine the efficiency with which the CFT will find tracks passing the 4.8 GeV/c cut. The jet triggers are based on calorimetry and introduce no tracking bias. The CFT efficiency is plotted as a function of track P_T in figure 6.5.

Because the CFT is not fully efficient for the 5 GeV/c P_T cut used in selecting tau candidate jets, the CFT efficiency curve must be convolved with the P_T spectrum of the lead track from the tau decays (figure 4.5). Monte Carlo taus are generated with $P_T > 20$ GeV/c The requirement that the tau have at least 20 GeV/c P_T in the Monte Carlo results in an overall CFT efficiency for the taus in question of $92 \pm 2\%$.

The efficiency estimate for the E_T cut at Level 2 trigger is computed from the Monte Carlo. As mentioned in chapter 2, the E_T computed by the Level 2 trigger is based on the assumption that the primary vertex is located at the CDF origin. This affect can be accounted for in the Monte Carlo by an acceptable modeling of the primary vertex

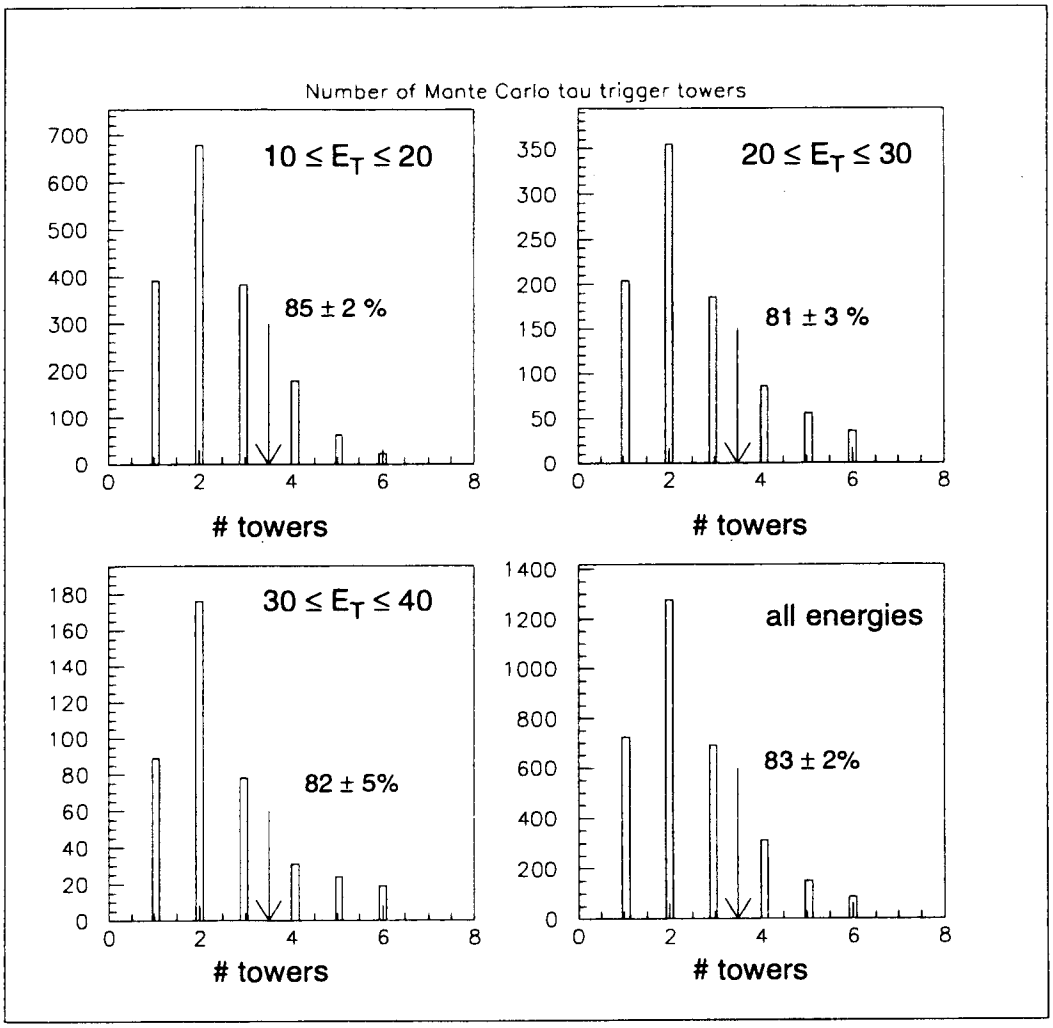

Figure 6.4: The number of calorimetry trigger towers at Level 2 for Monte Carlo τ jets.

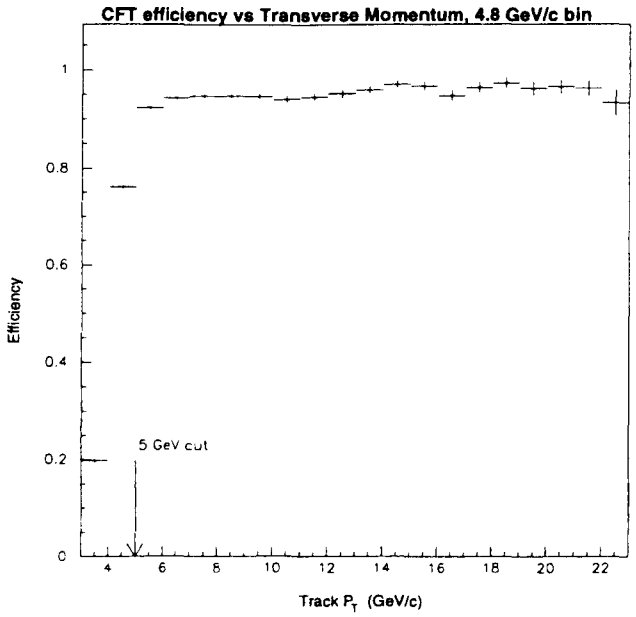

Figure 6.5: The efficiency of the CFT versus the track P_T for a nominal cut of 4.8 GeV/c. The tau-jet selection requirement of 5 GeV/c is also shown, and it is of note that the CFT is not fully efficient for a 5 GeV/c cut.

distribution, as is computed in appendix B. A 2% systematic error is assigned from the uncertainty in the primary vertex distribution.

The Level 3 tau trigger TAU_10_MET_20 has two main components, a tau-finding subroutine and a dijet removal cut discussed earlier. Because the tau-jet selection criteria used are uniformly more restrictive than that used in the Level 3 tau-finding module, the Level 3 tau results are ignored.

To study the dijet rejection at Level 3, a comparison of the $\Delta\phi(\not\!\!E_T, \text{jets})$ distribution both in Monte Carlo and in data is made. The results obtained from the $W \longrightarrow e\,\nu_e$ events and from VECBOS Monte Carlo are consistent.

There are other factors involved in the calculation of the efficiency. Implicit in the cut on the jet energy is the energy of the tau lepton. In all Monte Carlo studies the tau is required to have a P_T of at least 20 GeV. It is also required that the tau be within the SVX

fiducial volume (this is correlated with both the longitudinal distribution of the primary vertex and the P_T of the tau). These determinations are made by replacing the electron in real $W \longrightarrow e + \nu_e$ events with taus generated by Monte Carlo.

The fraction of taus which decay hadronically is well–measured, and is included in the efficiency calculations.

6.2 Tagging Results

The selection criteria are applied in a search of the Exotics data stream. The events are then categorized by the number of energetic jets (other than the tau candidate jet). Only jets with energy-corrected E_T of 15 GeV are counted. (Energy correction accounts for energy outside the clustering cone and known calorimeter gaps. This correction is applied to compare with results from other analyses, and is not applied to the tau jets.)

6.2.1 $W + 0$ Jet

This sample is similar to the monojet sample created earlier, but has lower statistics because of the trigger requirements placed on the data. However, the data are sufficient to allow the evaluation of the combined jet probability and η-width tagging algorithm. Consider first the sample before tagging.

Figure 6.6 shows strong peaks in the 1–prong and 3–prong bins in the track multiplicity distribution. A fit of the track multiplicity indicates 420 $\pm$ 14 taus and 384 $\pm$ 14 background events. From this sample the efficiency of the combined jet probability η-width cut on the data is determinable.

Application of the following tag to the sample:

- $0.005 < \mathcal{P}_{jet} < 0.200$ (using all tracks)
- $\langle \eta \rangle < 0.060$

gives the track multiplicity distribution shown in figure 6.7. The fit of the distribution gives 143^{+2}_{-5} taus and 5^{+5}_{-2} background events, which is a considerably higher fractional tau content than before tagging. This indicates that the tagging was successful. With the knowledge of the number of taus present before and after tagging, the efficiency of the tagger is calculated:

$$\epsilon \equiv \frac{143^{+2}_{-5}}{420 \pm 14} = 0.35 \pm 0.03$$

including the statistical errors on the fit values.

The limited statistics of the sample contribute to the uncertainty in the background estimation. An unrelated method of background estimation is derived from the study of the effect of the tagger on the background in chapter 5. With the track multiplicity distribution of the sample before tagging known, the bin-by-bin reject factors obtained from the control sample are used to obtain a (conservative) estimate of the number of background events passing the cut. Doing so gives a background value of 6.6 ± 0.8 events, which is consistent with the result from the track multiplicity distribution.

Because there is little variation in the efficiency of the jet probability and the η-width cuts within the limited kinematic regime used here, this number is treated as constant for the remainder of the W studies.

The complete efficiency values for this sample are given in table 6.2. To avoid problems from using, then compensating for, the jet probability + η-width cut which was derived from the sample, the cross-section computed from the untagged sample is used for monojet events.

6.2.2 $W + 1$ Jet

The next sampled considered is the case in which there is another jet in the event, whether from initial or final state radiation. The difficulty in observing such events stems from the large QCD background. Even with the restrictive cuts used here, an untagged sample is not highly enriched in taus. The track multiplicity distribution for the untagged sample is shown in figure 6.8, and gives no obvious surplus of 1–prong and 3–prong jets.

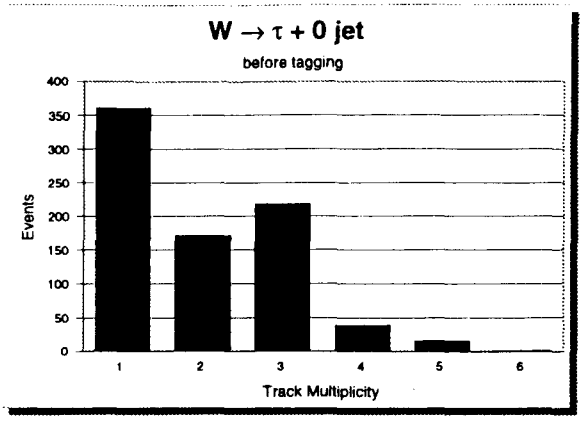

Figure 6.6: The track multiplicity distribution of the $W + 0$ jet sample before tagging.

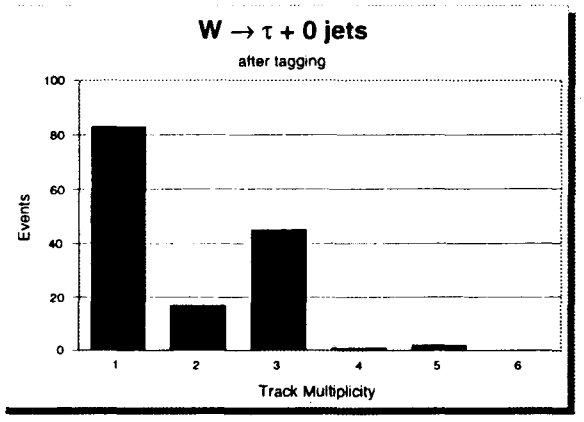

Figure 6.7: The track multiplicity distribution of the $W + 0$ jet sample after tagging.

	Efficiencies for $W \longrightarrow \tau\ \nu_\tau$	
Lepton P_T and SVX fiducial:	0.218 ± 0.005	
Tracking Isolation:	0.886 ± 0.011	
$\Delta\phi$(jet,$\not\!\!E_T$):	0.975 ± 0.012	
Level 3 dijet removal:	0.981 ± 0.015	
25 GeV $\leq \not\!\!E_T \leq$ 40 GeV:	0.747 ± 0.013	
$\sigma_{VXPRIM} \leq 40\ \mu m$:	0.87 ± 0.01	
Total topological efficiency:		0.120 ± 0.005
tau hadronization:	0.639 ± 0.001	
tau kinematic selection:	0.21 ± 0.01	
Level 2 efficiency:	0.77 ± 0.05	
Total kinematic efficiency:		0.103 ± 0.081
Total selection efficiency:		0.0123 ± 0.0010
Jet Probability and η-width:		0.35 ± 0.03
Overall Efficiency		0.0043 ± 0.0005

Table 6.2: Efficiencies for $W \longrightarrow \tau + \nu_\tau + 0$ jet.

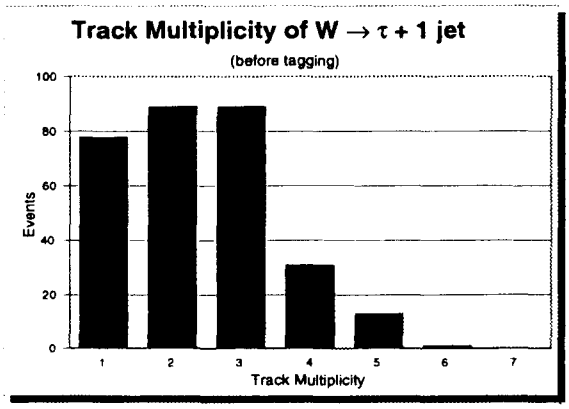

Figure 6.8: The track multiplicity distribution of the $W + 1$ jet sample before tagging.

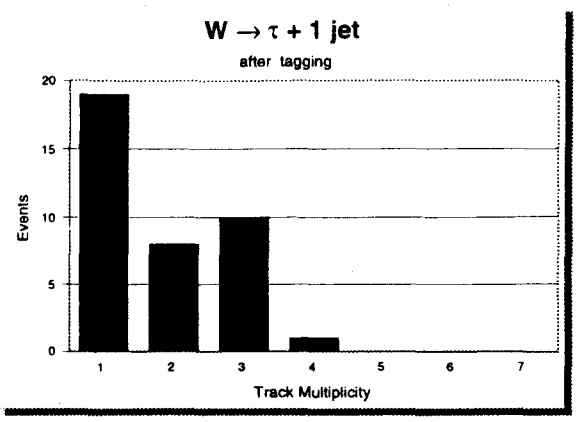

Figure 6.9: The track multiplicity distribution of the $W + 1$ jet sample after tagging.

After the jet probability and η-width cuts are applied, the situation is different. Figure 6.9 shows a marked excess of odd-numbered tracks with respect to the expected background distribution (see figure 5.14), indicating a high content of tau jets. A fit of the data indicates 26 ± 4 taus, with 12 ± 4 background events.

Using the background rejection factors to estimate the amount of background remaining in the tagged sample gives a result of 8.5 ± 0.5 background events, which is consistent with that fit above. It is interesting to note that the shape and size of the predicted background is considerably different from the distribution after tagging (figure 6.10), showing that the surplus in the 1–prong and 3–prong bins is unlikely to be the result of a fluctuation in the background. The efficiencies for the $W+1$ jet events are given in table 6.3.

6.2.3 $W + 2$ Jets

The analysis is repeated, this time searching for events in which there are two additional jets. Before the application of the tau-tagger, the track multiplicity distribution looks much like the expected QCD background (figure 6.11). After tagging, there is a surplus of 1–prong and 3–prong jets. Figure 6.12 shows the track multiplicity distribution after tagging, along with the prediction of the background from the pre-tagged sample.

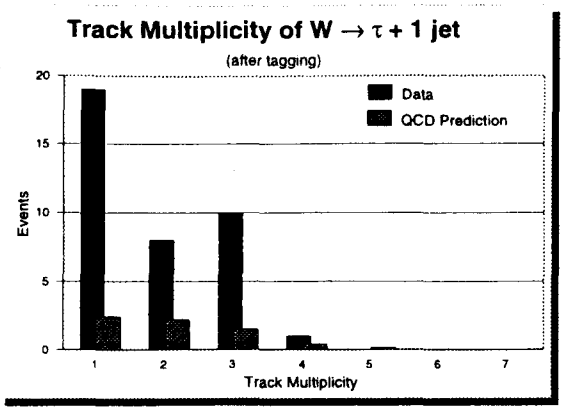

Figure 6.10: The track multiplicity distribution of the $W + 1$ jet sample after tagging, alongside the background estimation from the JET_20 control sample.

	Efficiencies for $W \longrightarrow \tau + \nu_\tau + 1$ Jet	
Lepton P_T and SVX fiducial:	0.28 ± 0.01	
Tracking Isolation:	0.85 ± 0.05	
$\Delta\phi$(jet,$\not\!\!E_T$):	0.91 ± 0.06	
Level 3 dijet removal:	0.73 ± 0.06	
25 GeV $\leq \not\!\!E_T \leq$ 40 GeV:	0.57 ± 0.03	
$\sigma_{VXPRIM} \leq 40\ \mu m$:	0.94 ± 0.01	
Total topological efficiency:		0.086 ± 0.011
tau hadronization:	0.639 ± 0.001	
tau kinematic selection:	0.21 ± 0.01	
Level 2 efficiency:	0.77 ± 0.05	
Total kinematic efficiency:		0.103 ± 0.081
Total selection efficiency:		0.0090 ± 0.0014
Jet Probability and η-width:		0.35 ± 0.03
Overall Efficiency		0.0032 ± 0.0006

Table 6.3: Efficiencies for $W \longrightarrow \tau + \nu_\tau + 1$ jet.

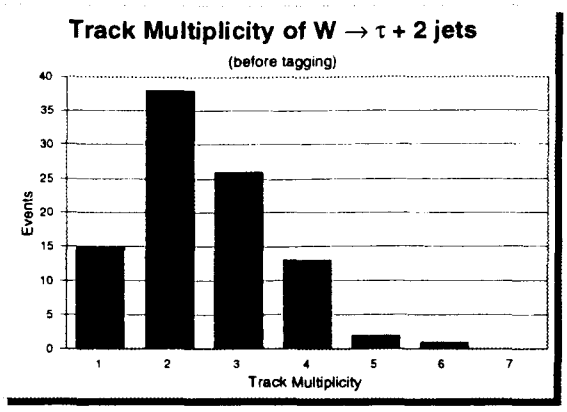

Figure 6.11: The track multiplicity distribution of the $W + 2$ jets sample before tagging.

The background estimation of 2.6 $\pm$ 0.4 events obtained from the QCD rejection factors is consistent with the track multiplicity fit value of 3^{+3}_{-2} tau jets with 3^{+2}_{-3} background. The large error on the track multiplicity fit is due to the low statistics of the sample. That the two estimates agree so well is fortuitous and does not necessarily indicate the exact knowledge of the background. Nonetheless, 3 signal events are claimed in the sample for purposes of cross-section calculations. The efficiencies for the $W + 2$ jet events are given in table 6.4.

6.2.4 $W + 3$ Jets

Next considered is the case in which there are three additional jets in the event. Few events of this type pass the selection criteria, due largely to the Level 3 dijet cut and the $\Delta\phi$ cut on the $\not\!\!E_T$. The track multiplicity of pre–tagged tau candidate jets is shown in figure 6.13. After tagging, a single event remains (figure 6.14).

It is difficult to make any statements about the remaining event. The estimated background (from the pre-tagged case) is 0.6 events, which is consistent with the observed data, although this is a conservative estimate by design. For purposes of comparing with other measurements, a claim 1 signal event with an uncertainty of 1 event is made.

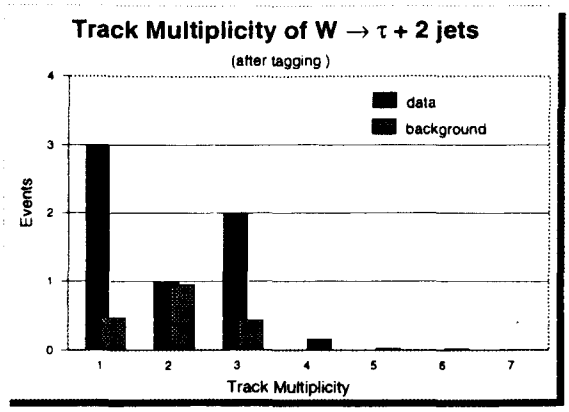

Figure 6.12: The track multiplicity distribution of the W + 2 jets sample after tagging, alongside the background estimation from the JET_20 control sample.

	Efficiencies for $W \longrightarrow \tau + \nu_\tau$ + 2 Jets	
Lepton P_T and SVX fiducial:	0.30 ± 0.01	
Tracking Isolation:	0.80 ± 0.05	
$\Delta\phi$(jet,$\not\!\!E_T$):	0.76 ± 0.06	
Level 3 dijet removal:	0.70 ± 0.06	
25 GeV $\leq \not\!\!E_T \leq$ 40 GeV:	0.51 ± 0.05	
$\sigma_{VXPRIM} \leq 40\ \mu m$:	0.97 ± 0.01	
Total topological efficiency:		0.063 ± 0.011
tau hadronization:	0.639 ± 0.001	
tau kinematic selection:	0.21 ± 0.01	
Level 2 efficiency:	0.77 ± 0.05	
Total kinematic efficiency:		0.103 ± 0.081
Total selection efficiency:		0.0065 ± 0.0011
Jet Probability and η-width:		0.35 ± 0.03
Overall Efficiency		0.0023 ± 0.0004

Table 6.4: Efficiencies for $W \longrightarrow \tau + \nu_\tau$ + 2 jets.

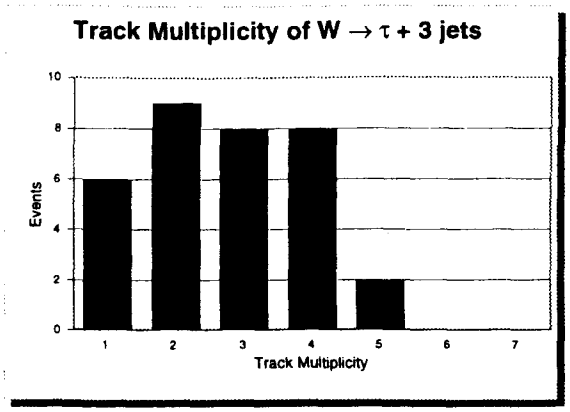

Figure 6.13: The track multiplicity distribution of the $W + 3$ jets sample before tagging.

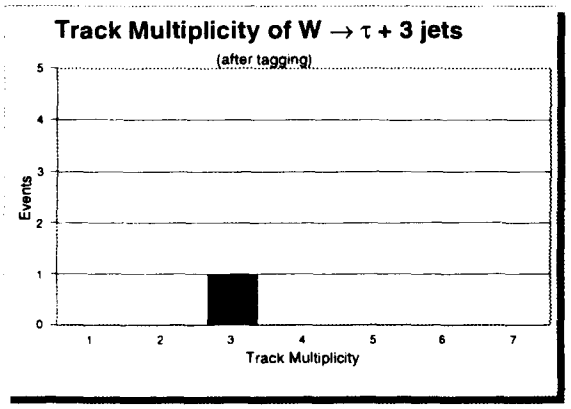

Figure 6.14: The track multiplicity distribution of the $W + 3$ jets sample after tagging. It is unknown whether the remaining event is signal or background.

The efficiencies for this data set are given in table 6.5.

6.3 Non-W Sources of Taus

The calculations in the preceding section yield the tau content. However, there is no specific means of distinguishing the τ's produced from W bosons with those from

Efficiencies for $W \longrightarrow \tau + \nu_\tau + 3$ Jets		
Lepton P_T and SVX fiducial:	0.36 ± 0.02	
Tracking Isolation:	0.80 ± 0.05	
$\Delta\phi$(jet,$\not\!\!E_T$):	0.69 ± 0.06	
Level 3 dijet removal:	0.60 ± 0.06	
25 GeV $\leq \not\!\!E_T \leq$ 40 GeV:	0.36 ± 0.03	
$\sigma_{VXPRIM} \leq 40\ \mu m$:	0.97 ± 0.01	
Total topological efficiency:		0.043 ± 0.009
tau hadronization:	0.639 ± 0.001	
tau kinematic selection:	0.21 ± 0.01	
Level 2 efficiency:	0.77 ± 0.05	
Total kinematic efficiency:		0.103 ± 0.081
Total selection efficiency:		0.0045 ± 0.0011
Jet Probability and η-width:		0.35 ± 0.03
Overall Efficiency		0.0016 ± 0.002

Table 6.5: Efficiencies for $W \longrightarrow \tau + \nu_\tau + 3$ jets.

Number of Jets in event	Events Expected (before tag)	Events Expected (after tag)
0	8.5 ± 1.7	3.0 ± 0.6
1	1.2 ± 0.6	0.4 ± 0.2
2	0.3 ± 0.2	0.11 ± 0.08
3	< 0.01	< 0.01

Table 6.6: Estimated number of events from $Z \longrightarrow \tau\ \tau$

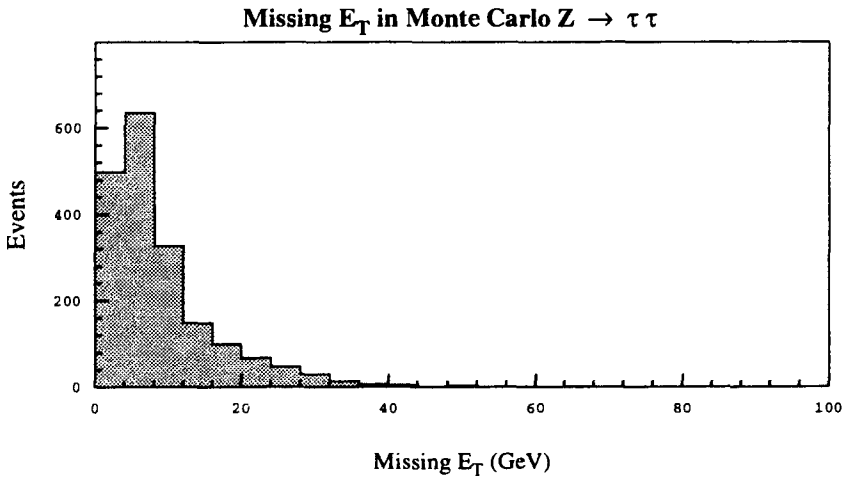

Figure 6.15: Missing transverse energy in Monte Carlo $Z \longrightarrow \tau\tau$ events.

other sources. It is necessary to consider alternate sources of high-P_T τ production before calculating the cross-sections for the W sources.

Other than $W \longrightarrow \tau\ \nu_\tau$, it is believed that the dominant source of energetic taus is the process $Z \longrightarrow \tau\ \tau$, with one or both taus decaying hadronically. This background is small. As shown in figure 6.15, the vector sum of the neutrino momenta in such events tends toward zero. Few Z events pass the $\not\!\!E_T$ requirement of the Level 2 tau trigger. Additionally, the tau jets typically recoil off each other. This results in event rejection by the Level 3 dijet removal. The estimated background from Z bosons is given in table 6.6.

Another possible source of taus is the decay of top quarks. The recent observation

# Jets	# of Events	# of taus	Non-W taus	W events
0	804	420 ± 14	8.5 ± 1.7	411 ± 14
1	38	26 ± 4	0.4 ± 0.2	26 ± 4
2	6	3 ± 0.4	0.12 ± 0.10	3 ± 0.4
3	1	1	< 0.01	1

Table 6.7: Event accounting for $W \longrightarrow \tau + jets$.

of top quark production at CDF [38], with the consequent measurements of top quark mass and pair production cross-section, allows the calculation of the contribution from this source. The published values of $m_{top} = 176$ GeV/c^2 and $\sigma(t\bar{t}) = 6.8$ pb are used in Isajet Monte Carlo studies to estimate the number of $t\bar{t}$ events which pass the W selection criteria. In the Run 1a data, the expected background from top is less than 0.01 event.

The accounting for the W + jets analysis is summarized in table 6.7.

Chapter 7

A Top Quark Search Via Tau Decay Modes

Few top quark events are expected to pass the tight cuts imposed in the W + jets analysis of chapter 6. However, it is possible to choose different kinematic and topological cuts favoring the acceptance of top quark events. The availability of a tau tagging algorithm permits the extension of top quark analyses into the tau–inclusive decay channels.

The Standard Model predicts that the dominant source of heavy top quarks in $\bar{p}p$ collisions at Tevatron energies is the production of top quark pairs from valence quark annihilation in the proton and antiproton. Figure 7.1 [37] shows this mechanism at the tree–level. The presence of the two real W bosons provides a source for the high–P_T τ leptons for which the tagger has been developed. Table 7.1 gives the expected decay modes of the top quark. The large QCD cross–section makes identification of the all–hadronic decay modes difficult. Most searches [38, 39] involved only those modes in which an electron or muon is produced by the W boson decays. Addition of the modes in which one of the W's decays into a τ increases the searchable branching ratio from $\sim$ 34% to $\sim$ 56%.

7.1 Loose Tau Tag

Because the production rate of top-antitop events is lower than that of W + jet events [38], a looser tau tag is needed. Herein lies the advantage of a continuous variable

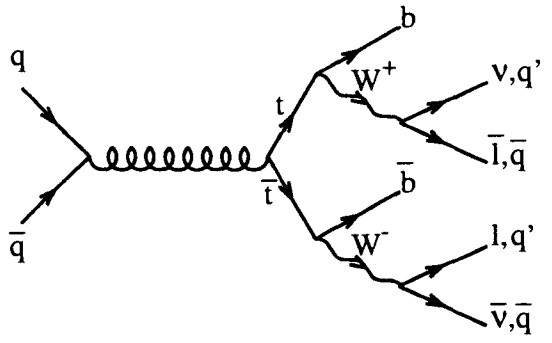

Figure 7.1: The production, and subsequent decay, of top quark pairs from quark annihilation.

Decay mode	Branching ratio
$t\bar{t} \longrightarrow (q\bar{q}'b)(q\bar{q}'\bar{b})$	36/81
$t\bar{t} \longrightarrow (q\bar{q}'b)(e\nu_e\bar{b})$	12/81
$t\bar{t} \longrightarrow (q\bar{q}'b)(\mu\nu_\mu\bar{b})$	12/81
$t\bar{t} \longrightarrow (q\bar{q}'b)(\tau\nu_\tau\bar{b})$	12/81
$t\bar{t} \longrightarrow (e\nu_e b)(\mu\nu_\mu\bar{b})$	2/81
$t\bar{t} \longrightarrow (e\nu_e b)(\tau\nu_\tau\bar{b})$	2/81
$t\bar{t} \longrightarrow (\mu\nu_\mu b)(\tau\nu_\tau\bar{b})$	2/81
$t\bar{t} \longrightarrow (e\nu_e b)(e\nu_e\bar{b})$	1/81
$t\bar{t} \longrightarrow (\mu\nu_\mu b)(\mu\nu_\mu\bar{b})$	1/81
$t\bar{t} \longrightarrow (\tau\nu_\tau b)(\tau\nu_\tau\bar{b})$	1/81

Table 7.1: Standard model decay modes for a $t\bar{t}$ pair to lowest order, where q represents light quarks (u, d, c, s).

for tagging, as is the case for the jet probability tag. For the top quark searches detailed below, the following tau tag

- $\mathcal{P}_{jet} < 0.250$ (using all tracks)
- $\langle \eta \rangle < 0.060$

is used. This provides an estimated efficiency of $(45 \pm 6)\%$ for τ's from top decay, with a background rejection factor of ~ 20.

7.2 Dilepton Top Search

Those decay channels in which both of the W's from the top pair decay leptonically are referred to as the "dilepton" decay modes. These are particularly useful because the presence of two high-P_T leptons greatly reduces the background. Only those event topologies in which at least one tau decays hadronically are investigated in this analysis.

7.2.1 $t\bar{t} \longrightarrow \tau + \tau + jets$

Considered first is the case with two hadronic tau jets in the final state. The following selection criteria are used:

- $\not\!\!E_T > 20$ GeV
- event satisfied the TAU_20_MET_20 Level 2 trigger
- event satisfied the TAU_10_MET_20 Level 3 trigger
- $\Delta\phi(\not\!\!E_T, \text{jets}) > 0.5$
- $\sigma_{VXPRIM} \leq 40\ \mu m$
- at least 2 jets satisfying the τ jet kinematic requirements
- $\Delta\phi(\tau_1, \tau_2) < 165^\circ$

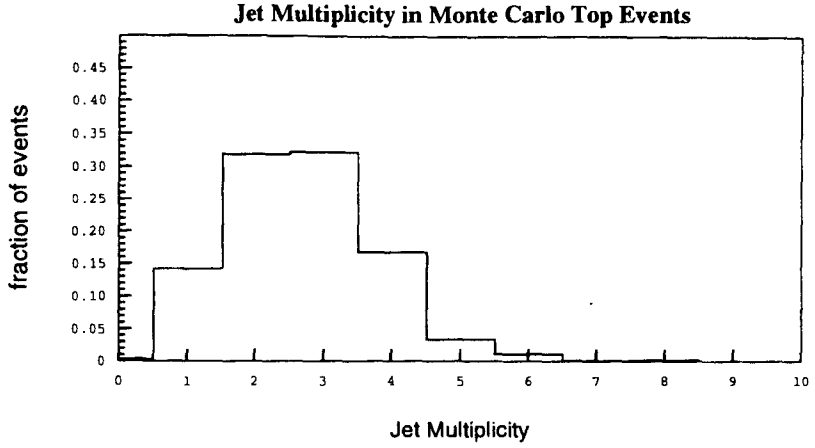

Figure 7.2: The distribution of the number of jets with $E_T > 15$ GeV in Monte Carlo top events.

- at least 2 other jets with $E_T > 15$ GeV

The kinematic requirements on the τ–candidate jets are the same as those used in chapter 6, with the exception that no upper bound is placed in the energy of the τ jet. This modification is necessary due to the large mass of the top quark, whose decay imparts considerable momentum to the W bosons and thus to the tau.

The presence of the bottom quarks in top events often results in hadronic jets (in addition to any jets from quark/gluon radiation). Figure 7.2 shows the expected jet multiplicity distribution (excluding any τ jets) for a top mass of 180 GeV/c^2. To reduce the background, selected events are required to have at least two jets.

There are no events satisfying these criteria in the Run 1a data.

7.2.2 $t\bar{t} \longrightarrow (e/\mu) + \tau + jets$

Next, the high-P_T electron and muon data sets from Run 1a [21] are checked for e $-$ τ and $\mu - \tau$ events. Because the high-P_T electron and muon triggers are much more

efficient than the corresponding triggers for τ jets, they are used for event selection in this search.

Electrons used are required to have passed the Level 1, Level 2, and Level 3 electron triggers, as well as additional offline criteria. The central electron trigger at Level 1 requires that there be a single trigger tower with $E_T > 6\ GeV$ in the CEM or $E_T > 8$ GeV in the CHA. The Level 2 central electron trigger selects those candidates with an energy cluster of $E_T > 9$ GeV and an associated CFT track of $P_T > 9.2$ GeV/c. It is further required that the ratio of hadronic to electromagnetic energy in the cluster be less than 0.125. The high-P_T electron trigger at Level 3 requires that a cluster of $E_T > 18$ GeV be associated with a CTC track of $P_T > 13$ GeV/c . The central electron trigger has been measured to be $(92.8 \pm 0.2)\%$ efficient for electrons in the range $20 < E_T < 150\ GeV$ [21].

Additional cuts on central electron candidates are made offline. A fiducial cut on the location of the cluster is made to ensure that the electron candidate is not near a calorimeter boundary. Electrons from photon conversions ($\gamma \longrightarrow e^+e^-$) are removed. Both the ratio of the hadronic energy to the electromagnetic cluster energy and the ratio of the energy to the momentum of the associated track are considered to remove charged hadrons. The lateral shower profile (L_{SHR}) and a χ^2 based on the CES shower profile are compared against data from test-beam electrons. The quality of the track association is given by the projected distance from the track to the cluster, both in the $r - \phi$ (Δx) and z (Δz) views. The difference in z from the reconstructed track and that from the primary vertex is considered. Furthermore, a calorimetry–based isolation cut is made on the electron, in which the fraction energy in a cone of $\Delta R < 0.4$ about the electron direction not contained by the electron tower is computed.

The values for the offline selections used here are given in table 7.2. The measured efficiency for the offline electron identification is $84 \pm 2\%$ [21] before isolation requirements.

The selection of high-P_T muons begins with the requirements made by the online muon triggers. The Level 1 central muon trigger (see section 2.3.1) requires a CMU muon track segment of $P_T > 6$ GeV/c in coincidence with hits in the CMP, or a CMX track

Variable	Cut
HAD/EM	< 0.05
E/P	< 1.5
$L_{SHR} < 0.2$	
$\|\Delta x\|$	$< 1.5cm$
$\|\Delta z\|$	$< 3.0cm$
CES χ^2	< 10
z-vertex match	$< 5.0cm$
Isolation	< 0.1

Table 7.2: Offline central electron selection criteria.

segment of $P_T > 10$ GeV/c in coincidence with scintillators sandwiching the chambers. The Level 2 muon trigger requires the association of a CFT track of $P_T > 9.2$ GeV/c with a Level 1 muon candidate. The algorithm used by the Level 3 high-P_T muon trigger demands that the muon candidate be associated with a CTC track of $P_T > 18$ GeV/c. This is done by requiring that the extrapolation of the CTC track to the muon chambers be within 10 cm of the reconstructed muon segment. The track is also extrapolated to the central calorimeter to determine which tower the muon candidate traversed. The energy deposition in that CHA tower is required to be less than 6 GeV. The CMU (CMX) trigger efficiency is measured [21] to be $(86.8 \pm 1.9)\%$ ($(54.4 \pm 5.5)\%$) for muons with $P_T > 20$ GeV/c.

Offline identification of central ($|\eta| < 1.0$) muons involves further calorimeter and track requirements. Cuts are placed on the amount of calorimeter energy to insure consistency with the hypothesis of the presence of a minimum-ionizing particle. Cosmic rays are removed by placing restrictions on the impact parameter of the muon track. An isolation requirement analogous to that used for electron identification is imposed on the data, with the P_T of the muon used rather than the energy. A summary of these requirements is given in table 7.3. The efficiency of the offline muon selection, excluding the isolation requirement, is measured to be $(90.6 \pm 1.4)\%$ [21].

An identified lepton (electron or muon) with $P_T > 20$GeV/c is required, per the criteria listed above. Only one such lepton is permitted in selected events to reduce back-

Variable	Cut
EM energy	< 2 GeV
HAD energy	< 6 GeV
$\|\Delta x\|$	$< 2.0cm$ (CMU)
	$< 5cm$ (CMP,CMX)
Impact parameter	$< 3.0mm$
z-vertex match	$< 5.0cm$
Isolation	< 0.1

Table 7.3: Offline central muon selection criteria. The variable $\Delta x = r \times \Delta\phi$ is defined in the text.

ground from $Z \longrightarrow l^+l^- + jets$. At least one τ candidate jet is required in each event, where the τ jet satisfies the kinematic requirements given in section 7.2.1. It is observed that there are no events in the remaining sample with more than one jet passing the τ selection criteria, but this limitation is not imposed. The leptons from the W's in $t\bar{t}$ decay are of opposite sign. Accordingly, a requirement that the identified leptons be of opposite sign is made on the data sample.

The sought dilepton events have two (typically) energetic neutrinos from the W decays, resulting in large amounts of missing energy (see figure 7.3). As such, only candidate events with $\not\!\!E_T > 25$ GeV are kept. To reduce the background from mismeasured jets, a cut is made on the azimuthal angle between the missing E_T direction and the jet nearest the $\not\!\!E_T$. Because the jet multiplicity of top events is expected to be higher than for the W events in chapter 6, a looser cut of $\Delta\phi(\not\!\!E_T, \text{jets}) > 15°$ is used (see figure 7.4).

The leptons in Z boson decays are usually produced back–to–back in the transverse plane, whereas this is not the case for leptons in $t\bar{t}$ events (figure 7.5). To reduce the background from $Z \longrightarrow \tau\tau$ where one τ decays leptonically and the other decays hadronically, the azimuthal angle between the identified leptons is required to be $< 165°$.

Two $\mu - \tau$ events and two $e - \tau$ events pass these cuts. The properties of the tau candidate jets are summarized in table 7.4. These events are displayed in figures 7.6,7.7, 7.8, and 7.9.

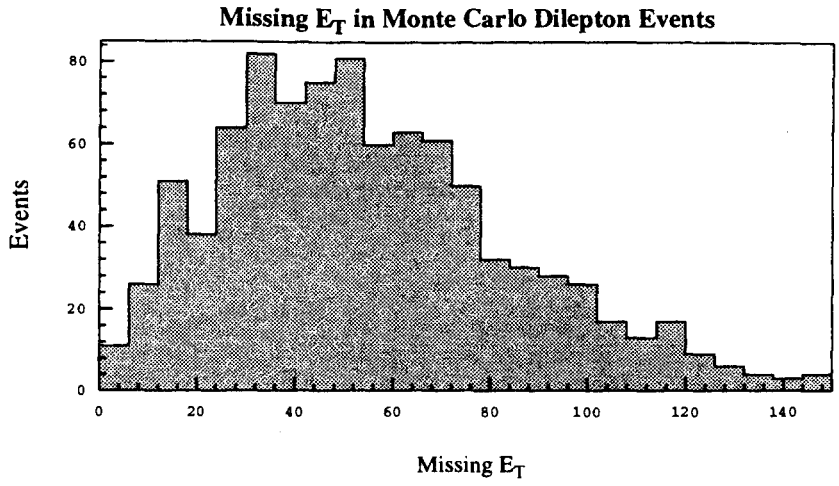

Figure 7.3: The $\not\!\!E_T$ in Monte Carlo $t\bar{t} \longrightarrow e/\mu + \tau$ dilepton events.

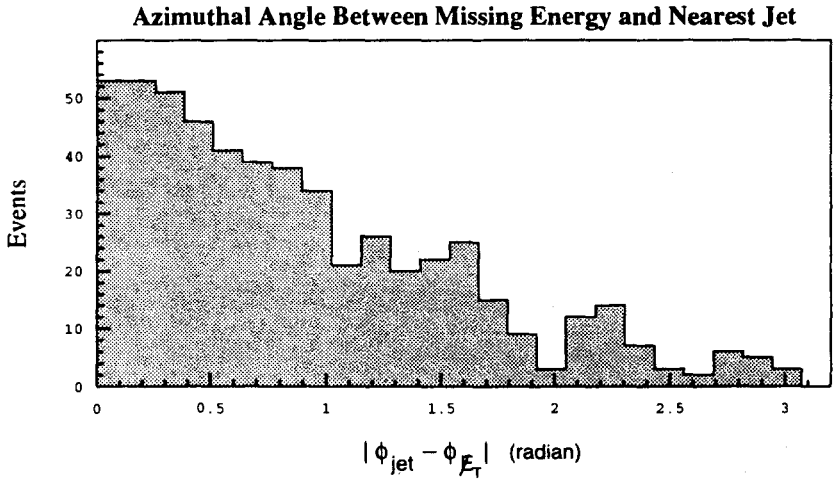

Figure 7.4: The azimuthal angle between the $\not\!\!E_T$ vector and the nearest jet of $E_T > 10\,GeV$, in Monte Carlo $t\bar{t}$ dilepton events.

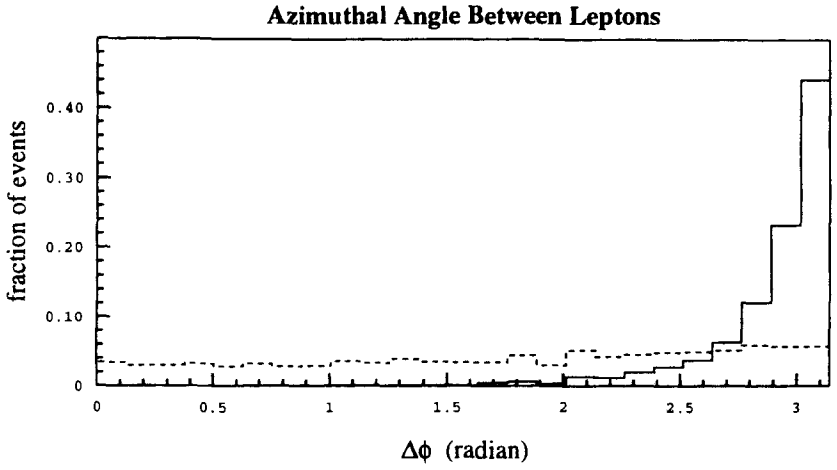

Figure 7.5: Azimuthal angle between leptons in $Z \longrightarrow \tau\tau$ (solid histogram) events and leptons in $t\bar{t} \longrightarrow l + \tau + \ jets$ (dashed histogram) events. Based on Monte Carlo.

Event	Run #	Event #	τ jet E_T	# of tracks	Jet Probability	η-width
A.	41735	15631	24.9	3	0.964	0.078
B.	45047	104393	30.3	1	0.002	0.047
C.	42727	81408	40.4	1	0.641	0.086
D.	45880	31838	84.2	1	0.990	0.059

Table 7.4: A summary of the τ candidate jets in the dilepton top search, before tau-tagging.

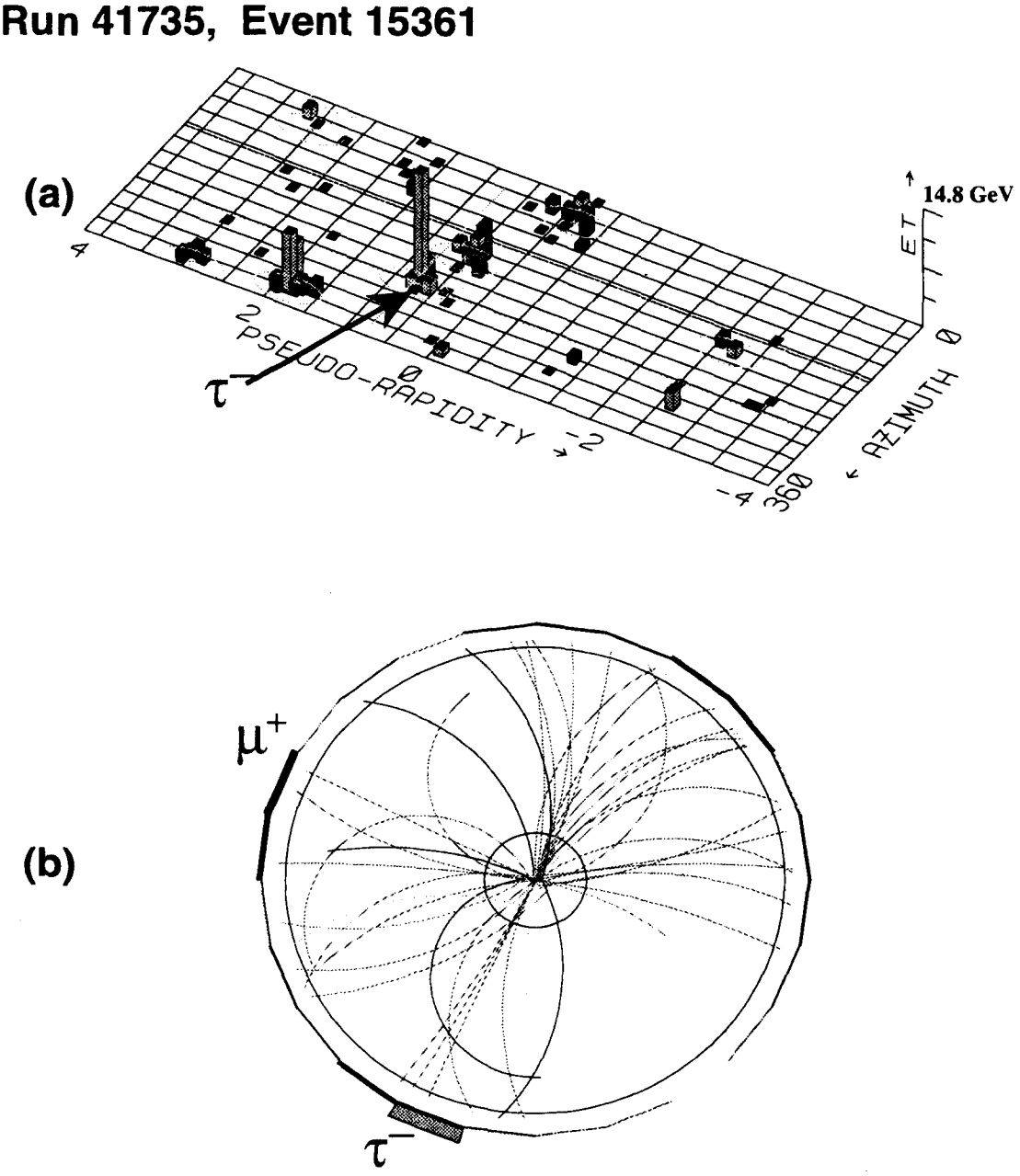

Figure 7.6: Event display for a candidate $\mu - \tau$ event. Figure (a) shows the observed calorimeter E_T in the $\eta - \phi$ plane. Figure (b) gives a transverse view of the CTC shows the reconstructed charged tracks.

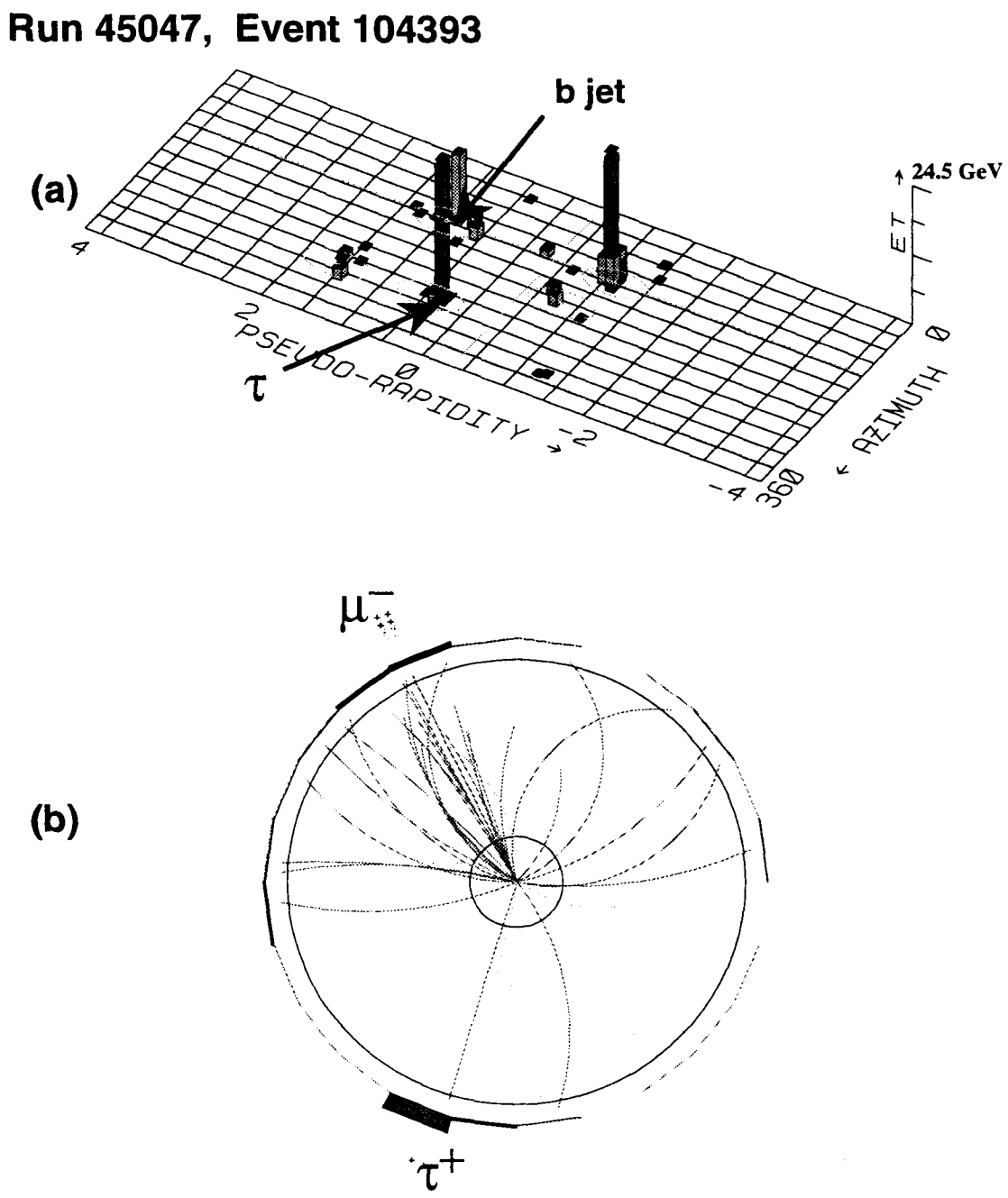

Figure 7.7: Event display for a candidate $\mu - \tau$ event. Figure (**a**) shows the observed calorimeter E_T in the $\eta - \phi$ plane. Figure (**b**) gives a transverse view of the CTC shows the reconstructed charged tracks. The jet satisfying an SVX b quark tagging algorithm is indicated.

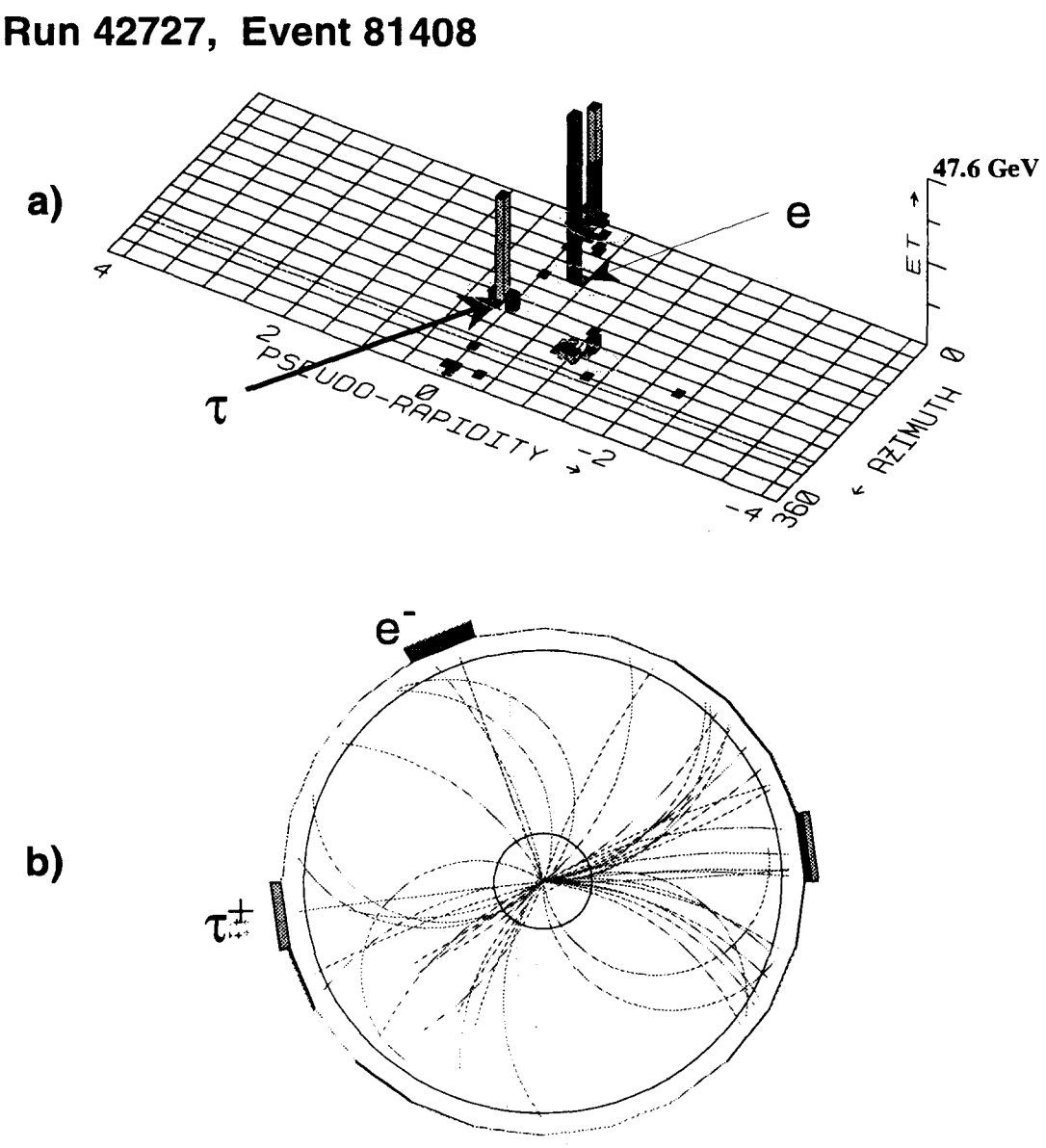

Figure 7.8: Event display for a candidate $e - \tau$ event. Figure **(a)** shows the observed calorimeter E_T in the $\eta - \phi$ plane. Figure **(b)** gives a transverse view of the CTC shows the reconstructed charged tracks.

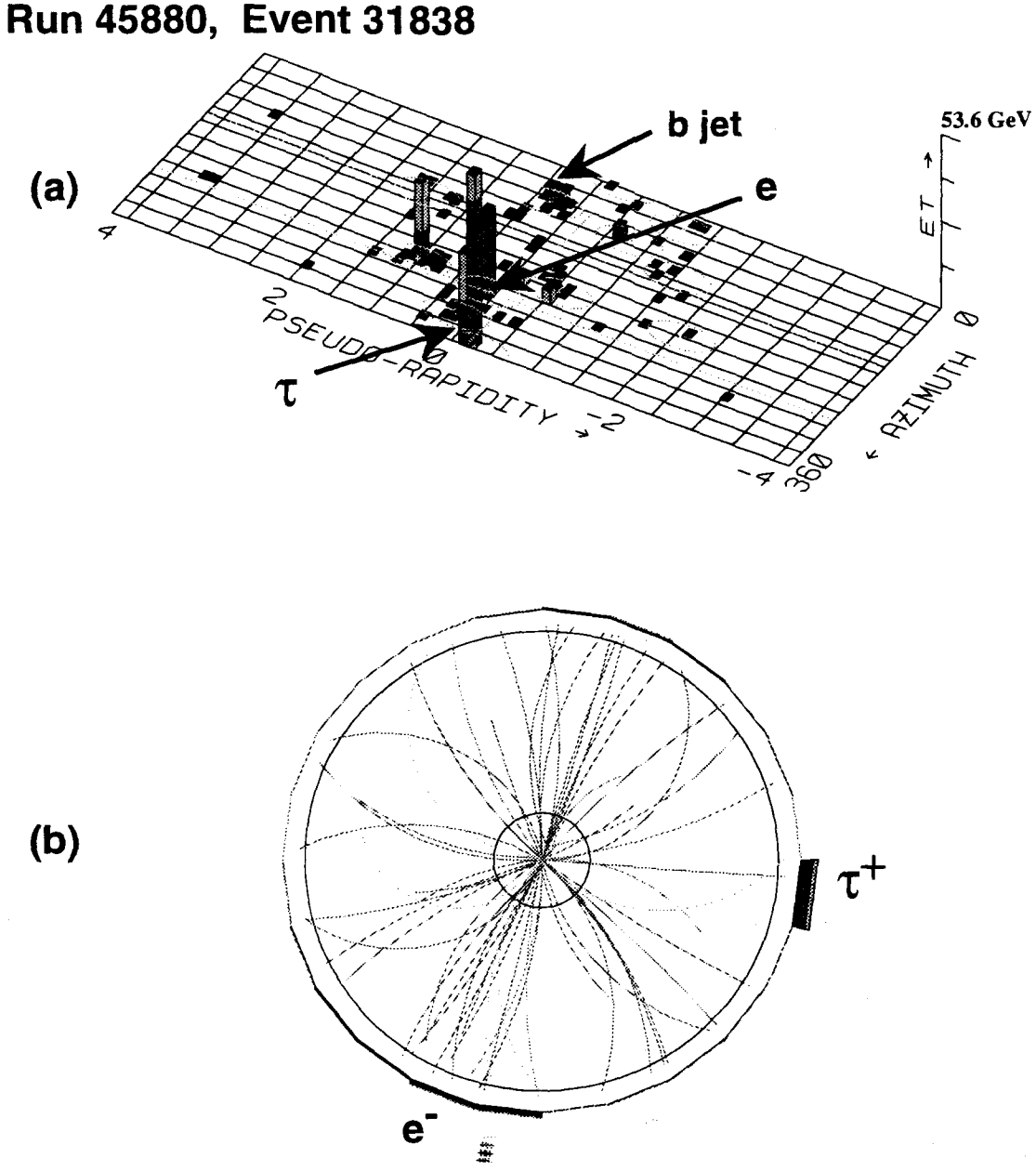

Figure 7.9: Event display for a candidate $e - \tau$ event. Figure (a) shows the observed calorimeter E_T in the $\eta - \phi$ plane. Figure (b) gives a transverse view of the CTC shows the reconstructed charged tracks. The jet satisfying a soft-lepton b quark tagging algorithm is indicated.

Based on the jet probability, the tau candidate jet in event **A** (per table 7.4) is consistent with originating from the primary vertex. The η-width of the jet is outside the usual distribution for energetic τ jets. It is unlikely that this jet is from a hadronic tau decay.

Dilepton event **B** is more interesting. The jet passes the η-width cut used earlier. Event **B** also contains a jet identified as a b jet by SVX tagging algorithms in other top quark studies (see section 7.4). In references [21] and [38] this event is treated as a $t\bar{t}$ event in which one W decay produces a muon and the other W decays hadronically.

Event **C** contains a τ candidate jet which fails the η-width selection criteria. Furthermore, the jet probability of this jet is sufficiently high that it will fail most reasonable cuts. It is unlikely that the jet is from a hadronic tau decay.

The τ candidate in event **D** has a high jet probability, and is inconsistent with the hypothesis of having come from a secondary vertex. It does, however, satisfy the η-width cut. While the jet does not satisfy the tau tagging algorithm, it is worth noting the presence of a b-tagged jet. This event was also selected as a top quark candidate event in other analyses [21]. A mass fit of the event, assuming top pair production and a lepton + jets decay mode, gave $m_{top} = 132 \pm 8$ GeV/c^2. This is inconsistent with the top mass found from other events in the same study, suggesting that this event is not well–described by the assumption that one of the W bosons decayed hadronically.

Assuming all the τ candidates to be background before tagging, a conservative estimate of 0.20 ± 0.06 background events remain after tagging. One event is observed.

The likelihood that this event is from top is increased considerably by the presence of an identified b jet in the event. The two additional (non-lepton) jets in the event are both SVX fiducial. Studies have shown that the efficiency for tagging SVX fiducial b jets is approximately 30% [21]. Monte Carlo simulation is used to estimate the number of expected tags in dilepton top events with an SVX-fiducial τ jet and two other SVX-fiducial jets. The expected value is 1.0 ± 0.1. The estimated background (mis–tagged b's), based on two SVX

Decay Mode	Efficiency
$\epsilon_{\tau-\tau}$	0.016 ± 0.007
$\epsilon_{e-\tau}$	0.038 ± 0.006
$\epsilon_{\mu-\tau}$	0.037 ± 0.007

Table 7.5: Calculated efficiencies for $t\bar{t} \longrightarrow \tau + lepton + X$, before tau tagging.

fiducial jets, is 0.06 ± 0.04 tags. This includes a small correlation found between multiple tags in the generic jet sample.

The estimated background from false tags (τ and b) is 0.001 ± 0.001 events. Calculating the rate of false dilepton events (real leptons from non-top sources) from e-e, e-μ, and $\mu-\mu$ studies [21] by replacing electron and muon efficiencies with τ identification efficiencies results in a prediction of $0.05^{+0.05}_{-0.03}$ event before b-tagging. This becomes $0.002^{+0.003}_{-0.001}$ event after b-tagging.

Monte Carlo simulation (ISAJET + detector simulation) is used to calculate the efficiency of the selection requirements. For those cases in which both W's decays to τ leptons, with one τ decaying leptonically and the other τ producing a hadronic jet, the likelihood of misidentifying the electron/muon as being directly from a W is considered as part of the $e-\tau$ and $\mu-\tau$ efficiency. The efficiencies for the tau–inclusive dilepton channels, for $m_{top} = 176$ GeV/c^2, are given in table 7.5.

When these efficiencies are multiplied by the efficiency of the loose tau tag detailed earlier in this chapter, only 0.12 dilepton event from top is expected in the Run 1a data.

7.3 Lepton + Jet Top Search

Those decay channels in which one W decays leptonically and the other hadronically are known as the lepton + jets modes. While having the advantage of a much larger branching fraction of top pair decays, these modes are more difficult to identify because of the larger background from W + jet events (see chapter 6). To reduce this background,

an SVX-based b-tagging algorithm (section 7.4) is used. It is required that at least one jet (other than the τ candidate) be identified as a b jet.

A search is made of the W + jets sample of chapter 6, with the upper-bound restriction on the jet energy increased to 50 GeV and the upper-bound on the $\not\!\!E_T$ removed. There is only one event in the data sample (the same event shown in figure 6.14). There are no b-tagged jets in this event.

The number of pre-tag τ candidate events, with the assumption that none are from top events, is used to make a conservative estimate of the background after tagging by applying the background rejection factor (for number of fake τ's) and the b-tag fake rates. The number of tau tags from background is computed to be 1.7 ± 0.5. The amount of background after τ and b identification is calculated to be 0.25 ± 0.15 event.

To avoid the logical problems of using the $W \longrightarrow \tau + 3$ jets sample for measurements of both W cross-section and background to top, the W cross–section obtained from electrons and muons [21] is used for estimating the rate of b tags from W + jets events in the leptons + jets search.

The efficiency for detection of $t\bar{t} \longrightarrow \tau + \ jets$ is determined to be 0.059 ± 0.007 from Monte Carlo studies. Using the Run 1a luminosity and Standard Model branching ratios, this leads to an predicted 0.12 events in the data.

7.4 Identification of Bottom Quarks

The presence of two real bottom quarks in $t\bar{t}$ events provides a means for greatly reducing the background in samples thought to be top–enriched. Two independent techniques were used at CDF during Run 1a to identify b jets. The first algorithm uses SVX tracking information to attempt the identification of a secondary vertex associated with the b decay.

Of the three SVX tagging algorithms used at CDF the jet probability technique is used in this analysis. A slightly different set of track selection requirements is imposed in the identification of jets from bottom quarks due to the different kinematics of the decay.

Tracks with two associated SVX hits are permitted. Only tracks with $P_T > 1.5$ GeV/c and positive jet probability are considered in b-tagging. Jets with at least two good SVX tracks and $\mathcal{P}^+_{jet} < 0.01$ are tagged as b's.

The sole SVX b-tagged jet in this study (see section 7.2.2) has a jet probability of 3.3×10^{-4}, well below the upper bound required for tagging. This jet also satisfies a tagger based on explicit reconstruction of the secondary vertex [21],[34].

Chapter 8

Results and Conclusions

Previous chapters have shown the technique by which hadronic jets from the decay of high-P_T τ leptons are distinguished from jets arising from other sources. The results of the application of the tau tagger to the data are now summarized.

The Silicon Vertex Detector at Fermilab has sufficient resolving power in the plane transverse to the beamline to allow the observation of the systematically larger impact parameters of tracks from the decay of high-P_T τ leptons. This allows for the measurement of the fractional tau content of a test monojet sample ($62^{+9}_{-10}\%$), as well as the only direct measurement to date of the τ lifetime at a hadron collider facility ($300^{+27}_{-51}(stat)\pm 17(sys)\ fs$).

Furthermore, the construction of a jet probability variable from the SVX impact parameters of the tracks in a jet, based on the measured resolution of the tracking systems, can be used to preferentially select tau jets from those of background. When used in concert with a calorimetry–based jet collimation cut, the jet probability can provide a background rejection factor of 56 ± 7 while maintaining a tau efficiency of 0.35 ± 0.03. These values, based on the jet probability window cut and η-width cuts described in earlier chapters, result in an increase in the signal-to-noise ratio of data samples by a factor of approximately 20. The tunability of the cuts allows for considerable flexibility in the values of the cuts, according to the needs of a particular analysis.

# Jets	# of taus	Efficiency	$\sigma \times$ BR
0	411 ± 14	0.0123 ± 0.0010	1731 ± 177 pb
1	26 ± 4	0.00315 ± 0.0006	427 ± 132 pb
2	3 ± 0.4	0.00228 ± 0.0004	68 ± 41 pb
3	1 ± 1	0.00158 ± 0.002	33 ± 33 pb

Table 8.1: Cross-section times branching ratios as a function of jet multiplicity in $W \longrightarrow \tau + \nu_\tau$ events.

8.1 Cross-Section Measurements

The tau–tagging technique was used to create samples of hadronic tau decays from real W boson production accompanied by radiative jet production. Measurements of the cross-sections times branching ratios for the tau modes of W decay are given in table 8.1. The numbers shown are the result of the calculations of the form:

$$\sigma \times \mathrm{BR} = \frac{N}{\epsilon \int \mathcal{L}}$$

where

- N is the number of taus
- ϵ is the efficiency for identification
- $\int \mathcal{L}$ is the integrated luminosity, which was $19.3 \pm 0.7 pb^{-1}$ in Run 1a. [21]

The values given in table 8.1 are consistent with previously published numbers for the electron and muon channels of W decay, and are plotted along with the electron and muon values in figure 8.1 for comparison.

8.2 Top Search Results

Recent top searches in the electron and muon channels at CDF [38] indicate a top mass of $176 \pm 8(stat.) \pm 10(sys.)$ GeV/c^2 and a $t\bar{t}$ production cross–section of $6.8^{+3.6}_{-2.4}$. Monte

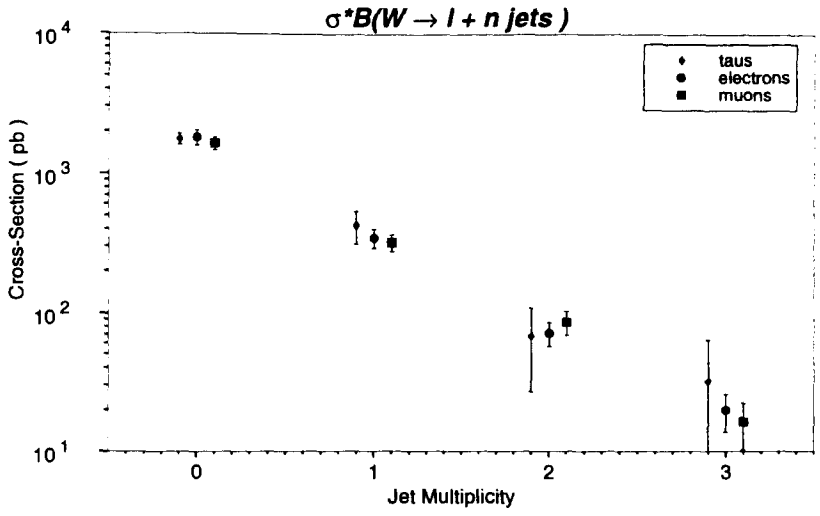

Figure 8.1: The cross-section times branching ratio for the leptonic decays of the W boson.

Carlo studies based on these results yield a prediction of 0.12 tau dilepton event and 0.12 b-tagged tau + jets event in the Run 1a data.

A search for tau–inclusive dilepton top decays results in one event found, with an estimated background of $0.25^{+0.08}_{-0.07}$ event ($0.003^{+0.005}_{-0.003}$ event after b-tagging). A search of the τ + jets decay modes yielded no events, with a predicted background of 0.25 ± 0.15 event.

The observed data does not contradict the results obtained from top quark searches in other channels. Based on the limited statistics from this search, the event is not claimed as signal.

8.3 Conclusions

The work demonstrates that it is possible to identify and study hadronic tau decays via precision tracking techniques. The utility of this technique was shown through the creation of high-purity data samples of hadronic tau jets in event topologies where the signal-to-noise prior to tagging was unfavorable. The ability to identify taus in such environments

extends the ability to explore the properties and interactions of elementary particles. The prospects for future use of these techniques are discussed in the Appendix.

Appendices

Appendix A

Prospects for Future Work

The development of a technique by which jets from semileptonic tau decays can be distinguished from other jets in a hadronic collider environment permits many new areas of research, only a few of which are explored in this work. In this appendix, possible continuations of the tau tagging research are presented.

Data collection at CDF continues with Run 1b, in which it is hoped that a data set from $\int \mathcal{L} \sim 100 pb^{-1}$ may be obtained. Such an increase in integrated luminosity provides obvious benefits to those studies which were statistically limited in Run 1a ($W+ \geq 2$ jets, top quark searches).

The data samples using tau–tagged events may be added to electron and muon data samples to conduct measurements of parton distribution functions in protons and antiprotons. The basis of this measurement is the charge asymmetry in the production of W bosons from valence quark interaction. A W^+ boson is typically produced by the reaction $u + \bar{d} \rightarrow W^+$, while the W^- is produced by $\bar{u} + d \rightarrow W^-$. Because the up (anti-up) quarks tend to carry a larger fraction of the proton (anti-proton) momentum than the down (anti-down) quarks, the W^+ tend to be boosted in the direction of the proton. This is seen in $W \rightarrow e\nu_e$ and $W \rightarrow \mu\nu_\mu$ events [42]. Utilization of a loose tau tag permits a suitably pure monojet sample for observation of the charge asymmetry via tau samples.

Figure A.1 shows the charge and event η distributions of a monojet sample with loose jet probability and η-width cuts (at least one positive jet probability track and $\langle \eta \rangle < 0.8$).

The sample is measured to be $(90 \pm 4)\%$ pure, and shows no obvious bias either in terms of charge or pseudo–rapidity distributions. If the pseudo–rapidity is plotted separately for jets of charge $\pm$ 1, then a difference is seen (figure A.2). A charge asymmetry, defined as

$$A = \frac{N_{positive} - N_{negative}}{N_{positive} + N_{negative}}$$

for each η bin is computed and plotted in figure A.3. Though statistically limited, the data show a charge dependence in the pseudo–rapidity distribution. Further data can be used to reduce the statistical errors so that the results may be usefully combined with electron and muon results.

Also of interest at CDF may be searches for light Higgs bosons. The Higgs bosons are expected to decay preferentially to heavy particles. The tau is by far the most massive of the known leptons. If leptonic decay modes of the Higgs are sought, the ability to distinguish the semileptonic decays of the τ could be of use.

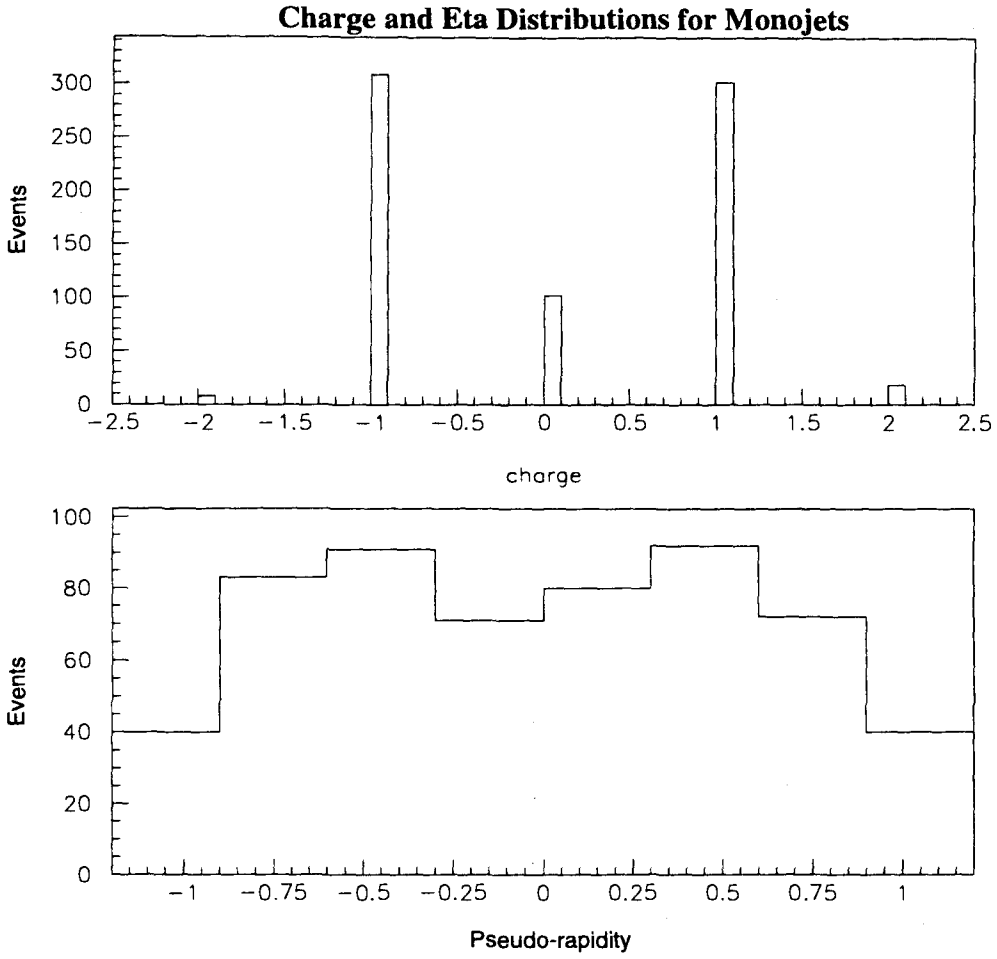

Figure A.1: Charge and η distributions in a loosely-tagged monojet sample.

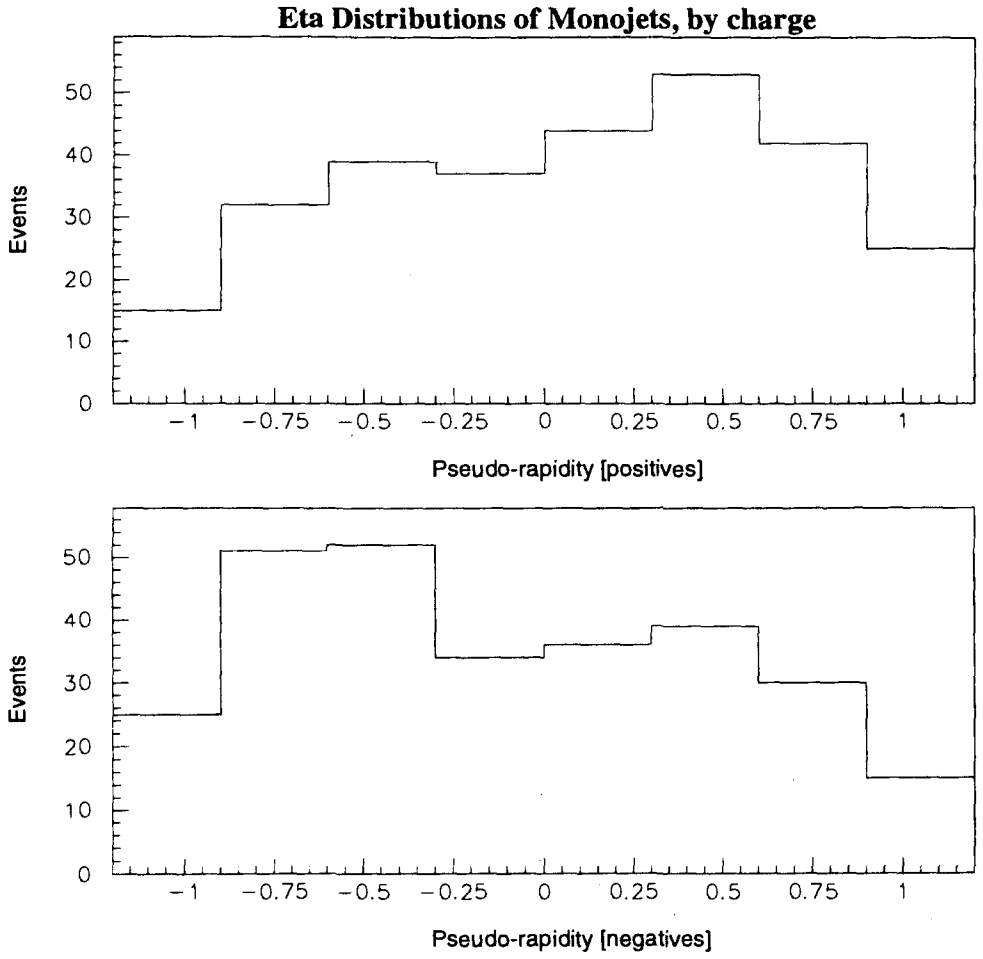

Figure A.2: Pseudo-rapidity distributions for positive (a) and negative (b) tau jets.

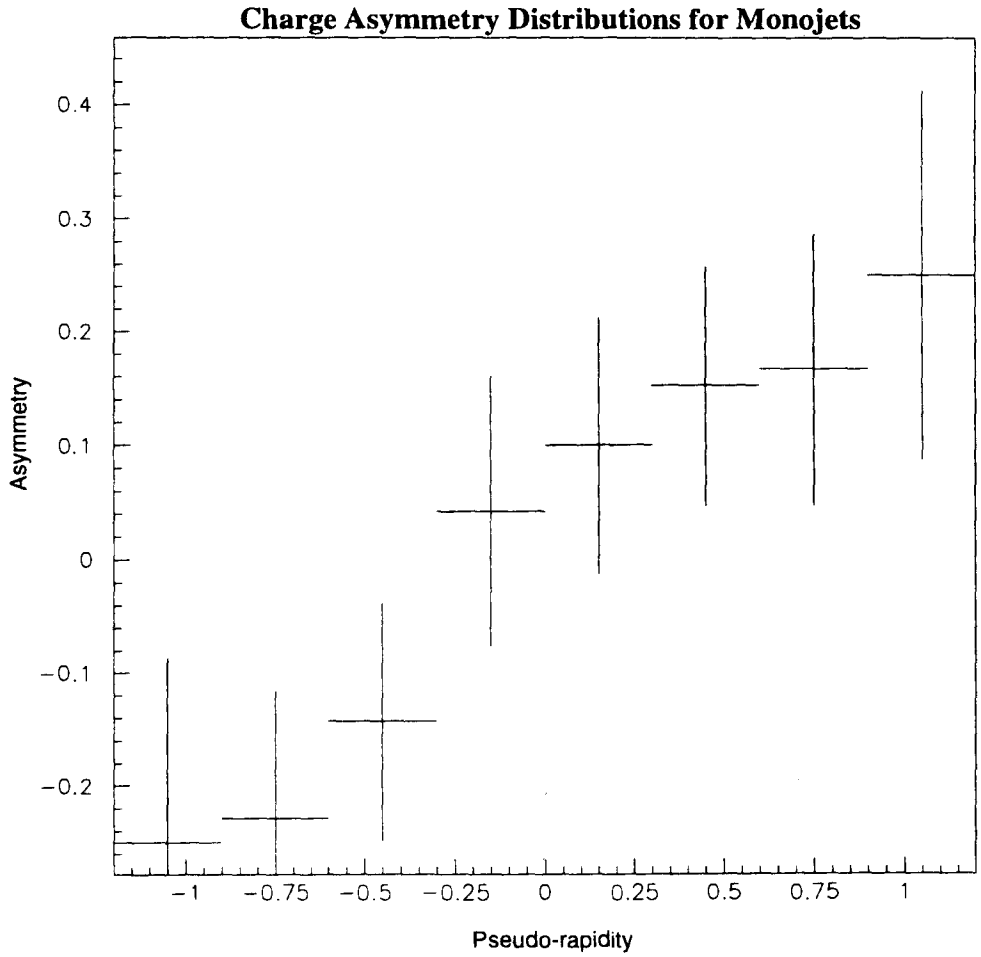

Figure A.3: Charge asymmetry as a function of pseudo-rapidity.

Appendix B

The Longitudinal Distribution of the Primary Event Vertex

The geometric acceptance for a given class of events depends not only on the spatial distribution of that class and the geometry of the detector, but also on the location and extent of the interaction region. To understand the longitudinal distribution of the interaction region in Run 1a, the vertices reconstructed from the VTX in the minimum bias data sample are used to determine a single set of descriptors for use in Monte Carlo.

The reconstructed vertices from the VTX are classified by quality, which is defined by the number of tracks linked to the vertex, the total momentum associated with those tracks, etc. For the purposes of this appendix, only those vertices which have the highest quality rating (12) are considered. Furthermore, to insure sufficient statistics for a good fit there are required to be at least 1000 events in each run have a class 12 vertex. There are 279 runs which meet these criteria.

The distribution of the z position of the vertices within a given run is well-described by a gaussian out to the limit of statistics, as shown by a typical run (figure B.1).

Because the interaction region varies from run to run, one cannot meaningfully plot all the vertices from the entire run and attempt to fit a single histogram. Therefore, each run is fit separately, with the results seen in figures B.2 and B.3,where the errors given on each point are those returned from the MINUIT fit.

In order to determine a single mean and width for purposes of simulation, the fit values for each run are combined (weighted by the errors) into 50 bins and the result fit by

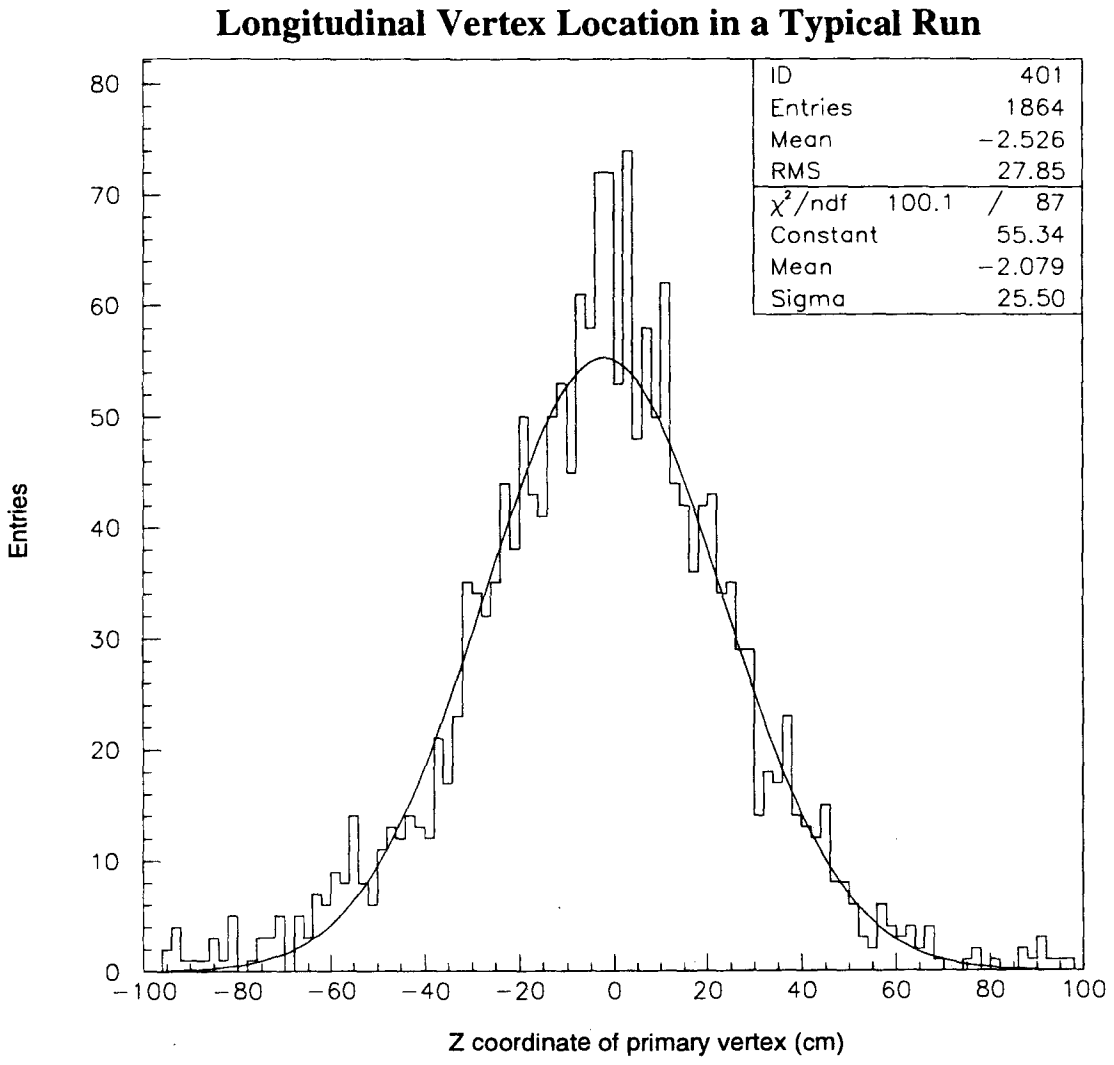

Figure B.1: The primary vertex location for a typical data run during Run 1a.

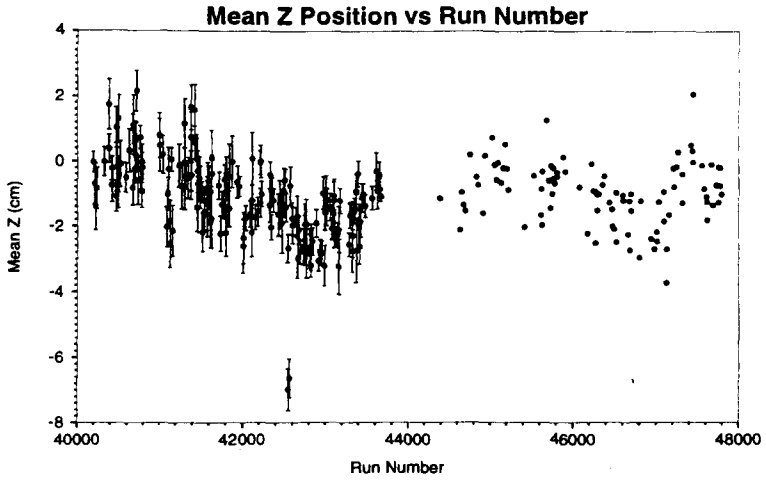

Figure B.2: The fit mean z positions of data runs in Run 1a.

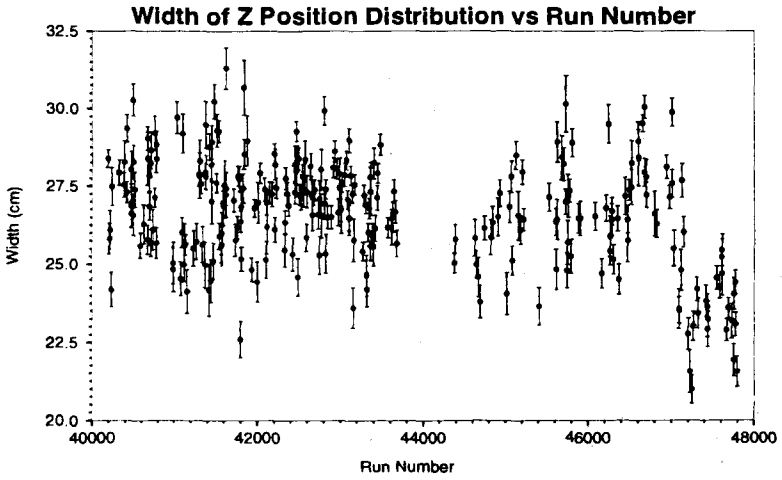

Figure B.3: The fit widths of the z position of data runs in Run 1a.

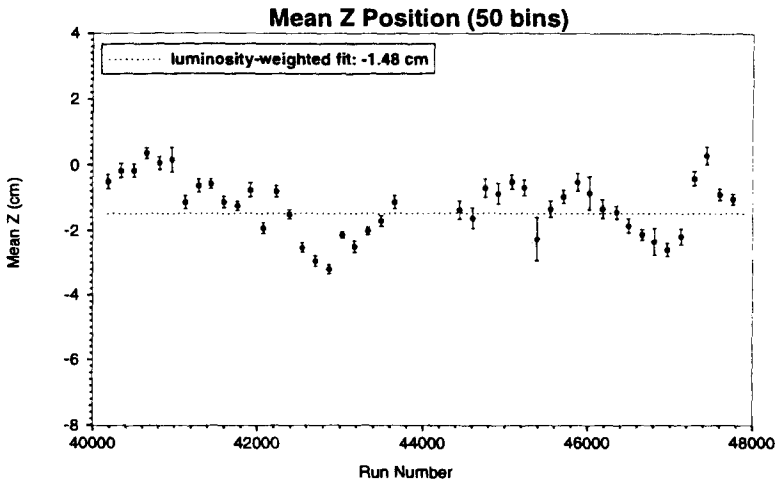

Figure B.4: The fit mean z positions of data runs in Run 1a, in 50 bins.

weighting each bin with the integrated luminosity for the runs spanned. This is necessary to prevent biasing the fit toward the early portions of the run, where more runs meet the selection criteria due to lower rate-limiting (as a result of lower instantaneous luminosity). The results of the binning are shown in figures B.4 and B.5.

A mean of 1.48 $\pm$ 0.11 cm and a width of 26.65 $\pm$ 0.18 cm is obtained from the integrated luminosity weighting of the 50 bins. The errors on these values are from the fits only; no attempt has been made to account for errors in the integrated luminosity for each bin, which are typically about 2-3%.

These value are used for Monte Carlo studies of geometric acceptance and trigger biases.

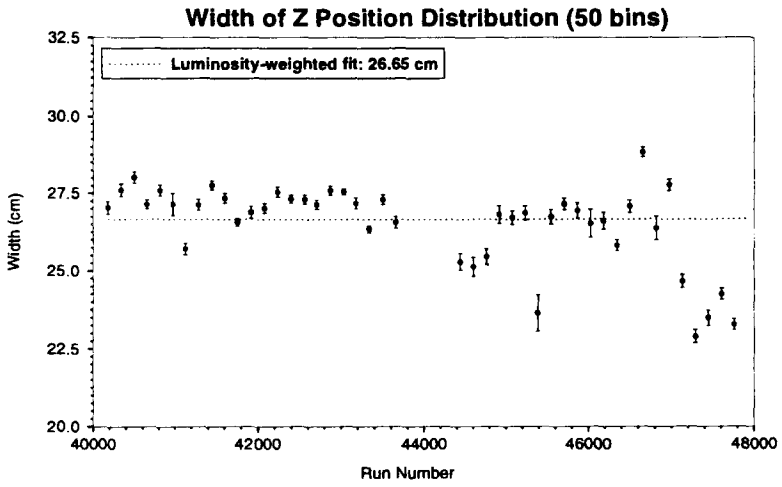

Figure B.5: The fit widths of the z position of data runs in Run 1a, in 50 bins.

Appendix C

The CDF Collaboration

The operation of an experiment the size of CDF is a monumental undertaking; that any of this works at all still amazes me. The successes of CDF are due to the contributions of a great many people over the years. Those who were members of the collaboration during the 1992-1993 run are listed below.

F. Abe,[13] M. G. Albrow,[7] D. Amidei,[16] J. Antos,[28] C. Anway-Wiese,[4] G. Apollinari,[26] H. Areti,[7] P. Auchincloss,[25] F. Azfar,[21] P. Azzi,[20] N. Bacchetta,[18] W. Badgett,[16] M. W. Bailey,[24] J. Bao,[34] P. de Barbaro,[25] A. Barbaro-Galtieri,[14] V. E. Barnes,[24] B. A. Barnett,[12] P. Bartalini,[23] G. Bauer,[15] T. Baumann,[9] F. Bedeschi,[23] S. Behrends,[2] S. Belforte,[23] G. Bellettini,[23] J. Bellinger,[33] D. Benjamin,[32] J. Benlloch,[15] D. Benton,[21] A. Beretvas,[7] J. P. Berge,[7] S. Bertolucci,[8] A. Bhatti,[26] K. Biery,[11] M. Binkley,[7] F. Bird,[29] D. Bisello,[20] R. E. Blair,[1] C. Blocker,[29] A. Bodek,[25] V. Bolognesi,[23] D. Bortoletto,[24] C. Boswell,[12] T. Boulos,[14] G. Brandenburg,[9] E. Buckley-Geer,[7] H. S. Budd,[25] K. Burkett,[16] G. Busetto,[20] A. Byon-Wagner,[7] K. L. Byrum,[1] C. Campagnari,[7] M. Campbell,[16] A. Caner,[7] W. Carithers,[14] D. Carlsmith,[33] A. Castro,[20] Y. Cen,[21] F. Cervelli,[23] J. Chapman,[16] M.-T. Cheng,[28] G. Chiarelli,[8] T. Chikamatsu,[31] S. Cihangir,[7] A. G. Clark,[23] M. Cobal,[23] M. Contreras,[5] J. Conway,[27] J. Cooper,[7] M. Cordelli,[8] D. P. Coupal,[29] D. Crane,[7] J. D. Cunningham,[2] T. Daniels,[15] F. DeJongh,[7] S. Delchamps,[7] S. Dell'Agnello,[23] M. Dell'Orso,[23] L. Demortier,[26] B. Denby,[23] M. Deninno,[3] P. F. Derwent,[16] T. Devlin,[27] M. Dickson,[25] S. Donati,[23] R. B. Drucker,[14] A. Dunn,[16] K. Einsweiler,[14] J. E. Elias,[7] R. Ely,[14] E. Engels, Jr.,[22] S. Eno,[5] D. Errede,[10] S. Errede,[10] Q. Fan,[25] B. Farhat,[15] I. Fiori,[3] B. Flaugher,[7] G. W. Foster,[7] M. Franklin,[9] M. Frautschi,[18] J. Freeman,[7] J. Friedman,[15] H. Frisch,[5] A. Fry,[29] T. A. Fuess,[1] Y. Fukui,[13] S. Funaki,[31] G. Gagliardi,[23] S. Galeotti,[23] M. Gallinaro,[20] A. F. Garfinkel,[24] S. Geer,[7] D. W. Gerdes,[16] P. Giannetti,[23] N. Giokaris,[26] P. Giromini,[8] L. Gladney,[21] D. Glenzinski,[12] M. Gold,[18] J. Gonzalez,[21] A. Gordon,[9] A. T. Goshaw,[6] K. Goulianos,[26] H. Grassmann,[6] A. Grewal,[21] G. Grieco,[23] L. Groer,[27] C. Grosso-Pilcher,[5] C. Haber,[14] S. R. Hahn,[7] R. Hamilton,[9] R. Handler,[33] R. M. Hans,[34] K. Hara,[31] B. Harral,[21] R. M. Harris,[7] S. A. Hauger,[6] J. Hauser,[4] C. Hawk,[27] J. Heinrich,[21] D. Cronin-Hennessy,[6] R. Hollebeek,[21] L. Holloway,[10] A. Hölscher,[11] S. Hong,[16] G. Houk,[21] P. Hu,[22] B. T. Huffman,[22] R. Hughes,[25] P. Hurst,[9] J. Huston,[17] J. Huth,[9] J. Hylen,[7] M. Incagli,[23] J. Incandela,[7] H. Iso,[31] H. Jensen,[7] C. P. Jessop,[9] U. Joshi,[7] R. W. Kadel,[14] E. Kajfasz,[7a] T. Kamon,[30] T. Kaneko,[31] D. A. Kardelis,[10] H. Kasha,[34] Y. Kato,[19] L. Keeble,[30] R. D. Kennedy,[27] R. Kephart,[7] P. Kesten,[14] D. Kestenbaum,[9] R. M. Keup,[10] H. Keutelian,[7] F. Keyvan,[4] D. H. Kim,[7] H. S. Kim,[11] S. B. Kim,[16] S. H. Kim,[31] Y. K. Kim,[14] L. Kirsch,[2] P. Koehn,[25] K. Kondo,[31] J. Konigsberg,[9] S. Kopp,[5] K. Kordas,[11] W. Koska,[7] E. Kovacs,[7a] W Kowald,[6] M. Krasberg,[16] J. Kroll,[7] M. Kruse,[24] S. E. Kuhlmann,[1] E. Kuns,[27] A. T. Laasanen,[24] S. Lammel,[4] J. I. Lamoureux,[33] T. LeCompte,[10] S. Leone,[23] J. D. Lewis,[7] P. Limon,[7] M. Lindgren,[4] T. M. Liss,[10] N. Lockyer,[21] O. Long,[21] M. Loreti,[20] E. H. Low,[21] J. Lu,[30] D. Lucchesi,[23] C. B. Luchini,[10] P. Lukens,[7] P. Maas,[33] K. Maeshima,[7] A. Maghakian,[26] P. Maksimovic,[15] M. Mangano,[23] J. Mansour,[17] M. Mariotti,[23] J. P. Marriner,[7] A. Martin,[10] J. A. J. Matthews,[18] R. Mattingly,[2] P. McIntyre,[30] P. Melese,[26] A. Menzione,[23] E. Meschi,[23] G. Michail,[9] S. Mikamo,[13] M. Miller,[5] R. Miller,[17] T. Mimashi,[31] S. Miscetti,[8] M. Mishina,[13] H. Mitsushio,[31] S. Miyashita,[31] Y. Morita,[13] S. Moulding,[26] J. Mueller,[27] A. Mukherjee,[7] T. Muller,[4] P. Musgrave,[11] L. F. Nakae,[29] I. Nakano,[31] C. Nelson,[7] D. Neuberger,[4] C. Newman-Holmes,[7] L. Nodulman,[1] S. Ogawa,[31] S. H. Oh,[6] K. E. Ohl,[34] R. Oishi,[31] T. Okusawa,[19] C. Pagliarone,[23] R. Paoletti,[23] V. Papadimitriou,[7] S. Park,[7] J. Patrick,[7] G. Pauletta,[23] M. Paulini,[14] L. Pescara,[20]

M. D. Peters,[14] T. J. Phillips,[6] G. Piacentino,[3] M. Pillai,[25] R. Plunkett,[7] L. Pondrom,[33] N. Produit,[14] J. Proudfoot,[1] F. Ptohos,[9] G. Punzi,[23] K. Ragan,[11] F. Rimondi,[3] L. Ristori,[23] M. Roach-Bellino,[32] W. J. Robertson,[6] T. Rodrigo,[7] J. Romano,[5] L. Rosenson,[15] W. K. Sakumoto,[25] D. Saltzberg,[5] A. Sansoni,[8] V. Scarpine,[30] A. Schindler,[14] P. Schlabach,[9] E. E. Schmidt,[7] M. P. Schmidt,[34] O. Schneider,[14] G. F. Sciacca,[23] A. Scribano,[23] S. Segler,[7] S. Seidel,[18] Y. Seiya,[31] G. Sganos,[11] A. Sgolacchia,[3] M. Shapiro,[14] N. M. Shaw,[24] Q. Shen,[24] P. F. Shepard,[22] M. Shimojima,[31] M. Shochet,[5] J. Siegrist,[29] A. Sill,[7a] P. Sinervo,[11] P. Singh,[22] J. Skarha,[12] K. Sliwa,[32] D. A. Smith,[23] F. D. Snider,[12] L. Song,[7] T. Song,[16] J. Spalding,[7] L. Spiegel,[7] P. Sphicas,[15] A. Spies,[12] L. Stanco,[20] J. Steele,[33] A. Stefanini,[23] K. Strahl,[11] J. Strait,[7] D. Stuart,[7] G. Sullivan,[5] K. Sumorok,[15] R. L. Swartz, Jr.,[10] T. Takahashi,[19] K. Takikawa,[31] F. Tartarelli,[23] W. Taylor,[11] Y. Teramoto,[19] S. Tether,[15] D. Theriot,[7] J. Thomas,[29] T. L. Thomas,[18] R. Thun,[16] M. Timko,[32] P. Tipton,[25] A. Titov,[26] S. Tkaczyk,[7] K. Tollefson,[25] A. Tollestrup,[7] J. Tonnison,[24] J. F. de Troconiz,[9] J. Tseng,[12] M. Turcotte,[29] N. Turini,[3] N. Uemura,[31] F. Ukegawa,[21] G. Unal,[21] S. van den Brink,[22] S. Vejcik, III,[16] R. Vidal,[7] M. Vondracek,[10] R. G. Wagner,[1] R. L. Wagner,[7] N. Wainer,[7] R. C. Walker,[25] G. Wang,[23] J. Wang,[5] M. J. Wang,[28] Q. F. Wang,[26] A. Warburton,[11] G. Watts,[25] T. Watts,[27] R. Webb,[30] C. Wendt,[33] H. Wenzel,[14] W. C. Wester, III,[14] T. Westhusing,[10] A. B. Wicklund,[1] E. Wicklund,[7] R. Wilkinson,[21] H. H. Williams,[21] P. Wilson,[5] B. L. Winer,[25] J. Wolinski,[30] D. Y. Wu,[16] X. Wu,[23] J. Wyss,[20] A. Yagil,[7] W. Yao,[14] K. Yasuoka,[31] Y. Ye,[11] G. P. Yeh,[7] P. Yeh,[28] M. Yin,[6] J. Yoh,[7] T. Yoshida,[19] D. Yovanovitch,[7] I. Yu,[34] J. C. Yun,[7] A. Zanetti,[23] F. Zetti,[23] L. Zhang,[33] S. Zhang,[15] W. Zhang,[21] and S. Zucchelli[3]

(CDF Collaboration)

[1] *Argonne National Laboratory, Argonne, Illinois 60439*

[2] *Brandeis University, Waltham, Massachusetts 02254*

[3] *Istituto Nazionale di Fisica Nucleare, University of Bologna, I-40126 Bologna, Italy*

[4] *University of California at Los Angeles, Los Angeles, California 90024*

[5] *University of Chicago, Chicago, Illinois 60637*

[6] *Duke University, Durham, North Carolina 27708*

[7] *Fermi National Accelerator Laboratory, Batavia, Illinois 60510*

[8] *Laboratori Nazionali di Frascati, Istituto Nazionale di Fisica Nucleare, I-00044 Frascati, Italy*

[9] *Harvard University, Cambridge, Massachusetts 02138*

[10] *University of Illinois, Urbana, Illinois 61801*

[11] *Institute of Particle Physics, McGill University, Montreal H3A 2T8, and University of Toronto, Toronto M5S 1A7, Canada*

[12] *The Johns Hopkins University, Baltimore, Maryland 21218*

[13] *National Laboratory for High Energy Physics (KEK), Tsukuba, Ibaraki 305, Japan*

[14] *Lawrence Berkeley Laboratory, Berkeley, California 94720*

[15] *Massachusetts Institute of Technology, Cambridge, Massachusetts 02139*

[16] *University of Michigan, Ann Arbor, Michigan 48109*

[17] *Michigan State University, East Lansing, Michigan 48824*

[18] *University of New Mexico, Albuquerque, New Mexico 87131*

[19] *Osaka City University, Osaka 588, Japan*

[20] *Universita di Padova, Instituto Nazionale di Fisica Nucleare, Sezione di Padova, I-35131 Padova, Italy*

[21] *University of Pennsylvania, Philadelphia, Pennsylvania 19104*

[22] *University of Pittsburgh, Pittsburgh, Pennsylvania 15260*

[23] *Istituto Nazionale di Fisica Nucleare, University and Scuola Normale Superiore of Pisa, I-56100 Pisa, Italy*

[24] *Purdue University, West Lafayette, Indiana 47907*

[25] *University of Rochester, Rochester, New York 14627*

[26] *Rockefeller University, New York, New York 10021*

[27] *Rutgers University, Piscataway, New Jersey 08854*

[28] *Academia Sinica, Taiwan 11529, Republic of China*

[29] *Superconducting Super Collider Laboratory, Dallas, Texas 75237*

[30] *Texas A&M University, College Station, Texas 77843*

[31] *University of Tsukuba, Tsukuba, Ibaraki 305, Japan*

[32] *Tufts University, Medford, Massachusetts 02155*

[33] *University of Wisconsin, Madison, Wisconsin 53706*

[34] *Yale University, New Haven, Connecticut 06511*

Bibliography

[1] Y. S. Tsai, *Decay Correlations of Heavy Leptons in* $e^+ + e^- \rightarrow l^+ + l^-$, Phys. Rev. D **4**, 2821 (1971).

[2] W. Trischuk, *A Review of the* τ *Lifetime*, 2nd Workshop on Tau Lepton Physics, Columbus, Ohio. To be published in the proceedings. CERN Pre-print CERN-PPE/92-197.

[3] P. Privitera, *The Tau Polarization Measurement at LEP And The Nature of The Tau-W-Tau-Neutrino Coupling*, Phys. Lett. **B288**, 227-231 (1992)

[4] M. Perl, et al, *Evidence for Anomalous Lepton Production in* $e^+ - e^-$ *Annihilation*, Phys. Rev. Lett. **35**, 1489-1492 (1975).

[5] C. Albajar, et al. (UA1 Collaboration), *Events With Large Missing Transverse Energy At The CERN Collider:* $W \longrightarrow$ *Tau Neutrino Decay And Test Of Tau - Mu E Universality At* $Q^2 = M(W^2)$, Phys.Lett. **185B**, 233 (1987)

[6] F. Abe, et al, (The CDF Collaboration), *Measurement of the Ratio* $B(W \rightarrow \tau\nu)/B(W \rightarrow e\nu)$ *in* $p\bar{p}$ *Collisions at* $\sqrt{s} = 1.8$ *TeV*, Phys. Rev. Lett. **68**, 3403-3407 (1992).

[7] R. R. Wilson, *The Tevatron*, Phys. Today **10**, 23-30 (1977).

[8] F. Abe, et al (The CDF Collaboration), *The CDF Detector: An Overview*, Nucl. Instr. and Meth. **A271**, 387-403 (1988).

[9] CDF cross sectional view diagram courtesy Randy Keup. Diagram first appeared in published form in reference [21].

[10] D. Amidei, et al, *The Silicon Vertex Detector of the Collider Detector at Fermilab*, Nucl. Instr. and Meth. **A350**, 73-130 (1994).

[11] *The CDF Vertex Detector*, internal note in progress, to be submitted to Nucl. Instr. and Meth. (1994).

[12] F. Bedeschi, et al, *Design and Construction of the CDF Central Tracking Chamber*, Nucl. Instr. and Meth. **A268**, 50-74 (1988).

[13] L. Balka, et al, *The CDF Central Electromagnetic Calorimeter*, Nucl. Instr. and Meth. **A267** 272-279 (1988).

[14] S. Bertolucci, et al, *The CDF Central and Endwall Hadron Calorimeter*, Nucl. Instr. and Meth. **A267** 301-314 (1988).

[15] Y. Fukui, et al, *CDF End Plug Electromagnetic Calorimeter Using Conductive Plastic Proportional Tubes*, Nucl.. Instr. and Meth. **A267**, 280-300 (1988).

[16] *The CDF End Plug Hadronic Calorimeter*, internal note in progress, to be submitted to Nucl. Instr. and Meth.

[17] G. Brandenburg, et al, *An Electromagnetic Calorimeter for the Small Angle Regions of the Collider Detector at Fermilab*, Nucl. Instr. and Meth. **A267**, 257-271 (1988).

[18] S. Cihangir, et al, *The CDF Forward/Backward Hadron Calorimeter* , Nucl. Instr. and Meth. **A267**, 249-256 (1988)

[19] G. Ascoli, et al, *CDF Central Muon Detector*, Nucl. Instr. and Meth. **A268** 33-40 (1988).

[20] A. Gauthier, et al, *Design and Performance of Drift Chambers for the Central Muon Upgrade of the CDF Detector*, to be submitted to Nucl. Instr. and Meth.

[21] F. Abe, et al, (The CDF Collaboration), *Evidence for Top Quark Production in $p\bar{p}$ Collisions at $\sqrt{s}$ = 1.8 TeV*, Fermilab Preprint FERMILAB-PUB-94-097-E (April 1994). Submitted to Phys. Rev. D.

[22] E. Barsoti, et al, *Fastbus Data Acquisition for CDF*, Nucl. Instr. and Meth. **A269**, 82-92 (1988).

[23] G. Drake, et al, *CDF Front End Electronics: The RABBIT System*, Nucl. Instr. and Meth. **A269**, 68-81 (1988).

[24] D. Amidei, et al, *A Two Level Fastbus Based Trigger System for CDF*, Nucl. Instr. and Meth. **A269**, 51-62 (1988).

[25] G. Ascoli, et al, *CDF Central Muon Level 1 Trigger Electronics*, Nucl. Instr. and Meth. **A269**, 63-67 (1988).

[26] W. Badgett, *Measurement of $\sigma \cdot B(W \to \mu\nu)$, $\sigma \cdot B(Z^0 \to \mu^+\mu^-)$ and $R_\mu = \sigma \cdot B(W \to \mu\nu)/\sigma \cdot B(Z^0 \to \mu^+\mu^-)$ and Extraction of $BR(W \to \mu\nu)$ and $\Gamma(W)$ in $p\bar{p}$ Collisions at $\sqrt{s}$ = 1.8 TeV*, Ph.D. thesis, University of Michigan (1994).

[27] G. W. Foster, et al, *A Fast Hardware Track Finder for the CDF Central Tracking Chambers*, Nucl. Instr. and Meth. **A269**, 93-100 (1988).

[28] J.T. Carrol, et al, *The CDF Level 3 Trigger*, Nucl. Instr. and Meth. **A300**, 552-567 (1991).

[29] F. Paige, S. Protopopescu, *IsaJet, A Monte Carlo Event Generator for pp and $p\bar{p}$ Reactions*, Brookhaven National Laboratory Report BNL-38034 (1986).

[30] S. Dell'Agnello, F. Bedeschi, *Combining the Primary Vertex Finder with the SVX Beam Line Measurements*, CDF Internal Note (1993).

[31] J. Konigsberg, T. Baumann, M. Franklin, *Tau/Jet Separation for Top Searches at CDF*, CDF Internal Note (1993).

[32] W.-M. Yao, L. Galtieri, R. Ely, J. Lys, M. Austern, *Study of Improved Track Selection for B Tagging With SVX*, CDF Internal Note (1993).

[33] D. Amidei, P.Derwent, D. Gerdes, S. Hong, S.B. Kim, T.Song, *Study of the Jet Probability Algorithm JPBTAG*, CDF Internal Note (1993).

[34] R. Hughes, P. Koehn, N.M. Shaw, *Efficiency and Background Studies Using the JETVTX B-Tagger*, CDF Internal Note (1993).

[35] S. Dell'Agnello, F. Bedeschi, G. Punzi, *The D-Phi Clustering B-Tagger*, CDF Internal Note (1992).

[36] J. Konigsberg, T. Baumann, M. Franklin, *A Top Dilepton Analysis Using Hadronic Taus*, CDF Internal Note (1993). The addition of the η-width cut was motivated by discussions with J. Konigsberg, who suggested the value used in this analysis.

[37] This diagram first appeared in reference [21].

[38] F. Abe, et al, (The CDF Collaboration) *Observation of Top Quark Production in $\bar{p}p$ Collisions with the CDF Detector at Fermilab*, Phys. Rev. Lett. **74**, 2626 (1995).

[39] S. Abachi, et al (The D0 Collaboration) *Search for the Top Quark at $p\bar{p}$ Collisions at $\sqrt{s} = 1.8$ TeV*, Phys. Rev. Lett. **72**,2138 (1994).

[40] E. Laenen, et al, *Phys Lett.* **B321**, 254, (1994).

[41] F. Abe, et al, (The CDF Collaboration), *Measurement of the $p\bar{p}$ Total Cross Section at $\sqrt{s} = 546$ GeV and 1.8 TeV*, Fermilab Preprint FERMILAB-PUB-93-234-E (Nov 1993); Submitted to Phys. Rev. D.

[42] F. Abe, et al, (The CDF Collaboration), *The Charge Asymmetry in W Boson Decays Produced in $\bar{p}p$ Collisions at $\sqrt{s} = 1.8TeV$*, to be published in Phys. Rev. Lett..